Optimum Design of Compact, Quiet, and Efficient Ventilation Fans

Mark Pastor Hurtado

Dissertation submitted to the faculty of the Virginia Polytechnic Institute and State University in partial fulfillment of the requirements for the degree of

Doctor of Philosophy
In
Mechanical Engineering

Ricardo A. Burdisso, Committee Chair
Pablo A. Tarazaga
William J. Devenport
Wing F. Ng
Seongim S. Choi

December 16th, 2019
Blacksburg, VA

Keywords: Multi-element, Tandem, Compact, Fan design

Optimum Design of Compact, Quiet, and Efficient Ventilation Fans

Mark Pastor Hurtado

ABSTRACT

Axial ventilation fans are used to improve the air quality, remove contaminants, and to control the temperature and humidity in occupied areas. Ventilation fans are one of the most harmful sources of noise due to their close proximity to occupied areas and widespread use. The prolonged exposure to hazardous noise levels can lead to noise-induced hearing loss. Consequently, there is a critical need to reduce noise levels from ventilation fans. Since fan noise scales with the 4-6th power of the fan tip speed, minimizing the fan tip speed and optimizing the duct geometry are effective methods to reduce fan noise. However, there is a tradeoff between reducing fan speed, noise and aerodynamic efficiency. To this end, a new innovative comprehensive optimum design methodology considering both aerodynamic efficiency and noise was formulated and implemented using a multi-objective genetic algorithm. The methodology incorporates a control vortex design approach that results in a spanwise chord and twist distribution of the blades that maximize the volumetric flow rate contribution of the outer radii, i.e. the axial flow velocity increases from the fan hub to the tip. The resulting blade geometry generates a given volumetric flow rate at the minimum fan tip speed. The fan design is complemented by the design of the optimum inlet duct geometry to maximize volumetric flow rate and minimize BL thickness for low noise generation. Good agreement with experimental results validates the design process. The present study also incorporates multi-element airfoils to further increase the aerodynamic characteristics of the fan blades and enable lower fan speeds and noise. Good agreement between experiments and predictions indicate that traditional blade element momentum methods can be implemented in conjunction with multi-element airfoil aerodynamic characteristics with good accuracy. A direct comparison of fans designed with single and multi-element airfoils has shown that fans designed with multi-element airfoils aerodynamically outperform single element airfoil fans.

Optimum Design of Compact, Quiet, and Efficient Ventilation Fans

Mark Pastor Hurtado

GENERAL AUDIENCE ABSTRACT

Axial ventilation fans are widely used to improve the air quality, remove contaminants, and to control the temperature and humidity in occupied areas. However, high noise levels from ventilations fans are a harmful source of noise that can lead to irreversible noise-induced hearing loss. Therefore, this work addresses a critical need for quiet and efficient ventilation fans. To this end, a new innovative comprehensive optimum design methodology considering both aerodynamic efficiency and noise was formulated, implemented, and tested. The methodology optimizes the fan geometry to maximize the volumetric flow rate and minimize noise. The fan design is complemented by the design of the optimum inlet duct geometry to increase the volumetric flow rate and minimize BL thickness for low noise generation. Good agreement with experimental results validates the design process. The present study also incorporates multi-element airfoils to further increase the aerodynamic characteristics of the fan blades. A direct comparison of fans designed with single and multi-element airfoils has shown that fans designed with multi-element airfoils aerodynamically outperform single element airfoil fans.

Acknowledgements

I would like to thank my advisor Dr. Ricardo Burdisso, whose technical insight, encouragement, and support created a wonderful environment in which to grow, professionally, academically, and personally during my graduate studies at Virginia Tech. I would also like to express my gratitude and appreciation to the members of my committee Dr. Pablo Tarazaga, Dr. William Devenport, Dr. Wing Ng, and Dr. Seongim Choi for their input and support. Additionally, I would like to thank my colleagues Sterling McBride, Lucas Spies, Pradosh Pritam Dash, and Daniel Wu from the Vibrations and Acoustics laboratory for their assistance in setting up experiments. I will always cherish their help, friendship and technical insights. Lastly, I would also like to thank the members of the GradSHPE chapter for creating a sense of community in Blacksburg where I could grow personally, academically, and professionally. Special thanks to Anthony Millican, Genesis Alvarez, Javier González-Rocha, Elisa Wasson, John Angarita, Kevin Moreno, Adam Lowery, and Adrian Davila for their insightful conversation and laughter.

I dedicate this dissertation to my parents and my fiancé Alyssa Murray, whose continuous and unconditional support have been essential for the completion of this work. Lastly, I would like to thank God for giving me the opportunity to successfully accomplish my academic and professional goals.

Table of Contents

List of Figures

List of Tables

Nomenclature

Symbol	Name	*Unit*
a	Swirl velocity coefficient	-
A	Area	m^2
a_1	Vertical ellipse axis	*m*
a_2	Horizontal ellipse axis	*m*
b	Half chord (c/2)	*m*
c	Chord	*m*
c_{air}	Speed of sound of air	*m/s*
C_d	Coefficient of drag	-
C_f	Coefficient of friction	-
C_l	Coefficient of lift	-
c_{total}	Chord-total	*m*
c_1	Chord - Main airfoil	*m*
c_2	Chord - Rear airfoil	*m*
d	Airfoil cascade spacing	*m*
D	Fan diameter	*m*
d_{TE}	Vertical displacement of the rear element	*% of the chord*
f	Frequency	*Hz*
f_{BPF}	Blade passage frequency	*Hz*
f_c	1/3rd octave band center frequency	*Hz*
F_c	Centrifugal force	*N*
f_ℓ	1/3rd octave band lower frequency limit	*Hz*
F_{loss}	Prandtl's tip loss factor	-
f_0	Reference peak frequency	*Hz*
f_u	1/3rd octave band upper frequency limit	*Hz*
h	Airfoil span	*m*
H	Shape factor	-
h_t	Stagnation enthalpy	*kJ/kg*
I_l	Acoustic intensity	$watts/m^2$
i_{motor}	Motor current	*Amps*
$K_L(\omega)$	Three-dimensional lift response factor	*m*
k_T	Motor torque constant	
k_1	Wave number	*m*
L	Lift force	*N*

L_I	Sound intensity level	*dB*
$\ell_s(\omega)$	Span-wise integral correlation length	*m*
L_p	Sound pressure level	*dB*
L_w	Sound power Level	*dB*
L_x	Length of exhaust duct	*m*
m	Mass	*kg*
$\dot{m}$	Mass flow rate	*kg/s*
M_e	BL edge Mach number	
M_{rel}	Relative Mach number	-
M_{tip}	Tip speed	-
n	Fan speed	*RPM*
n	Swirl velocity exponent	-
$\vec{n}$	Unit normal vector	-
N_B	Number of blades	-
N_m	Number of microphones	-
p	Static pressure	*Pa*
Δp	Pressure rise	*Pa*
P_B	Barometric pressure	*Pa*
P_{mech}	Mechanical power	*wats*
p_{ref}	Reference pressure	*Pa*
P_{shaft}	Shaft mechanical power	*watts*
p_t	Total pressure	*Pa*
p_{rms}	Root mean square pressure	*Pa*
P_v	Dynamic pressure	*Pa*
r	Radial position	*m*
R	Radius	*m*
R_{arc}	Arc radius	*m*
R_c	Air gas constant	*J/(kg*K)*
r_h	Hub radius	*M*
r_w	Distance from the wall	*m*
R_w	Normalized distance to the wall	-
Re	Reynolds number	-
RE_c	Chord Reynolds number	
s	Solidity	
S	Ellipse arc length	*m*
S_l	Spherical surface area	m^2

S_{FF}	Far-field acoustic pressure PSD	$\frac{N^2}{m^4}s$
$S_{LL}(\omega)$	PSD of the airfoil unsteady loading	$\frac{N^2}{m^2}s$
S_{WW}	Power spectral density (PSD) of the acoustic power	$Watts \cdot s$
St	Strouthal number	-
T	Thrust	*N*
T_r	Room temperature	*K*
Q	Torque	*n-m*
U	BL velocity	*m/s*
u_a	Externally-induced axial velocity	*m/s*
U_c	Convection speed of turbulence	*m/s*
U_e	BL edge velocity	*m/s*
u_{rms}	Stream-wise turbulence strength	*m/s*
u_t	Externally-induced tangential velocity	*m/s*
U_∞	Mean velocity in the free stream	*m/s*
U_τ	Friction velocity	*m/s*
V	Forward velocity	*m/s*
$\dot{V}$	Volumetric flow rate	m^3/s
$\bar{v}$	Circumferentially-averaged tangential velocity	*m/s*
$\bar{v}_a$	Average axial velocity	*m/s*
v_a	Rotor induced axial velocity	*m/s*
$\bar{V}_a$	Area average axial velocity	*m/s*
v_{air}	Air kinematic viscosity	m^2/s
$V_{pv,out}$	Pressure transducer voltage output	*Volts*
v_t	Rotor induced tangential velocity	*m/s*
V_t	Tangential velocity (Ωr)	*m/s*
v_θ	Swirl velocity	*m/s*
x	Airfoil transition location	*m*
W	Sound power	*watts*
W_a	Total axial velocity	*m/s*
W_{ref}	Reference acoustic power	*watts*
W_{rel}	Total relative velocity	*m/s*
W_t	Total tangential velocity	*m/s*
z	Ring height	*m*
α	Angle of attack (AoA)	*deg*
β	Blade twist	*deg*

Γ	Circulation	m^2/s
Γ_f	Gamma function	-
δ	BL thickness	*m*
δ^*	Displacement thickness	*m*
δ_n	Diameter number	
δ_1	Main airfoil rotation angle	*deg*
δ_2	Rear airfoil rotation angle	*deg*
ε	Drag-to-lift ratio	-
η_i	Inviscid froude efficiency	-
η_{local}	Local aerodynamic efficiency	-
η_m	Mechanical aerodynamic efficiency	*%*
η_p	Viscous profile efficiency	-
η_{total}	Total aerodynamic efficiency	-
θ	Momentum thickness	*m*
Θ	Ellipse angle	*deg*
θ^*	Density thickness	*m*
θ_a	Arc microphone angle	*deg*
λ	Acoustic wavelength	*m*
λ_f	Integral length scale	*m*
λ_w	local wake advance ratio	-
ν	Hub-to-tip ratio	-
ρ_{air}	Air density	kg/m^3
ρ_B	Room density	kg/m^3
σ_n	Speed number	m^3/s
ϕ	Local flow angle	*deg*
φ	Rotational angle	*deg*
Ψ	XROTOR iteration dummy variable	-
ψ_{opt}	Pressure coefficient	-
ω	Oscillation frequency	*rads/s*
Ω	Angular velocity	*rad/sec*
ω_c	1/3rd octave band center frequency	*rad/s*
ω_ℓ	1/3rd octave band lower frequency limit	*rad/s*
ω_u	1/3rd octave band upper frequency limit	*rad/s*

CHAPTER 1

1 Introduction and motivation

According to the National Institute for Occupational Safety and Health (NIOSH), poor air quality due to insufficient air flow and accumulated air contaminants can create a hazardous working environment for exposed workers. Poor air quality often occurs when working in confined or enclosed spaces with poor air circulation. When these conditions exist, the use of ventilation fans is necessary to provide a healthful and safe working environment (OSHA, 2013). Consequently, ventilation fans are used widely across different industries to improve the air quality, remove contaminants, and to control the temperature and humidity in the working areas.

For ventilation fans to be the most effective, they need to be in close proximity to the working areas. Consequently, loud ventilation fans are one of the most harmful sources of noise due to their proximity to the workers. Long term exposure to harmful noise levels can lead to irreversible hearing damage, i.e. noise-induced hearing loss (NIHL). Consequently, NIOSH has stablished recommended standards to regulate the exposure of high noise levels and prevent NIHL. The NIOSH recommendation is an exposure limit for occupational noise of 85 decibels, A-Weighted 8-hour time weighted average (TWA). It is also important to note that in the calculation of the TWA, the recommended exchange rate is 3dB. Therefore, for a 3dB increase in the noise levels, the time of exposure must be halved. Consequently, if the 85 dBA as an 8 hour TWA is exceeded, the use of all administrative controls must be used to ensure noise levels are reduced or the exposure time is reduced. The short term exposure to high noise levels is also hazardous as it creates physical and psychological stress, decrease job performance, and contribute to workplace accidents and injuries from difficulty to hear warning signals (Lin et al., 2012).

Due to future climate change, the demand for axial fans is expected to increase as the demand for cooling will exceed the demand for heating (Labriet et al., 2013). Consequently, the European Union introduced regulations on the minimum efficiency of ventilation fans in 2013 in an effort to

reduce CO2 emissions. The Commission Regulation (EU) No 327/2011 limits the minimum efficiency of fans driven by motors with an electric input power between 125W and 500kW (Council, 2011). Consequently, quiet operation and a high aerodynamic efficiency are becoming increasingly important when selecting of ventilation fans (Xiang Hua et al., 2012). However, most ventilation fans available in the market tend to have a poor aerodynamic efficiency and high noise levels. This can be partially attributed to the widely applied design methods based on trial and error approaches. ***A review on fan design methods suggests that a comprehensive design approach is needed to fill in the gaps that still persist in the literature, particularly considering both aerodynamic and noise performances***. To this end, a new comprehensive fan design approach is presented as part of this research to design low pressure axial fans with low noise and a high aerodynamic efficiency. The novel aspect of this approach is that it presents a clear, concise, and well-thought-out quantitative approach for the design of low speed quiet ventilation fans. The design approach is limited to the widely used rotor-only configuration with no fixed vanes or diffuser. The main function of these fans is to generate flow with minimum losses from friction, flow separation, and secondary flows (Wallis, 1983). To this end, these fans are designed to function within a low static pressure environment for the purpose of pulling or pushing air in large volumes at low cost, i.e. low pressure rise fans. Therefore, the main metrics of interest in this research are volumetric flow rate, sound power level, mechanical power, and aerodynamic efficiency.

The main premise of this research effort is that reducing the fan speed while maintaining a high aerodynamic efficiency will result in significant noise reduction. This approach is justified considering that the fan aerodynamic noise sources scale directly with the 4-6th power of the fan speed. To this end, two approaches are implemented to improve the aerodynamic characteristics of the fan blades to reduce the fan speed and noise while maintaining a high aerodynamic efficiency. First, a control vortex design (CVD) approach is used to design the blades. The CVD approach is used to better design the axial and swirl velocity distributions along the blade span to improve the contributions of the blade outer sections. This allows for a reduction of the fan tip speed and noise while reducing the complexity of the blade, i.e. the chord and twist distribution are reduced along the blade. This resulting blade geometry is ideally suited to implement multi-element airfoils that can further reduce the fan speed. Multi-element airfoil configurations

outperform single element airfoils by preventing flow separation and subsequent stall that lead to higher lift characteristics. Figure 1.1 shows the flow around a single element and a multi-element airfoil. As illustrated here, the flow remains attached in the multi-element configuration due to the accelerated flow in the gap that increases the kinetic energy of the flow on the suction surface of the subsequent airfoil (Roy et al., 2009). Consequently, the use of multi-element airfoils in a tandem configuration has been previously investigated to improve the aerodynamic characteristics of compressor blades by several authors (Bammert and Beelte, 1980; McGlumphy, 2008; Saha and Roy, 1997). ***However, to the best of the author's knowledge, multi-element airfoils have not been previously investigated for rotor-only low-pressure axial ventilation fans considering both aerodynamic performance and noise***.

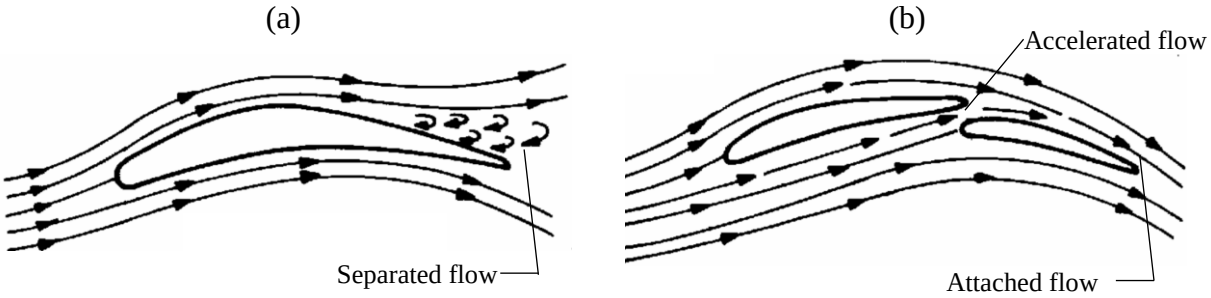

Figure 1.1: Flow field streamlines around **(a)** Single element, and **(b)** Multi-element airfoil showing separated flow characteristics for the same AoA, taken from Roy et al. (2009).

The current trend in the fan industry is to use BLDC motors to drive the ventilation fans. This is due to the higher efficiency, higher power density, and lower weight relative to other variable speed drivers (Yong-Han et al., 2006). However, significant motor noise can arise from the electro-magnetic forces and motor housing (Cho, 2018). The work in this dissertation is only focused on reducing aerodynamic noise and not the BLDC motor noise. Thus, for the experimental part of the work, off the shelf BLDC motors are used. To this end, several candidate motors with suitable characteristics have been experimentally evaluated for noise. The quietest motor was implemented for the experiments.

The focus of the experimental work is to validate the aerodynamic tools used in the design process and to gain insight into sources of noise in fans designed with multi-element airfoils. Additionally, the data collected for fans designed with multi-element airfoils is provided as a first step towards future acoustic prediction tools that can be used for multi-element airfoil fans.

1.1 Objectives

The main aims of this work are to develop and experimentally demonstrate a comprehensive approach for the design of rotor-only low-pressure axial ventilation fans considering aerodynamic performance and noise. To this end, the main contributions from this work are:

- A new comprehensive design approach for rotor-only low-pressure axial ventilation fans considering both aerodynamic performance and noise. This innovation addresses gaps in the literature regarding the design of low-pressure axial ventilation fans. To this end, a clear, concise, and well-thought-out method for the design of low speed quiet ventilation fans is presented that can be easily implemented by fan designers.

- The first implementation of multi-element airfoils in the design of low-pressure axial ventilation fan blades in the open literature. Multi-element airfoils are implemented to enable lower fan speeds and noise while maintaining aerodynamic efficiency.

- A new multi-fan unit concept is designed and experimentally tested as a practical implementation of the innovations proposed here.

1.2 Organization

The remaining chapters of this dissertation are organized as follows.

Chapter 2 reviews aerodynamic and acoustic performance of commercial fans. The dominant sources of noise are identified as their dependence on the fan speed is presented. An overview of the most widely used theories for the design of rotor only axial fans is presented.

Chapter 3 described the aerodynamic and acoustics tools used in the design process developed as part of this research effort. The acoustic tools consider both rotor-self noise and boundary layer (BL) turbulence rotor interaction noise, i.e. the dominant sources of noise in rotor-only axial fans.

Chapter 4 introduces a new comprehensive design approach considering both aerodynamic performance and noise. The fan design is a stepwise approach that implements a multi-objective genetic algorithm to design the blade geometry to generate a given volumetric flow rate at the minimum fan tip speed. The comprehensive design approach is applied for the design of the first fans in the open literature implementing multi-element airfoil geometries.

Chapter 5 experimentally evaluates the innovations proposed here using a test rig designed and implemented as part of this research effort. The prototype fans are used to validate the aerodynamic design and acoustic prediction tools used in the design process. Additionally, data pertaining to fans designed with multi-element airfoils is provided as a first step towards future acoustic prediction tools for the design of multi-element airfoil fans. The performance of fans designed with single and multi-element airfoils are compared to evaluate the potential benefits of multi-element airfoils.

Chapter 6 describes the mechanical design of the first multi-fan unit as a practical implementation of the innovations developed in this research. The focus here is at providing an overall picture of the trends related to the addition of multiple fans connected in parallel.

Chapter 7 describes the overall conclusions and outlines potential future work.

CHAPTER 2

2 Literature review

The aim of this chapter is to review the characteristics of noise generation in axial ventilation fans in an effort to understand tradeoffs between fan noise and aerodynamic performances. To this end, a broad overview of the aerodynamic and acoustic performance of commercial ventilation fans is first assessed in order to stablish a baseline understanding of design trends in the fan industry. The collected data related to the fan aerodynamic and acoustic performance from well-established datasheets published by the fan manufacturers is presented in Section 2.1. The sources of noise in axial ventilation fans and their dependence on the fan speed are reviewed in section 2.3. The historical development of widely used theoretical principles for the aerodynamic analysis of fans is presented in Section 2.3. Lastly, Section 2.4 presents a historical development of the methods implemented to design axial ventilation fans.

2.1 Current state of the ventilation fan industry

Ventilation fans are commonly used across many industries for a wide range of applications. Figure 2.1 shows three different applications for rotor only axial ventilation fans. As illustrated here, ventilation fans can vary in size depending on the performance requirement, i.e. volumetric flow rate, efficiency and noise. To this end, an extensive review of rotor only ventilation fans has been carried out in an effort to benchmark the current state of the ventilation fan industry. The review is limited to low pressure axial ventilation fans with a diameter ranging from 30 to 80 cm. Data has been collected from 80 commercial ventilation fans from various well-known manufacturers. In the figures presented below, the size of the data circles is proportional to the diameter of the fan. The diameter of selected fans is also noted in the figures. The manufacturers' data was taken at face value and, thus, its accuracy not independently assessed.

(a) (b) (c)

Figure 2.1: Ventilation fans used in **(a)** manufacturing (Power-Star-Electrical, 2019), **(b)** Construction (Industries, 2019), and **(c)** road tunnels (cybernetics;, 2019).

Since the fan noise data provided by the manufacturer is in terms of sound pressure level at a given distance (different for each manufacturer), the sound power level was estimated as

$$L_w = L_p\left(R\right) + 10\log_{10}\left(4\pi R^2\right) \quad [dB] \tag{2.1}$$

where $L_p(R)$ is the sound pressure level provided by the manufacturer at a distance, R.

Figure 2.2 shows the commercial fan volumetric flow rate as a function of the fan speed (RPM). As illustrated here, fans can be designed for a high volumetric flow rate by increasing the fan speed and/or increasing the fan diameter. However, a trade off exists between the fan speed and noise. Figure 2.3 plots the fan noise as a function of the volumetric flow rate. As illustrated here, the trend to design fans with a high volumetric flow rate at low noise levels is to increase the fan diameter. However, workplace constraints can significantly restrict the fan size. Consequently, smaller fans are often implemented while compromising for higher speeds and noise levels. Therefore, there is a need for quiet, compact ventilation fans with a high volumetric flow rate.

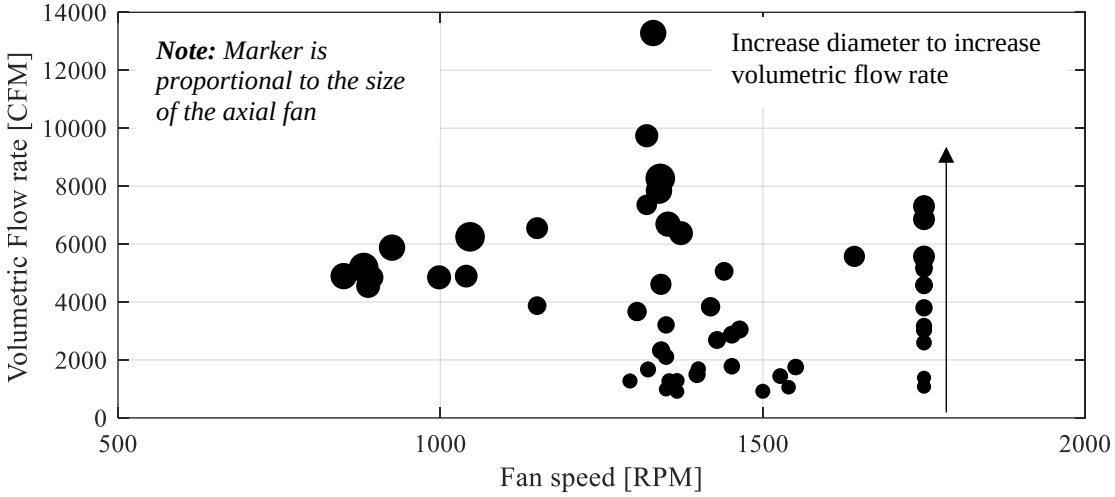

Figure 2.2: Trend in the volumetric flow rate output for commercial fans as a function of the fan design speed-Data collected from published manufactured data.

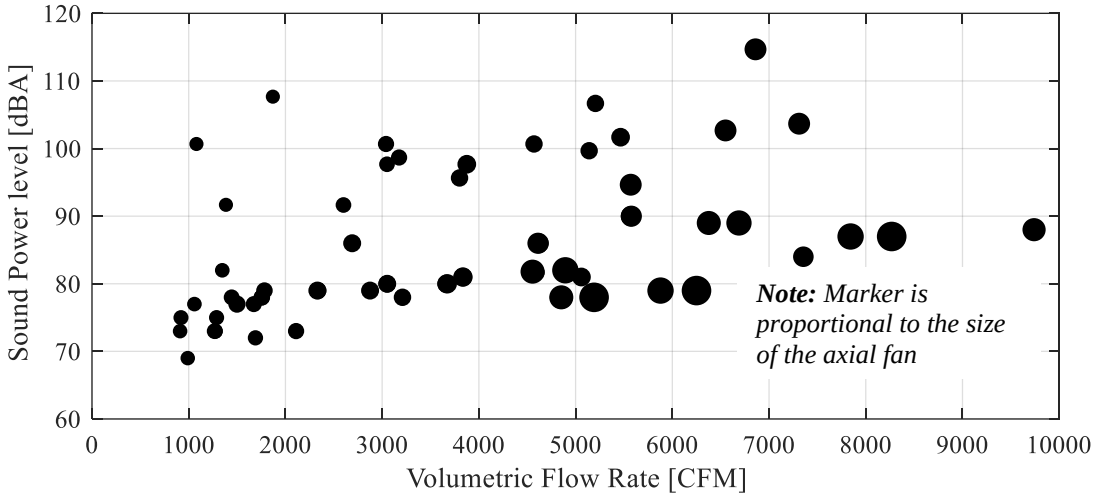

Figure 2.3: Sound power level for commercial ventilation fans at the design speed as a function of the output volumetric flow rate- Data collected from published manufactured data.

To better display trends of commercial fans with different sizes, the data was normalized and replotted. The sound power was normalized by the fan cross sectional area to give the sound intensity (sound radiated per unit area). The sound intensity level ($L_I(dB)$) is computed as

$$L_I\left(dB\right) = L_w\left(dB\right) - 10\,Log_{10}\left(\frac{\pi D^2 \times 2}{4}\right)\ [dB] \qquad \textbf{(2.2)}$$

where D is the fan diameter [m].

The fan speed was normalized by the size of the fan to give the fan tip speed. The fan tip speed is computed as

$$M_{tip} = \frac{D\Omega}{2c_{air}} \tag{2.3}$$

where Ω is the fan speed [*rad/sec*] and c_{air} is the speed of sound [*m/s*]. In addition, fan efficiency is also plotted. The fan aerodynamic efficiency is defined here as the ratio of the power imparted to the fluid divided by the shaft power (Sforza, 2012). It is computed as

$$\eta_m = \frac{1/2\,\dot{m}\bar{V}_a^2}{P_{shaft}} \tag{2.4}$$

where $\dot{m}$ is the mass flow rate [kg/s], $\bar{V}_a$ is the area average axial flow velocity [m/s], P_{shaft} is the shaft power [watts]. The area average axial flow velocity ($\bar{V}_a$) is computed by dividing the reported volumetric flow rate by the annulus area, $A = \pi(R^2 - r_h^2)$. Where R is the fan radius and r_h is the hub radius. Since the radius of the hub (r_h) is not readily provided by the manufacturer, it is estimated here by analyzing the picture of the rotors. Additionally, the shaft power is assumed to be equal to the electrical power, i.e. efficiency of the motor not accounted for. This introduces uncertainties in the computation of the fan efficiency. Consequently, the fan efficiency computed using Equation (2.4) represents a rough estimate only (lower than actual), i.e. it is not accurate and it is intended for illustration purposes only. Figure 2.4 shows the efficiency of the commercial fans as a function of fan tip speed. It is evident here that the size of the fan does not have a direct relationship with the fan efficiency. However, a linear curve fit of the data shows that the fan efficiency increases with the fan tip speed.

Figure 2.5 shows the sound intensity level as a function of the fan tip speed. The clear trend is that fans designed for low noise have a larger diameter. However, it can be observed that the data collapses better than in Figure 2.3 and a clear dependence of the noise with tip speed is evident. The sound intensity levels increase significantly with fan tip Mach number as shown by the linear regression. Figure 2.4 and Figure 2.5 show that an increase in the fan tip speed results in an increase in the fan efficiency and noise. Hence, the tradeoffs between fan noise and efficiency are evident. Consequently, both efficiency and noise must be accounted for in the design process for fans.

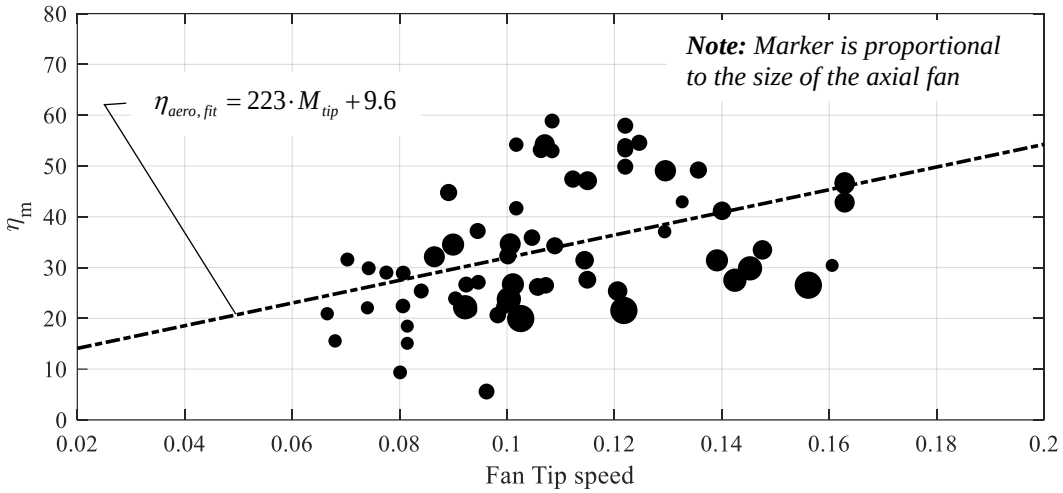

Figure 2.4: Estimated aerodynamic efficiency for commercial fans as a function of the fan tip speed - Data collected for commercial for ventilation fans.

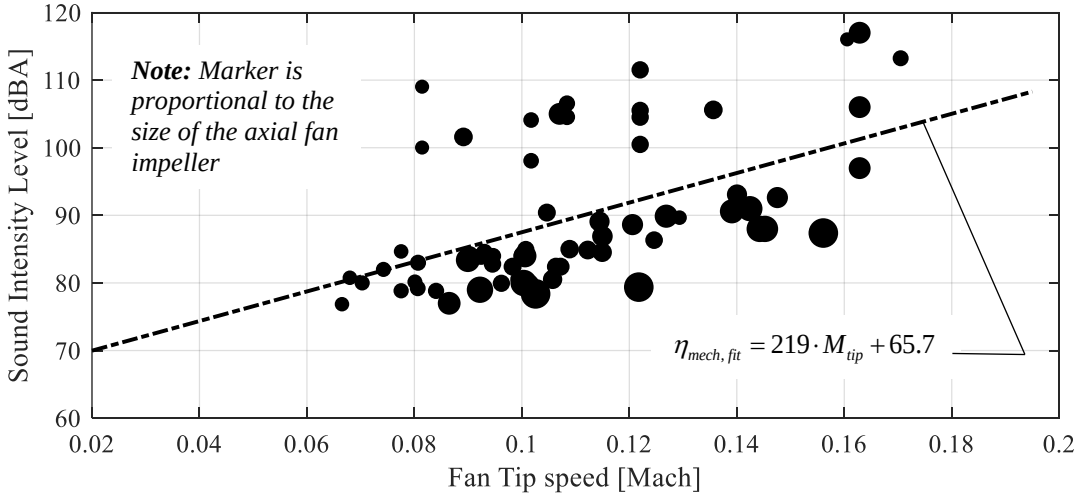

Figure 2.5: Fan overall A-weighed sound intensity level for commercial fan as a function of fan tip speed - Data collected from published manufactured data.

2.2 **Dominant sources of noise in axial flow fans**

The typical fan noise spectrum is composed of broadband and discrete tones as shown in Figure 2.6(a). The dominant discrete tones noise occur at the blade passage frequency (f_{BPF}) and harmonics. The BPF is

$$f_{BPF} = \frac{n * N_B}{60} \quad [Hz] \tag{2.5}$$

where *n* is the fan speed [RPM] and N_B is the number of blades.

However, the human ear does not have a flat frequency response. To account for the human perception of sound at different frequencies, A-weighting is used as illustrated in Figure 2.6(b), Although the A-weighting narrowband spectrum is preferred in this research, in engineering applications it is common to present the fan noise spectrum in 1/3rd octave bands. In addition, fan noise in 1/3rd octave bands is widely applied in environmental and noise control applications to stablish noise regulations. Therefore, noise results are presented in narrowband and 1/3rd octave bands when appropriate. Figure 2.7 shows the 1/3rd octave band spectrum for the fan in Figure 2.6.

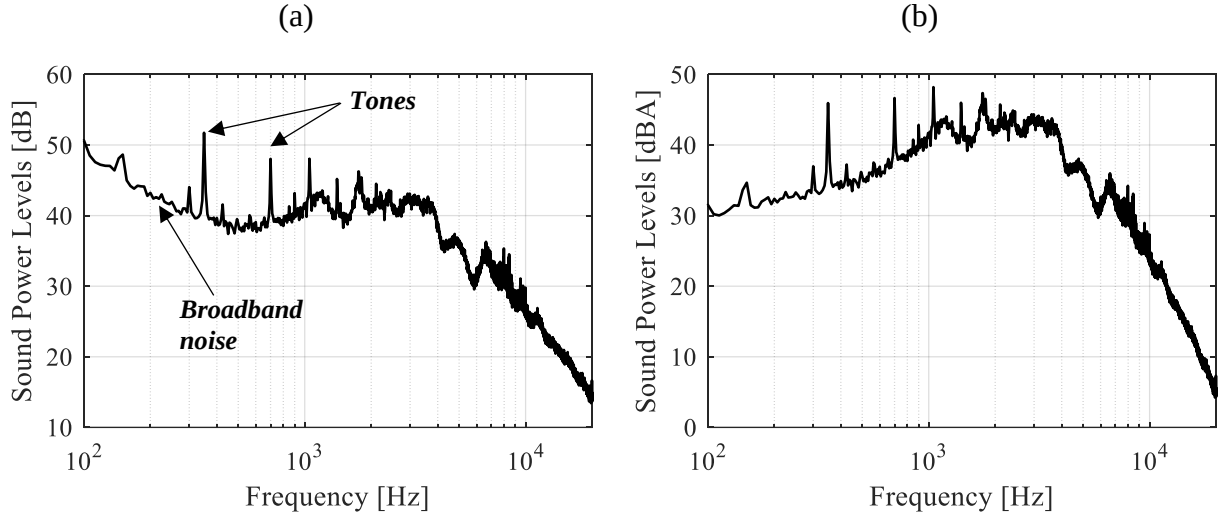

Figure 2.6: Fan noise spectrum **(a)** Z-weighted and **(b)** A-weighted for a 7 blades fan (186mm diameter) at a fan speed of 3000 RPM, i.e. BPF of 350 Hz.

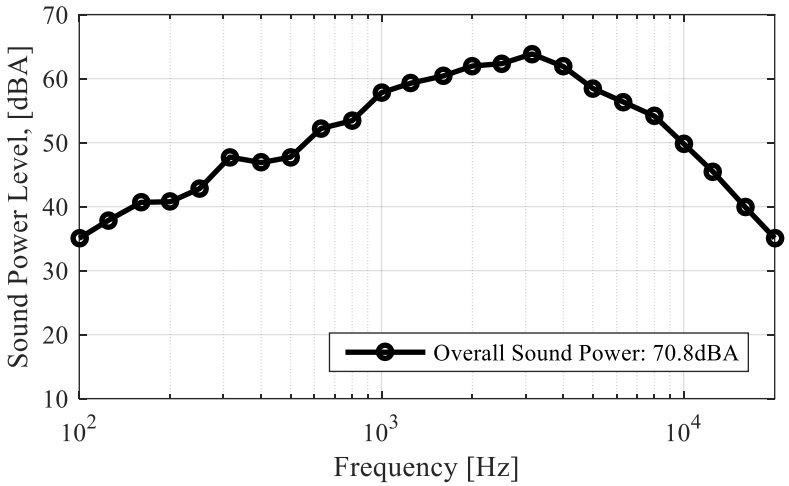

Figure 2.7: Fan noise in 1/3rd octave bands for a 7 blades fan (186mm diameter) at a fan speed of 3000 RPM, i.e. BPF of 350 Hz.

The most significant sources of aerodynamic noise for rotor only axial fan configurations are well documented by several authors (Neise and Michel, 1994; NIEKERK, 1965; Wright, 1976) and illustrated in Figure 2.8. The tonal sources of noise are due to rotor-strut interaction, steady blade loading, and steady blade thickness noise. Steady loading on the blades occurs when the fan operates in clean axisymmetric steady flow. The steady lift and drag forces are perceived as harmonic pressure fluctuations (noise) at the observer location due to the rotation of the blades. Steady loading noise scales with the 6^{th} power of the fan tip speed. Blade thickness noise is generated from the periodic pressure fluctuations created by the displacement of air by the rotating blade (Marte and Kurtz, 1970; Moreau and Guérin). Blade thickness noise scales approximately by the 4^{th} power of the fan tip speed. Lastly, tones are also generated from several possible rotor-strut interaction noise mechanisms. First, the perturbation field of the downstream strut can trigger unsteady pressure fluctuations on the upstream blades that can radiate noise. Secondly, the interaction of the rotor wakes with the downstream struts results in unsteady aerodynamic forces that generate noise (Nakamura et al., 1986). The rotor-strut interaction noise scales with approximately the 6^{th} power of the fan tip speed.

The broadband sources of noise are tip-gap noise, turbulence ingested noise interacting with the rotor, boundary layer (BL) turbulence interacting with the rotor, airfoil self-noise, and rotor wake turbulence interacting with the strut. Two mechanisms are possible for the generation of tip gap noise. First, tip-gap noise can be generated from the leakage flow driven from the pressure to the

suction side of the blade as shown in Figure 2.9 (Fukano et al., 1986). The resulting vortex system is characterized by a considerable degree of unsteady pressure fluctuations that results in noise. As the tip gap gets larger, the vortex strength and noise increases (Fukano et al., 1986). Second, ingested turbulence from the duct wall BL and atmospheric turbulence results in noise from the interaction of the turbulence eddies with the leading edge of the airfoil (Majumdar and Peake, 1998; Mugridge and Morfey, 1972). The incident turbulence interaction noise scales with approximately the 6^{th} power of the fan tip speed and the 2^{nd} power of the airfoil chord (Hutcheson et al., 2012).

Self-noise is generated from the interaction between an airfoil blade and the turbulence produced in its own BL (Brooks et al., 1989). Self-noise is a combination of fundamentally different sources occurring in different regions of the airfoil. Since they do not interfere with each other, they are considered independent noise sources (Jianu et al., 2012). They are Turbulent BL trailing-edge noise, Laminar BL vortex-shedding noise, Separation-stall noise, Trailing edge bluntness vortex-shedding noise, and Tip vortex formation noise (Brooks et al., 1989).

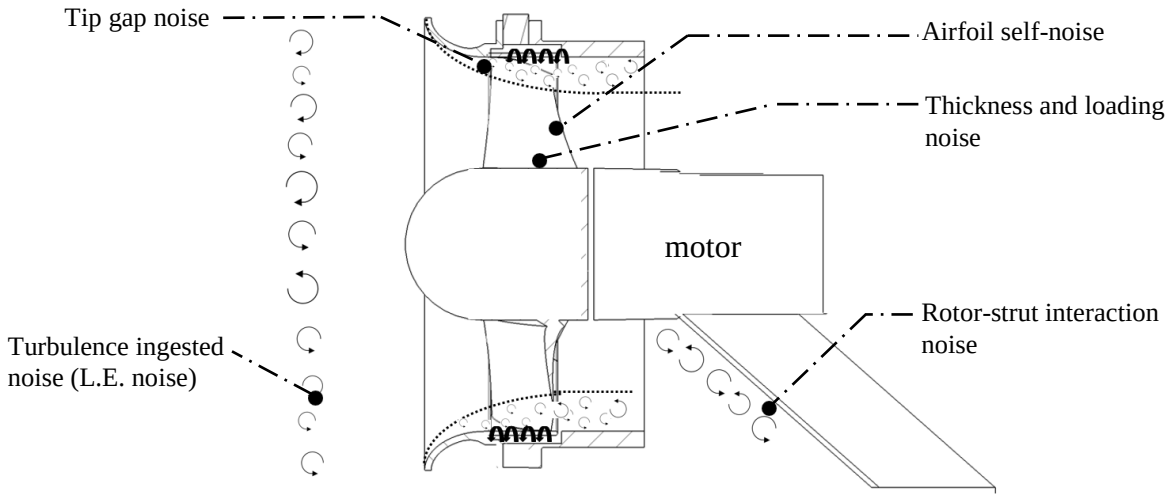

Figure 2.8: Major noise-generating mechanisms in ducted rotor only axial flow fans. Noise sources scale with the 4-6^{th} power of the fan tip speed.

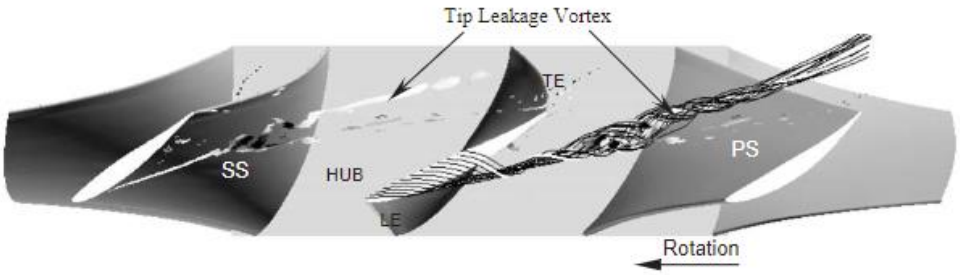

Figure 2.9: Tip vortex generating mechanism illustration. Leakage flow driven from the pressure side to the suction side of the blade results in the tip leakage vortex, taken from Fukano (1986).

The design features of commercial ventilation fans show that improvements in the design process can significantly reduce noise. Some of the poor design features on a common ventilation fan are illustrated in Figure 2.10. It is evident here, that the fan operating in the wake of the motor and struts results in high leading edge noise. Additionally, the rotor-strut interaction noise is amplified by the close proximity of the struts and large motor to the blades. The tip gap is also very large (> blade thickness) and the flanged inlet generates a thick BL that result in a high tip gap noise and duct BL turbulence interacting with rotor. Lastly, the thick airfoil sections and trailing edge of the blades are a dominant source of broadband airfoil self-noise. Consequently, it is evident here that fan design procedures considering aerodynamics and acoustics can significantly improve aerodynamic efficiency and reduce noise levels in axial ventilation fans.

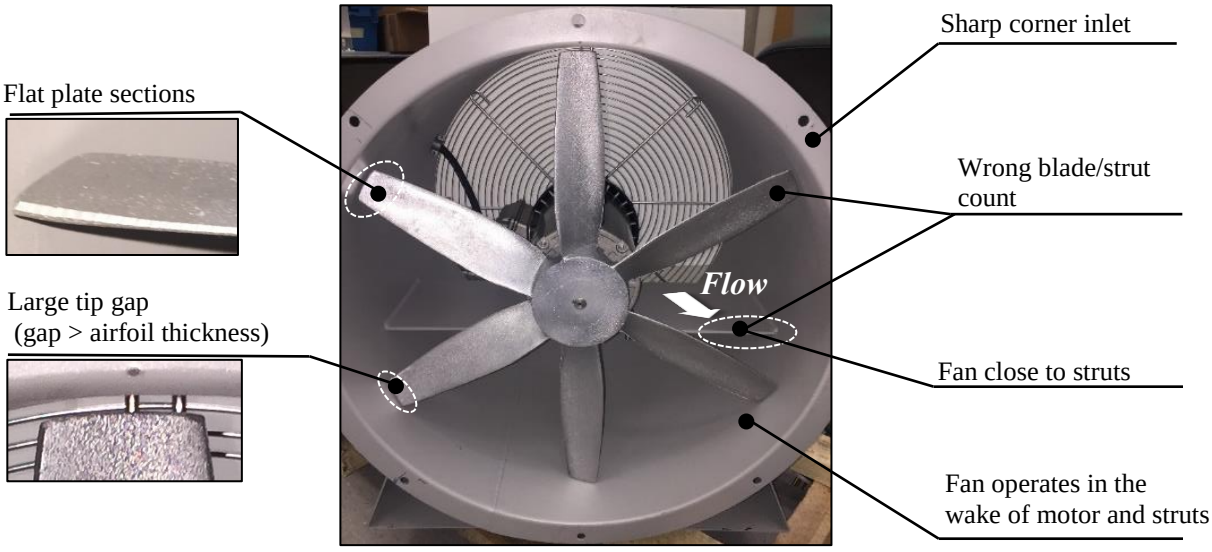

Figure 2.10: Typical features in commercial fans that deteriorate the aerodynamic efficiency and increase noise levels.

2.3 Brief Historical Review of Aerodynamic Theories

The first aerodynamic model that was used to guide the design of axial fans was the turbine equation. Euler derived the turbine equation in 1837 from the conservation of energy and angular momentum. The turbine equation relates the change in swirl velocities (v_θ) through the rotor with the torque required to drive the fan.

The design of axial fans was further improved with the introduction of the axial momentum theory (also known as the actuator disk theory) by Rankine in 1885 for the use of marine propellers. The axial momentum theory was later developed by Froude in 1889. The momentum theory is a global analysis of the conservation of mass, momentum, and energy of a propeller in a control volume. The major contributions for the axial momentum theory is that it allows for the calculation of the ideal efficiency as the ratio of the work done to the fluid to the available power. Consequently, momentum theory is a very useful theory for estimating the necessary power to operate a fan. Additionally, it can be used to estimate the size of the fan to generate a given flow rate.

The axial momentum theory does not take into account the blade geometry, number of blades, or airfoil characteristics. Consequently, Blade Element Theory (BE) was proposed by Froude and Drzewiecki (Drzewiecki, 1892) as a solution. BE theory assumes that each blade section behaves as a 2D airfoil generating aerodynamic lift and drag forces. The blades are divided into individual sections with velocity vectors acting on the airfoil. The thrust and torque can then be determined by integrating the normal and tangential forces along the blade.

One key issue with the BE theory is that it does not account for the induced velocities by the rotor. Consequently, BE theory assumes that as the drag approaches zero the efficiency becomes unity. This created discrepancies with the induced efficiency derived from momentum theory. The blade element momentum (BEM) theory proposed by Glauert (Glauert, 1926) solved this discrepancy by combining the blade element theory with the momentum theory to compute the induced velocities at the rotor. Numerically intensive methods such as vortex theory and computational fluid dynamics can be used for the design of rotors. However, tradeoffs between accuracy and computational effort make the BEM method a more practical way to analyze and design rotors. It

is still the most widely used method today for the design of rotors and turbines. This approach was used in this dissertation and presented in more detail in Chapter 3.

2.4 Brief Historical Review of Fan Design Methods

The first known documented design of a ventilation fan dates back to 1827 in Paisley, Scotland for mining applications (Cory, 2005). Without aerodynamic theories, these designs consisted of empirical trial and error methods. With the development of the aerodynamic theories presented in section 2.3, aerodynamic design methods achieved a more definite form in the 1930's (Castegnaro, 2018). The purpose of fan design methods is to determine the fan size (diameter and hub-to-tip ratio), blade geometry (chord and twist distribution), and blade cross sectional area (airfoil) to meet the design requirements. The first known guidelines for the design of axial flow fans are credited to Keller (1934). The work of Keller was widely distributed after the translation by Weske and Marks (1937). A key assumption implemented by Keller is that of uniform axial velocity and pressure rise along the blade span, i.e. free vortex design (FVD). The FVD is characterized by a tangential velocity that is inversely proportional to the radius. The design approach assumes isolated airfoil characteristics (no mutual interference between adjacent blade elements) and that the lift coefficient and number of blades are known. Using this information and the flow angle, the angle of attack (AoA) for the given lift coefficient can be used to determine the blade chord and twist at a given radial position. The process is repeated for all radial positions to get the chord and twist distribution along the blade span (Keller, 1934; Keller et al., 1937).

An assumption for the blade loading different from free-vortex is a challenge given that it can result in radial induced velocities if not properly designed, i.e. 3D flow. Consequently, free-vortex design is the most widely used method. However, it is possible to design blades with non-free vortex loading that result in flow with 2-dimensional characteristics. The first fan design approach of this kind was implemented by Ruden (1944) for the design of single-stage axial fans for a wind tunnel in Göttingen, Germany. Here, the relation between the axial and swirl velocity distributions to maintain radial equilibrium (2D flow characteristics) along the blade span are derived from direct integration of the Euler equations. To this end, the blades are loaded so that the centrifugal force due to the rotation of the fluid is balanced by a pressure gradient, or

$$\frac{\partial p}{\partial r} = \rho_{air} \frac{v_\theta^2}{r} \quad \left[\frac{Pa}{m}\right] \tag{2.6}$$

where ρ_{air} is the air density [kg/m^3], p is the static pressure [Pa], r is the radial spanwise position [m], and v_θ is the swirl velocity [m/s].

Using this approach, Ruden designed three fans with different spanwise chord distributions; decreasing, constant, and increasing along the blade span. Experimental investigations on these rotors showed that rotors with an outwardly increasing chord are more suitable for higher blade loadings due to the increasing axial velocity along the blade (Castegnaro, 2018; Ruden, 1944). In 1947, Kahane implemented the approach described by Ruden to design two non-free vortex fans with a high pressure rise. One with an approximately constant swirl-velocity ($v_\theta \approx const$) and the other with a forced vortex distribution ($v_\theta = const \cdot r$). Both fans employed a high hub-to-tip ratio of 0.69 with a NACA-65 series airfoil. The forced vortex design is characterized by a radially increasing swirl velocity along the blade that results in a large chord at the blade tip that radially decreases towards the blade root. The approximately constant swirl velocity distribution resulted in a nearly constant chord along the blade span. Kahane tested the measured radial pressure gradient for the two fans in Figure 2.11 against radial equilibrium equation (Equation (2.6)). As illustrated in Figure 2.11, theory agrees very well with experimental data. Consequently, it is concluded that non-free vortex methods can be used in conjunction with two dimensional airfoil data with sufficiently accurate results.

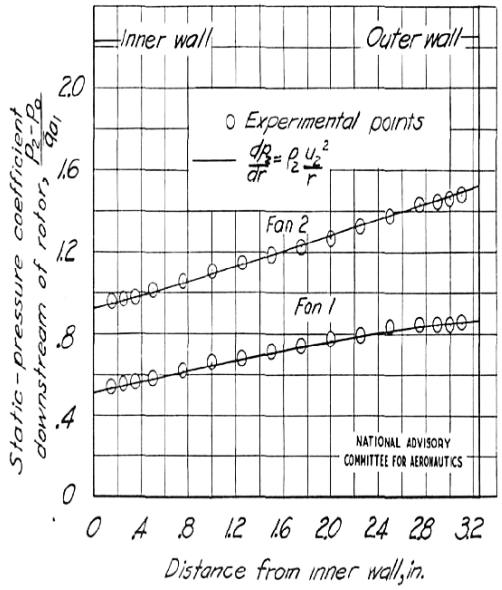

Figure 2.11: Static pressure coefficient along the blade span for a rotor designed with approximately constant swirl loading (Fan 1), and with a forced vortex loading (Fan 2), taken from Kahane (1947) . Experimental data shows excellent agreement with the radial equilibrium equation.

In 1953, Cordier carried out an extensive analysis of experimental data pertaining to efficient fans, blowers, and pumps. The empirical analysis correlated the optimum operating conditions (flowrate, pressure rise) of fans with two parameters that can readily describe the performance of the turbomachine for assessment, selection, and comparison. The two parameters are the speed number (σ_n) and the diameter number (δ_n) defined as

$$\sigma_n = 2\sqrt{\pi n}\,\frac{\sqrt{\dot{V}}}{(2Y)^{3/2}} \tag{2.7}$$

$$\delta_n = \frac{\sqrt{\pi}}{2} D^4 \sqrt{\frac{2Y}{\dot{V}^2}} \tag{2.8}$$

where $Y = \Delta p / \rho_{air}$, $\dot{V}$ is the volumetric flow rate, and Δp is the pressure rise.

Figure 2.13(a) shows the data collected by Cordier for fans, blowers, and pumps in terms of the speed number and the diameter number in a logarithmic plot. As illustrated here all of the data collapses to a well-defined line (Cordier line) reproduced in Figure 2.13(b). Deviation from the Cordier line represents a decrease in efficiency as illustrated by the efficiency contours in Figure 2.13(a). In addition, Figure 2.13(a) shows the lines for the optimum pressure coefficient ($\psi_{opt} = \Delta p / 0.5\rho_{air}(\Omega R)^2$). These lines indicate that impeller designs for low pressure coefficients

with a higher efficiency are better achieved with high speed numbers and low diameter numbers, i.e. axial flow fans as shown in Figure 2.13(b). The Cordier line is widely used in the fan design process is two different ways. First, the Cordier line is used to determine the maximum fan diameter with a known rotational speed. Second, for a fixed diameter it is used to determine the fan speed. However, this approach is not encouraged by some authors (Osborne, 1966; Wallis, 1983). The physical explanation of the Cordier line is that there is an optimum velocity triangle that can achieve the required design point (flow-rate and pressure rise) with the highest efficiency (Castegnaro, 2018)

(a) (b)

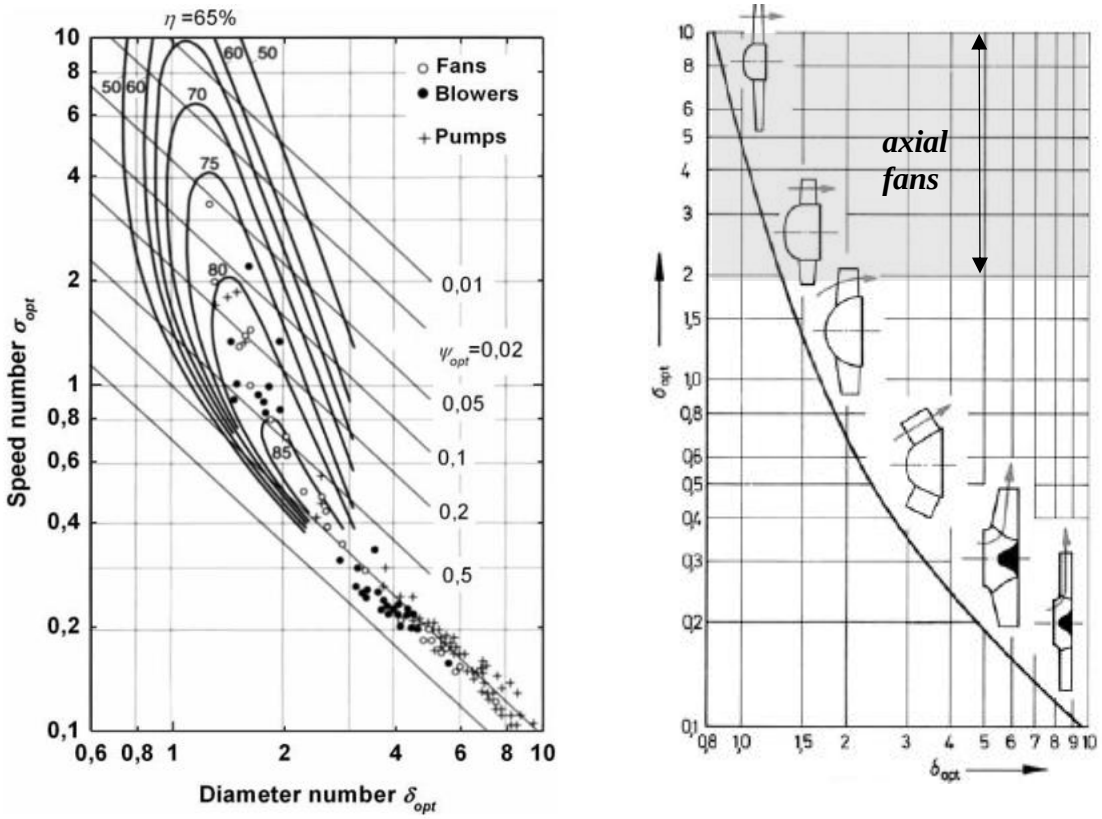

Figure 2.12: (a) Original performance diagram for fans, blowers, and pumps in terms of the speed number and the diameter number by Cordier (1953), and **(b)** the Cordier line representing "optimum" fans with a high efficiency, captured by Cordier (1953) and reproduced by Bohl and Elmendorf (2008).

In 1961, Wallis published his book on axial flow fans which has become a standard in the fan design literature. The book presents guidelines for the design of axial flow fans for a given operation point, i.e. pressure rise, volumetric flow rate. The design approach involves first using trial and error method to establish the best overall dimensions of the fan (fan diameter and hub to tip ratio) and the fan speed. Once these parameters are determined, the radial distribution of the

flow velocity can be obtained using one of two proposed methods. The first is the classical free vortex method characterized by a constant axial velocity distribution. The second implements an arbitrary vortex approach. The arbitrary design is an intermediate swirl velocity distribution that is between that of a free vortex distribution and a forced vortex distribution, i.e. between $v_\theta = const \cdot r^{-1}$ and $v_\theta = const \cdot r^{1}$). Figure 2.13 compares the resulting chord distribution for the free vortex, forced vortex, and arbitrary vortex (in between the other two) designs. As illustrated here, they result in significantly different blade geometries. The non-free vortex design by Wallis was largely based on the experimental success of Kahane (1947). Consequently, Wallis recommended caution using the non-free vortex designs pending further experimental validations. The experimental validation was carried out later by Downie et al. (1993) using two 0.610 m diameter fans employing an arbitrary vortex design with a hub-to-tip ratio of 0.38. Results by Downie confirmed the findings by Kahane that two-dimensional design methods can be used for the design of non-free vortex fans while the radial equilibrium equation is satisfied.

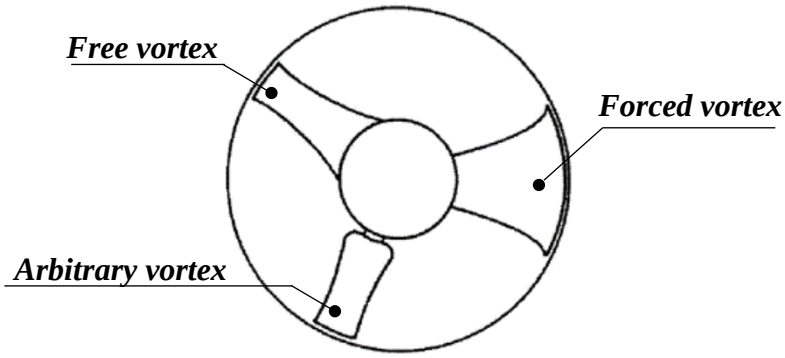

Figure 2.13: Blade geometry shape resulting from a free vortex, force vortex and arbitrary vortex loading designs, taken from Cory (2005).

Most authors advocate the use of the free vortex loading due to the resulting simplifications in the design process. However, non-free vortex designs can result in smoother chord and twist distributions while achieving similar efficiencies (Wallis, 1983). However, tip losses can increase considerably for non-free vortex designs. Consequently, the gap should be kept at minimum to avoid significant losses and noise in non-free vortex fans.

In light of the preceding findings by Wallis and Kahane, the design of axial flow fans employing non free vortex loading distributions has gained popularity in recent years with many different

methods being developed. In an effort to compare fans designed with different vortex criteria, Castegnaro et al. (2017) carried out an extensive review of over 25 different fans designed with different swirl velocity distributions. The experimental efficiency of the rotor-only fans with different vortex distributions is presented in Figure 2.14 in terms of the speed number and diameter number, i.e. Cordier diagram format. The vortex distributions have been grouped into three groups: free vortex, forced vortex, and arbitrary vortex. It is evident from Figure 2.14 that fans with and without the free vortex criteria can be designed to achieve a high efficiency, i.e. all fan types are in close proximity to the Cordier line. Additionally, Figure 2.14 shows that fans designed with arbitrary vortex tend to have higher specific speeds, i.e. they generate higher flow rates at a lower pressure rise relative to the free vortex and forced vortex designs. Therefore, the arbitrary vortex is expected to have comparable efficiency to free vortex while also generating more volumetric flow rate at a given tip speed.

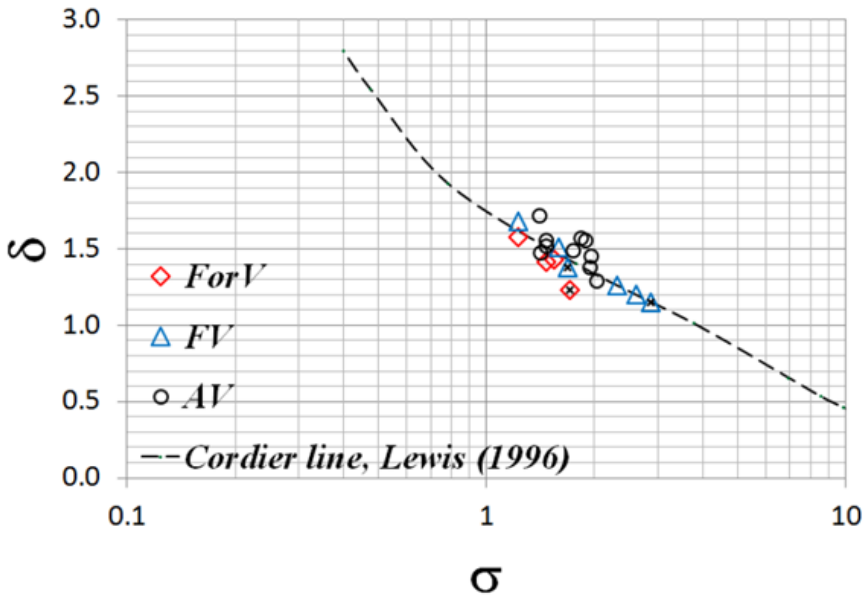

Figure 2.14: Speed number (σ_n) and diameter number (δ_n) comparison of fans designed with a free vortex (FV), Forced vortex (ForV), and Arbitrary vortex (AV) loading with the Cordier line (shown in Figure 2.13). Taken from Castegnaro et al. (2017).

One of the key benefits of arbitrary vortex designs is the re-distribution of the solidity to higher radii to increase the volumetric flow rate and pressure rise of the blade designs. An increase in solidity allows for a high blade loading and hence a higher volumetric flow rate contribution. However, the blade loading can also be increased by using airfoils with higher lift coefficient. One

method for increasing the lift coefficient involves using multi-element airfoils. The use of multi-element airfoils in turbomachines was first proposed by Karl Stahl in 1924 under US patent 1,742,792 as illustrated in Figure 2.15. This invention consist of a single airfoil with a slit that would be equivalent to a two-element or tandem airfoil(Stahl, 1924) (Stahl, 1924). The patent describes this invention as having an advantage in efficiency relative to a normal propeller. Stahl justified the increased in efficiency by the additional force generated by the slit relative to ordinary blades. The use of a tandem configuration have also been investigated by several authors to improve the aerodynamic characteristics of compressor blades (Bammert and Beelte, 1980; McGlumphy, 2008; Saha and Roy, 1997). Additionally, multi-element airfoils have been recently implemented in the design of horizontal blade turbines. However, after an extensive review, tandem airfoils have not been implemented into axial low speed axial fans. This can be attributed to the lack of information regarding the performance of tandem airfoils at low Reynold numbers (Re <500,000).

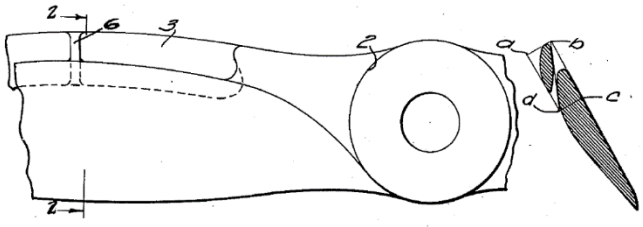

Figure 2.15: First proposed multi-element blade for improving the aerodynamic performance of impellers, US patent 1,742,792 tiled "Air propeller" by Stahl (1924).

From the review here of design methods, there is a need for a method for selecting the best vortex criteria for a given design. It should also be noted here, that none of these design methods reviewed address fan noise in the design, i.e. the focus is on achieving a high aerodynamic efficiency and pressure rise. ***However, the need for incorporating fan noise into the fan designs is obvious and a short-coming of existing fan design methods including using multi-element airfoils.***

CHAPTER 3

3 Aerodynamic and Acoustic Design Tools

This chapter describes the aerodynamic and acoustic tools used to guide and implement the fan design approach. To this end, the aerodynamic code implemented to analyze the aerodynamic characteristics (polars) of different multi-element airfoil geometries is first described in section 3.1. The code used for this task is MSES. The airfoil characteristics are used for the design of the blade geometry using XROTOR. The theoretical background of XROTOR is briefly described in Section 3.2. Two noise prediction codes are implemented in this research and presented in section 3.3. These acoustic tools are used to gain insight into the rotor self-noise (RSN) and boundary layer (BL) turbulence rotor interaction noise (BLTRIN) sources. These noise sources are the ones dominating the acoustic signature of the fans. The BLTRIN requires BL data. To this end, the duct analysis program, DFDC, is used to estimate the BL characteristics. The code DFDC presented in Section 3.4 is also used to design the duct geometry to maximize the performance of the fan while indirectly minimizing noise by reducing the BL thickness.

3.1 Airfoil Polars

The code MSES, developed by Mark Drela (Drela, 2007a) at MIT, was chosen for the analysis of the airfoil aerodynamic characteristics in the absence of experimental data. This code was primarily used in the calculations of the lift and drag polars for the multi-element airfoils. MSES is an inviscid-viscous solver with an interactive framework consisting of several programs used for the analysis, design, and optimization of airfoil geometries. In this work, the main programs used are MSET (grid generation program), MSES (Flow solver), and MPOLAR (version of MSES that sweeps through a range of specified parameter). The results from MSES have been experimentally evaluated for both single and multi-element airfoils showing good agreement with experimental data (Lakshmi et al., 2018). Consequently, it has been implemented in this work to obtain the aerodynamic performance characteristics of multi-element airfoils at different AoA, i.e.

the lift and drag polars. For the single element airfoils, experimentally measured polar data was used.

MSES couples the inviscid Euler formulation and the integral viscous formulation to compute the airfoil characteristics of airfoils at different Reynolds numbers. The fundamental assumption is that the viscous effects are confined to the BL and wake. The inviscid flow is solved using the steady state, two-dimensional Euler equations of

Conservation of mass

$$\oint \rho_{air} \vec{v} \cdot \vec{n} ds = 0 \tag{3.1}$$

Conservation of momentum

$$\oint \left(\rho_{air} \left(\vec{v} \cdot \vec{n} \right) \vec{v} + p\vec{n} \right) ds = 0 \tag{3.2}$$

Conservation of Energy

$$\oint \rho_{air} \vec{v} \cdot \vec{n} h_t ds = 0 \tag{3.3}$$

where $\vec{v}$ is the velocity vector, h_t is the stagnation enthalpy, and $\vec{n}$ is the unit normal vector.

The discrete Euler equations are solved on a grid formed from the intersection of the inviscid flow streamlines and the curves from the airfoil surface points as shown in Figure 3.1. The streamlines are solved using a panel method (potential flow solver) for a user specified AoA, arbitrary selected only used for the initial grid generation. The spacing of the grid nodes on the airfoil surface were left at the default value computed by MSET (grid generation code from MSES). Additionally, MSES documentation shows fairly low sensitivity to the location of the outer boundaries, i.e. the grid size (Drela, 2007b). Consequently, the grid size was also left at the default value. The main assumptions for the solver are a vortex+source+doublet airfoil far-fiend BC and streamwise momentum (streamline entropy is conserved) everywhere except near the leading edge where a isentropic condition is applied.

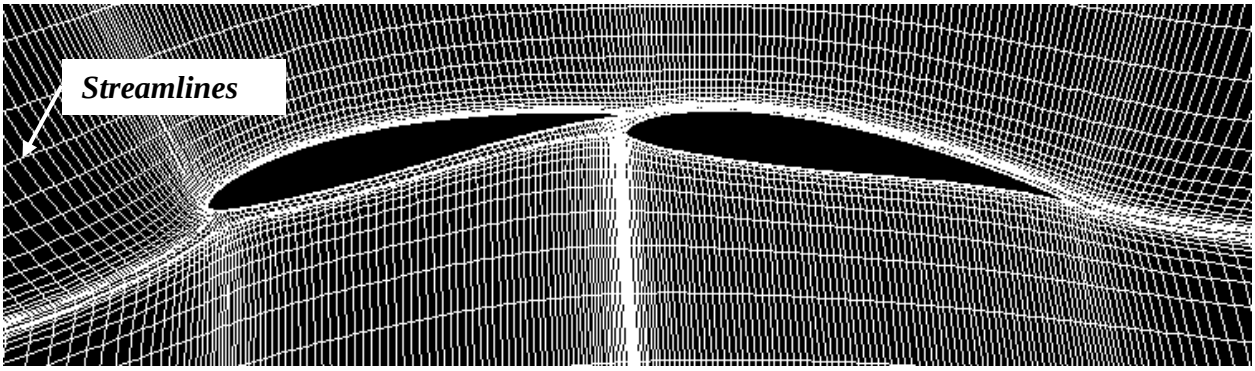

Figure 3.1: MSES grid for an E214 two-element airfoil at an AoA of 5 deg. (see Table 4.1 under E214-T3 for configuration details).

The computation of the airfoil characteristics is carried out using the MSIS flow solver. MSIS is a special case of MSES used for extremely small freestream Mach numbers, $M_\infty = 0.001$ or less. The MSES solver assumes that the only effect of the BL and wake is to displace the inviscid flow away from the physical body to create an effective "displacement body" (Drela, 1986). The displacement body is shown in Figure 3.2. To this end, the inviscid grid is coupled to the viscous flow through the displacement of the streamline adjacent to the airfoil, i.e. BL displacement thickness (δ^*). The BL equations used in the analysis of the viscous flow are derived from the Prandtl integral BL equations. With the assumptions of negligible cross-stream pressure variations and an adiabatic free streams. The final form of the BL equations used in the program are (Terry, 2004)

$$\frac{d\theta}{d\xi} + \left(H + 2 - M_e^2\right)\frac{\theta}{U_e}\frac{dU_e}{d\xi} = \frac{C_f}{2} \tag{3.4}$$

And

$$\theta\frac{dH^*}{d\xi} + \left(2H^{**} + H^*\left(1 - H\right)\right)\frac{\theta}{U_e}\frac{dU_e}{d\xi} = 2C_{Ds} \tag{3.5}$$

where θ is the momentum thickness, C_f is the coefficient of friction, C_{Ds} is the dissipation coefficient, ξ is a local coordinate along the BL, M_e and U_e are the Mach number and velocity component at the edge of the BL, respectively. Additionally, the three shape factors are

$$H = \frac{\delta^*}{\theta}, H^* = \frac{\theta^*}{\theta}, H^{**} = \frac{\delta^{**}}{\theta} \tag{3.6}$$

where δ^{**} is the density thickness, θ^* is the kinetic energy thickness.

Additionally, empirical relations are used for laminar and turbulent closure to Equation (3.4) and Equation (3.5). To predict the onset of transition, the Orr-Sommerfeld equation is used where the critical amplification factor "*n*" for the e^n envelope used is 9. Additionally, transition can also be forced using the MSES code. This allows for the additional capability to analyzing tripped airfoils. MSES can also account for the effect of inflow turbulence by adjusting the "n" factor same as in code Xfoil. The system of coupled inviscid-viscous non-linear equations and constraints are solved using a Newton-Raphson iterative method.

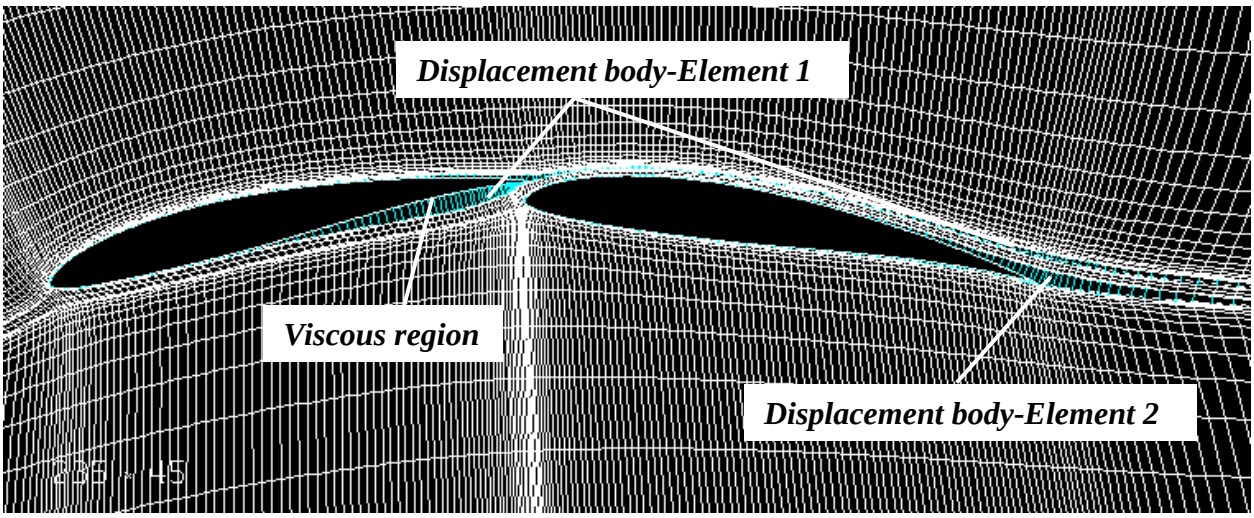

Figure 3.2: MSES inviscid flow streamlines and viscous region for an E214 two-element airfoil at a grid AOA of 5 deg. (see Table 4.1 under E214-T3 for configuration details).

3.2 **Rotor Analysis**

In this thesis, XROTOR is used as the main tool to design and analyze the rotor. XROTOR is an open source code developed by Mark Drela and Harold Youngren at MIT (Drela, 2011). XROTOR is an extension of the classical blade-element/vortex formulation developed by (Betz, 1919), Goldstein (Goldstein, 1929), Theodorson (Theodorsen, 1948) and reformulated by Larrabee (Larrabee and French, 1983). XROTOR was chosen because it has been validated and is extensively used in practice by both academia and industry. XROTOR is an interactive program for the design and analysis of ducted and free tip rotors. The rotor geometry can be analyzed or designed to achieve a minimum induced loss circulation distribution. The induced velocities and induced losses are calculated using one of several available methods based on the user preference. They are: Vortex formulation, Graded momentum formulation, and Potential Formulation. The

last two aforementioned methods treat the rotor blade sections as lifting lines and assume the wake contraction and wake self-deformation are small, i.e. relatively low disk loading (Drela, 2003).

The vortex formulation is used for rotors with non-radial lifting lines (raked or swept blades). The induced velocities on the lifting lines are computed using a discrete vortex wake that trails from the lifting line into the far-field downstream.

The Graded momentum formulation is based on the classical theory of propellers developed by Glauert (Glauert, 1926) and revived by Larrabee (Eugene Larrabee and French, 1983). This approach assumes that the rotor has a low advance ration and relies on the Betz-Prandtl tip loss factor. The main advantage of this method is its extreme computational efficiency.

The third approach is the potential formulation which is more computationally expensive. The potential formulation is extension of Goldstein's solutions which solves the helically-symmetric potential flow about a rigid helicoidal wake. Therefore, it applies to rotor with any blade number and radial load distribution. This approach also treats ducted rotors when computing the induced velocities and induced losses. Noting the need for a rotor analysis tools that accounts for the presence of the duct, the third approach (potential formulation) is used throughout the rotor analysis in this research. The duct here is assumed to be an aerodynamically "long" duct with a uniform inflow velocity.

The rotor analysis is carried by decomposing the blade into 30 radial sections with user specified aerodynamic parameters, i.e. lift and drag polars. The velocity triangle seen by the blade section at some radial position *r* is shown in Figure 3.3. The axial and tangential velocities add to give the relative velocity as

$$W_{rel} = \sqrt{W_a^2 + W_t^2} \quad [m/s] \tag{3.7}$$

where W_a and W_t are the total axial and total tangential velocities, respectively. They are computed as

$$W_a = V + u_a + v_a \quad [m/s] \tag{3.8}$$

$$W_t = \Omega r - u_t - v_t \quad [m/s] \tag{3.9}$$

Where v_t is the induced tangential velocity, v_a is the induced axial velocity, V is the forward velocity, u_a and u_t are externally-induced axial and tangential velocity, respectively.

Though, XROTOR has extensive capabilities and can be used for many applications. However, in this research XROTOR is exclusively to calculate the induced velocities on a rotor-only axial flow fan. Consequently, no externally induced velocities (u_a and u_t) or forward velocity (V) are implemented in the rotor analysis as part of this research, i.e. they are assumed to be zero.

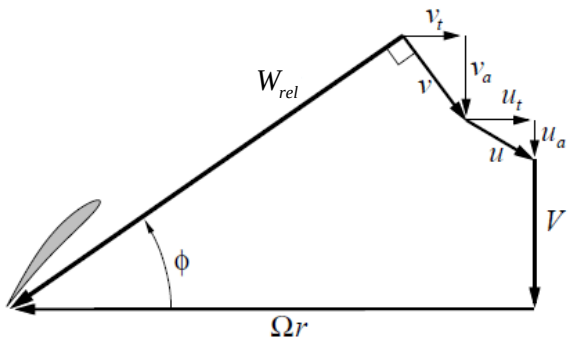

Figure 3.3: Total blade relative velocity decomposition diagram at a radial position r.

XROTOR relates the induced tangential velocity, or "swirl", to the circulation on the blades using Hemlholtz's theorem. Helmholtz's theorem states that the vortex filament is constant along its length. Therefore, the line integral evaluated along the contour of the induced tangential velocity vector ($\vec{v}_t$) is equal to the circulation around the blade. That is

$$\Gamma = \oint \vec{v}_t dL \tag{3.10}$$

Consequently, the total circulation at a radial position (r) is described as $N_B\Gamma(r)$ where $\Gamma(r)$ is the circulation at the radial position r. Here, it is assumed that the wake has a semi-infinite helical shape as shown in Figure 3.4. Therefore, only half of the circulation about the rotor plane is shed as illustrated in Figure 3.4. Half the circulation about a circumferential circuit at a radial position r in the rotor plane is

$$2\pi r\bar{v}_t = \frac{1}{2} N_B \Gamma \tag{3.11}$$

Where the circumferentially-averaged tangential velocity ($\bar{v}_t$) is related to the blade tangential velocity (v_t) as

$$\bar{v}_t = v_t F \sqrt{1+\left(\frac{4\lambda_w R}{\pi N_B r}\right)^2} \tag{3.12}$$

where F is the Prandtl's factor associated with the "tip losses," R is the fan radius [m], and λ_w is the local wake advance ratio. The Prandtl's factor is computed as

$$F_{loss} = \frac{2}{\pi}\arccos\left(e^{-f}\right) \tag{3.13}$$

where:

$$f = \frac{N_B}{2}\left(1-\frac{r}{R}\right)\frac{1}{\lambda_w}$$

$$\lambda_w = \frac{r}{R}\tan\phi = \frac{r}{R}\frac{W_a}{W_t}$$

Assuming that the total induced relative velocity is perpendicular to the total relative velocity, the axial velocity can be computed as

$$v_a = v_t \frac{W_t}{W_a} \tag{3.14}$$

This assumption is true for a lightly-loaded rotors having a Goldstein circulation distribution and a non-contracting helical wake that has the same pitch at all radii.

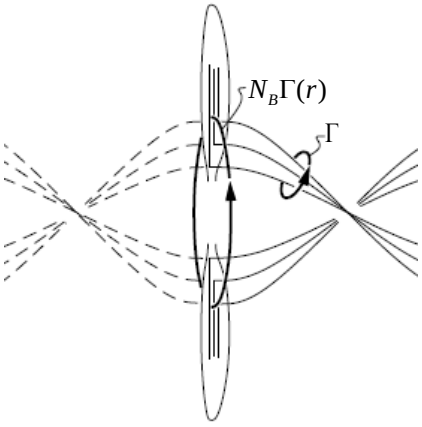

Figure 3.4: Semi-infinite helical wake showing the circulation/swirl relation in XROTOR.

The overall system performance is evaluated using a global Newton method where the Newton residual ($\mathcal{R}$) is the $C_l - \Gamma$ relation. Therefore, the residual is

$$\Re(\Psi) = \Gamma - \frac{1}{2} W_{rel} c C_l(\alpha, \mathrm{Re}, M_{rel}) \tag{3.15}$$

where c is the chord [m], α is the AoA [deg], and C_l is the coefficient of lift. The solution converges when the Newton remedial ($\mathcal{R}$) is approximately zero. The result is the local circulation along the blade ($\Gamma(r)$. The circulation around the airfoil creates a lift force which is perpendicular to the relative velocity (W_{rel}) and a drag force in the direction of the flow as shown in Figure 3.5(a). The lift (L) and drag (D) force for a position *r* along the blade are then described as:

$$dL = \frac{1}{2} N_B \rho_{air} W_{rel}^2 C_l c dr \tag{3.16}$$

$$dD = \frac{1}{2} N_B \rho_{air} W_{rel}^2 C_d c dr \tag{3.17}$$

Where C_d is the Coefficient of drag. The section thrust and torque are the forces in the axial and tangential direction as shown in Figure 3.5(b). They are computed as

$$dT = \frac{1}{2} N_B \rho_{air} W_{rel}^2 \left(C_l \cos(\phi) - C_d \sin(\phi)\right) c dr \tag{3.18}$$

$$dQ = \frac{1}{2} N_B \rho_{air} W_{rel}^2 \left(C_l \sin(\phi) + C_d \cos(\phi)\right) c r dr \tag{3.19}$$

Where ϕ is the flow angle computed as

$$\phi = \arctan\left(\frac{W_a}{W_t}\right) \tag{3.20}$$

Noting that $W_t = W_{rel}\cos\phi$ and $W_a = W_{rel}\sin\phi$ from Figure 3.5(a), the local Thrust (T) and Torque (Q) are expressed as

$$dT = \frac{1}{2} N_B \rho_{air} W_{rel}^2 \left(C_f \cos(\phi) - C_d \sin(\phi)\right) c dr \tag{3.21}$$

$$dQ = \frac{1}{2} N_B \rho_{air} W_{rel}^2 \left(C_l \sin(\phi) + C_d \cos(\phi)\right) c r dr \tag{3.22}$$

The total thrust and torque generated by the rotor are computed by integrating equation (3.16) and equation (3.17) respectively.

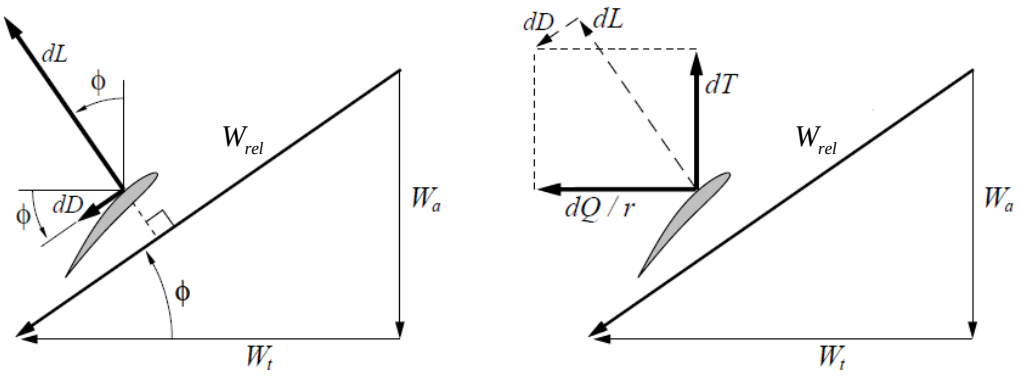

Figure 3.5: Aerodynamic blade section force components resolved into **(a)** lift-drag forces, and **(b)** torque-thrust forces.

The aerodynamic efficiency is described by the ratio of the propulsive power and the shaft power as

$$\eta_{total} = \frac{VT}{\Omega Q} \tag{3.23}$$

Similarly, the local propulsive efficiency can be described as

$$\eta_{local} = \frac{VdT}{\Omega dQ} \tag{3.24}$$

Combining Equations (3.21), (3.22), (3.8) and (3.9) the local aerodynamic efficiency can be computed as

$$\eta_{local}(r) = \frac{V\Omega r}{\Omega r V} \frac{\left(1 - {v_t}/{\Omega r}\right)}{\left(1 + {v_a}/{V}\right)} \tag{3.25}$$

The local aerodynamic efficiency is the product of the inviscid Froude efficiency (η_i) and the viscous profile efficiency (η_p), hence

$$\eta_{local}(r) = \eta_i \eta_p \tag{3.26}$$

The local viscous profile efficiency (η_p) is derived as

$$\eta_p(r) = \frac{\left(1 - \varepsilon \frac{W_a}{W_t}\right)}{\left(1 + \varepsilon \frac{W_t}{W_a}\right)} \tag{3.27}$$

and the inviscid local Froude efficiency is computed as

$$\eta_i(r) = \frac{\left(1 - \frac{v_t}{\Omega r}\right)}{\left(1 + \frac{v_a}{V}\right)} \tag{3.28}$$

Where ε is the drag to lift ratio computed as

$$\varepsilon = \frac{C_d}{C_l} \tag{3.29}$$

The local profile efficiency accounts for the viscous drag on the airfoils through the drag to lift ratio (ε). Therefore, the viscous profile efficiency describes how well the propeller airfoils perform. The inviscid Froude efficiency represents inviscid losses that result from accelerating the rotor.

3.3 Noise Prediction Tools

As discussed before, there are many noise sources in ventilation fans. However, the two dominant ones are the rotor self noise (RSN) due to the airfoil boundary later interacting with the the trailing edge and the turbulence in the inlet BL interacting with the rotor tip section (BLTRIN). The models implemented to predict these noise sources are described in this section. The models predict the power spectral desinsity (PSD) function for the source sound power. The PSD is then used to compute the sound power spectrum in narrowbands and 1/3rd octave bands.

3.3.1 Rotor Self-Noise (RSN)

The approach implemented to predict RSN is to use an empirical expression for the wall-pressure spectrum in conjunction with a model for trailing edge noise. To this end, the edge scattering Howe's model for trailing edge noise at low Mach numbers is implemented (Howe, 1978; Howe, 1998). The model predicts the far-field acoustic pressure PSD, $S_{FF}(\theta, \psi, R, \omega)$, for an observer at (θ, ψ, R) as

$$S_{FF}(\theta,\psi,R,\omega)=\frac{U_c h}{2\pi^2 c_{air} R^2}\ell_s(\omega)Sin^2(\theta)Sin(\psi)S_{pp}(\omega)\left[\frac{N^2}{m^4}s\right] \quad \textbf{(3.30)}$$

where h is the airfoil span, $\ell_s(\omega)$ is the span-wise integral correlation length, ω is the oscillation frequency (rads/s), $S_{pp}(\omega)$ is the PSD of the surface pressure over the airfoil near the trailing edge, and U_c is the convection speed of the turbulence eddies over the airfoil that is less than the relative flow speed over the airfoil, $U_{rel} < U_c$. The relative flow speed U_{rel} is estimated by XROTOR.

In Equation (3.30), it is assumed that the turbulence is on the upper surface of the airfoil and that for large values of the reduced frequency $\omega b/U$, the turbulence flow on the bottom side of the airfoil is uncorrelated to the upper turbulence. The total noise is the incoherently addition of the upper and bottom side of the airfoil. Another assumption is that the noise source is compact, e.g. $\lambda > 2b$ where λ is the acoustic wavelength and $2b$ is the airfoil chord.

The observer position (θ,ψ,R) relative to the trailing edge is illustrated in Figure 3.6.

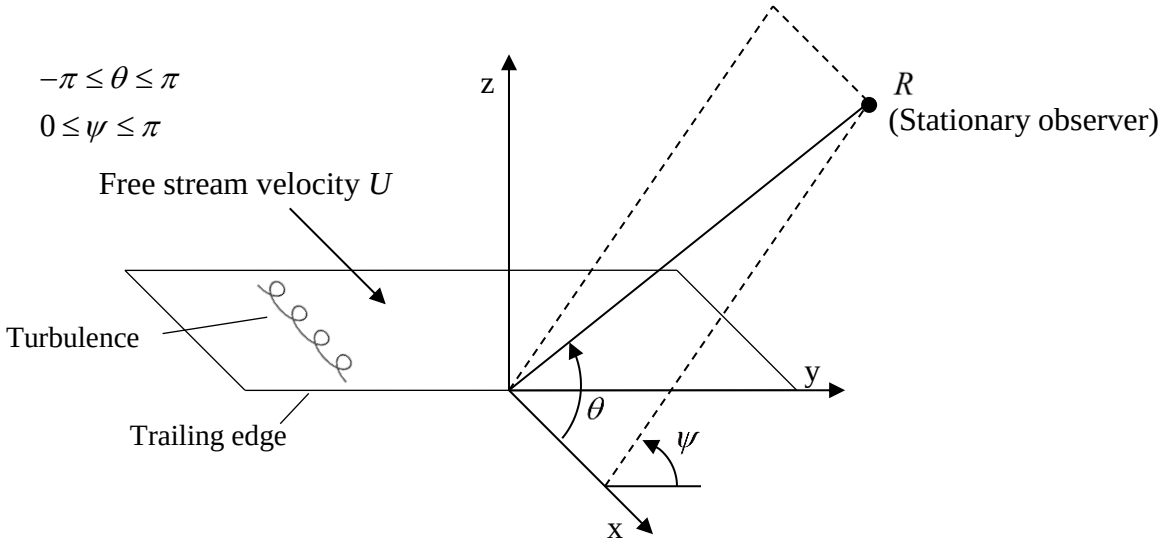

Figure 3.6: Coordinate system relative to trailing edge.

The surface pressure PSD $S_{pp}(\omega)$ in Equation (3.30) needs to be defined. There are many empirical equations for the surface pressure with increasing degree of complexity (Mugridge,

1973; Amiet, 1976; Howe 1998; Rozenberg et al., 2012; Lee and Shum, 2019). In this work, we consider the model proposed by Amiet (1976). It is given by

$$S_{pp}(\omega)=\left(\frac{\rho_{air}}{2}U_{rel}^2\right)^2\left(\frac{\delta^*}{U_{rel}}\right)\frac{2\times10^{-5}}{\left[1+\left(\frac{\omega\delta^*}{U_c}\right)+0.217\left(\frac{\omega\delta^*}{U_c}\right)^2+0.00562\left(\frac{\omega\delta^*}{U_c}\right)^4\right]}\quad\left[\frac{N^2}{m^4}s\right] \tag{3.31}$$

In the above expression for the surface pressure, it is assumed that $S_{pp}(\omega)$ is single-sided. That is

$$p_{rms}^2=\int_0^\infty S_{pp}(\omega)\,d\omega$$

Since we are mainly interested in the sound power level, the pressure in Equation (3.30) is used to estimate intensity and integrate over a sphere with radius *R* to get acoustic power. That is

$$S_{WW}(\omega)=\int_{\theta=-\pi}^{\theta=\pi}\int_{\psi=0}^{\psi=\pi}\frac{S_{FF}(\theta,\psi,R,\omega)}{\rho_{air}c_{air}}R^2d\theta d\psi\quad\left[\frac{Nm}{s}s\right] \tag{3.32}$$

Replacing Equation (3.30) into Equation (3.32) and solving for the integrals

$$\int_{\theta=-\pi}^{\theta=\pi}Sin^2(\theta)\,d\theta=\pi\ \text{ and }\int_{\psi=0}^{\psi=\pi}Sin(\psi)\,d\psi=2$$

yields

$$S_{WW}(\omega)=\frac{U_c h}{2\pi\rho_{air}c_{air}^2}\ell_s(\omega)S_{pp}(\omega)\quad\left[\frac{Nm}{s}s\right] \tag{3.33}$$

Several parameters need to be assumed to implement Equation (3.33). The BL displacement thickness at the trailing edge is estimated in terms of the drag coefficient C_d, valid for both upper and lower surfaces, as

$$\delta^*\cong 2bC_d\qquad[m] \tag{3.34}$$

The drag coefficient is also obtained from XROTOR and accounts for the fan solidity.

The span-wise correlation length and the convention turbulence velocity are assumed as

$$\ell_s(\omega)\approx\frac{2U_{rel}}{\omega}\qquad[m]\ U_c\approx 0.8U_{rel} \tag{3.35}$$

Replacing the above expression, multiplying by number of blades (noise from blade are uncorrelated), and Amiet's surface pressure spectrum in Equation (3.31), Equation (3.33) results in

$$S_{WW}(\omega) = \frac{0.8}{2\pi} \frac{M_{rel}^5 \rho_{air} c_{air}^3 N_B (ch) C_d}{\omega} F(\omega) \tag{3.36}$$

where

$$F(\omega) = \frac{2\times10^{-5}}{\left[1+\left(\frac{\omega\delta^*}{U_c}\right)+0.217\left(\frac{\omega\delta^*}{U_c}\right)^2+0.00562\left(\frac{\omega\delta^*}{U_c}\right)^4\right]}$$

The expression in Equation (3.36)(3.33) needs to be multiplied by 2 to account for the BL contribution from both surfaces. In general, the results should also be multiplied by 2 to account for the two sided PSD. However, the surface pressure spectrum in Equation (3.31) is already single sided and thus it is not needed.

Finally, it is important to note that the RSN source is predicted using the flow velocity profile without accounting for the presence of the BL. This introduces errors in the RSN predictions. The blade angle of attack in the outer section of the blade, affected by the BL, increases while the relative flow velocity will decrease. These effects can have an important effect on the predicted noise spectrum and they are not considered here.

3.3.2 Turbulence Rotor Interaction Noise (TRIN)

For this noise source, only the prediction of the inlet outer wall turbulence interacting with the rotor tip is considered. The inner BL interacting with the rotor hub section was assumed to be significantly lower in level and not modelled. The flow field in the duct and BL is computed using the code DFDC.

The noise prediction approach implemented is the method developed by Mugridge and Morfey (Mugridge and Morfey, 1972; Mugridge 1973, Morfey, 1974) in conjunction with the turbulence upwash spectrum assuming a Von Karman isotropic turbulence model (Hinze, 1959). Consistent with the RSN models, the formulation predicts the sound power. The approach starts with the

expression of the sound power PSD due to incident turbulence interacting with a rotor blade. That is

$$S_{WW}(\omega) = \frac{\omega^2}{12\pi\rho_{air}c_{air}^3}\left[S_{LL}(\omega)h\ell_s(\omega)\right] \ [watts \times s] \tag{3.37}$$

The airfoil unsteady lift loading, $S_{LL}(\omega)$, is due to the incident turbulence interacting with the blade. Mugridge proposed the following expression for the unsteady blade lift spectrum

$$S_{LL}(\omega) = \left(2\pi\rho_{air}bU_{rel}\right)^2 K_L(\omega)S_{ww}(\omega) \left[\frac{N^2}{m^2}s\right] \tag{3.38}$$

where $S_{ww}(\omega)$ is the velocity upwash turbulence spectrum (*w* is the transversal turbulence in the BL) entering the blade row and $K_L(\omega)$ is a three-dimensional lift response factor computed by Mugridge (1971).

The lift spectrum (similar to the Sears Function) is given by Mugridge as

$$K_L(\omega) = \frac{1}{\left(1+2\pi k_1\right)}\left[1-\frac{\left(1-e^{-2H_L}\right)}{2H_L}\right] \tag{3.39}$$

where

$$H_L = \frac{h}{2b}\sqrt{\left(k_1^2+\frac{2}{\pi^2}\right)} \quad k_1 > 2 \tag{3.40}$$

is a span-wise correlation factor accounting for span-wise coherent of incident turbulence and k_1 is the reduced frequency, $k_1 = \omega b/U_c$. For large blade aspect ratio (*h*>>*2b*) Equation (3.39) is approximated as

$$K_L(\omega) = \frac{1}{\left(1+2\pi k_1\right)} \tag{3.41}$$

For isotropic turbulence, explicit expressions for the transversal turbulence, *w*, characterized in terms of the stream-wise turbulence strength (u_{rms}) and integral length scale (λ_f) are available. Gliege (2002) proposed to use the upwash spectrum derived by Mani (1971) with additional simplifications. He derived the following upwash spectral function

$$S_{ww}(\omega) = \left(\frac{\lambda_f u_{rms}^2}{2\pi U_c}\right) \frac{1+3\left(\lambda_f \frac{\omega}{U_c}\right)^2}{\left(1+\left(\lambda_f \frac{\omega}{U_c}\right)^2\right)^2} \tag{3.42}$$

It is interesting to note that this expression corresponds to the isotropic turbulence model developed by Liepmann.

However, the other well-known model of isotropic turbulence is by Von Karman (Hinze, 1959; Amiet, 1975). Using the Von Karman model, Amiet (1975) derived the upwash PSD as

$$S_{ww}(\omega) = \frac{\lambda_f u_{rms}^2}{6\pi U_c} \frac{3+8\left(\frac{\Gamma_f(1/3)}{\sqrt{\pi}\Gamma_f(5/6)}\lambda_f \frac{\omega}{U_c}\right)^2}{\left(1+\left(\frac{\Gamma_f(1/3)}{\sqrt{\pi}\Gamma_f(5/6)}\lambda_f \frac{\omega}{U_c}\right)^2\right)^{11/6}} \tag{3.43}$$

where Γ_f is the Gamma function.

To write the Von Karman model in the form of the Liepmann expression in Equation (3.43), the term $\Gamma(1/3)/\sqrt{\pi}\Gamma(5/6) = 1.3393$ is inserted in Equation (3.43) and after rearranging leads to

$$S_{ww}(\omega) = \left(\frac{\lambda_f u_{rms}^2}{2\pi U_c}\right) \frac{1+\frac{8}{3}\left(1.3393\lambda_f \frac{\omega}{U_c}\right)^2}{\left(1+\left(1.3393\lambda_f \frac{\omega}{U_c}\right)^2\right)^{11/6}} \tag{3.44}$$

Comparing Equation (3.42) to Equation (3.44) the two models have very similar functional definition. However, it was decided to use the Von Karman model from Equation (3.44).

Replacing (3.38) into (3.37) and multiplying by the number of rotor blades (noise from blades assumed uncorrelated) gives

$$S_{WW}(\omega)=\frac{N_B\pi\rho_{air}c_{air}}{6}\left(\frac{\omega^2b^2}{U_c^2}\right)\frac{U_c^2}{U_{rel}^2}M_{rel}^4(2bh)\frac{\ell_s(\omega)}{b}K_L(\omega)S_{ww}(\omega)\quad[watts\times s] \tag{3.45}$$

This expression shows that the turbulence rotor interaction scales with the 4th power of the relative Mach number, $M_{rel}=U_{rel}/c$. However, there are other terms that are indirectly a function of the relative Mach number. Assuming the convective velocity (U_c) and span-wise correlation length (ℓ_s) as

$$\ell_s(\omega)\approx\frac{2U_{rel}}{\omega}\quad U_c\approx 0.8U_{rel} \tag{3.46}$$

The sound power spectral density implemented is

$$S_{WW}(\omega)=\frac{N_B\pi\rho_{air}c_{air}}{6}\left(\frac{\omega^2b^2}{U_c^2}\right)0.8^2M_{rel}^4(2bh)\frac{2U_{rel}}{\omega b}K_L(\omega)S_{ww}(\omega) \tag{3.47}$$

with $K_L(\omega)$ computed using Equation (3.41) and $S_{ww}(\omega)$ computed with Equation (3.44).

The final step in the implementation is to model the turbulent BL and estimate the BL thickness, mean velocity profile, stream-wise turbulence intensity, and integral length scale. In a BL, the mean and fluctuating velocities vary from the distance to the wall. The turbulent BL consists of two layer, inner and outer. The mean velocity profile in both the inner and outer regions for a <u>smooth</u> flat surface with zero pressure gradient is given as (Cebeci and Smith, 1974; Coles, 1956; Joseph and Parry, 2001)

$$\begin{aligned}\frac{U(r_w)}{U_\tau}&=\frac{1}{0.41}Ln\frac{r_w}{\delta}+5+2\frac{1.75}{0.41}\sin^2\left(\frac{\pi r_w}{2\delta}\right)\\ \frac{U(R_w)}{U_\tau}&=\underbrace{\frac{1}{0.41}Ln(R_w)}_{\text{Inner}}+\underbrace{5+2\frac{1.75}{0.41}\sin^2\left(R_w\frac{\pi}{2}\right)}_{\text{Outer}}\end{aligned} \tag{3.48}$$

where $r_w = R_{tip} - r$ is the distance from the wall, $R_w = r_w/\delta$ is the normalized distance to the wall, δ is the BL thickness, and U_τ is the friction velocity. The friction velocity is a normalizing factor that accounts for the wall shear stress. It is given as

$$U_\tau = U_\infty \sqrt{C_f/2} \tag{3.49}$$

where C_f is the skin friction coefficient on the wall and U_∞ is the mean velocity in the free stream.

A similar expression exits for the mean flow velocity profile for a rough (not aerodynamically smooth) surface based on the height of the roughness elements (Cebeci and Smith, 1974).

From the experimental data in this work, it was found that Equation (3.48) doesn't predict the BL mean velocity well. This is likely because the flow in the small fans tested here behave more like a pipe, e.g. BL thickness is ~ 10% of the duct radius. However, the 1/7 power velocity distribution for the BL mean velocity (White, 1991) matches the experimental data very well and it was used to predict the mean velocity profile. It is gives as

$$\frac{U(r_w)}{U_\infty} = \left(\frac{r_w}{\delta}\right)^{1/7} \tag{3.50}$$

The BL thickness, δ, needed in Equation (3.50) is obtained from the BL displacement thickness, $\Delta = \delta/\delta^*$, where Δ is in the 4.8 to 6.4 range for pipe flows and ~ 3.9 for airfoils (Rozenberg et al., 2012). Here, it was assumed $\Delta = 4$. The BL displacement thickness and U_∞ are estimated from DFDC.

The three component of turbulence intensities for a BL over a smooth flat plate without a pressure gradient were measured by Klebanoff (1954) and reproduced in Figure 3.7.

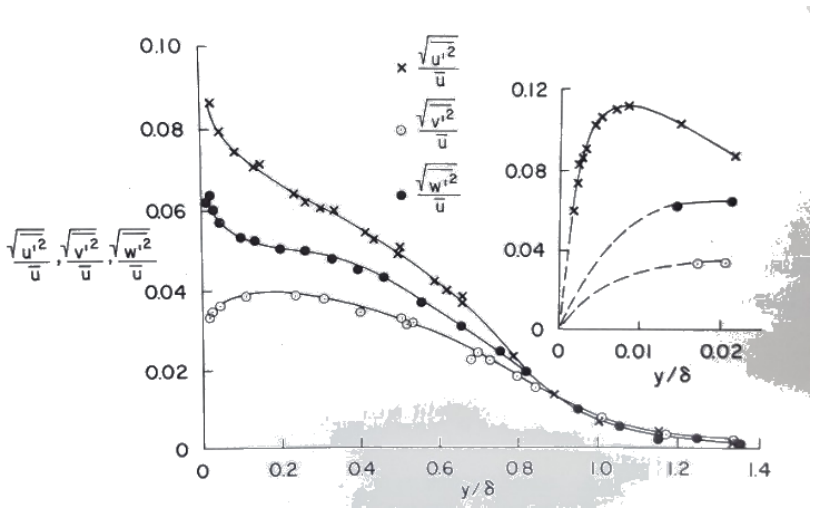

Figure 3.7: BL turbulence intensities as a function of the distance to the wall normalized by BL thickness for a smooth flat plate and zero pressure gradient. Data from Klebanoff, 1954 where *u* stream-wise, *w* transversal, and *v* radial components.

The approach here was to use a polynomial curve fit of the stream-wise turbulence intensity. The expression is

$$\frac{u_{rms}^2(R_w)}{U_\infty^2} = 0.0075 - 0.0305R_w + 0.098R_w^2 - 0.1738R_w^3 + 0.138R_w^4 - 0.0392R_w^5 \qquad \textbf{(3.51)}$$

The last parameter needed for the BL turbulence characterization is the integral length scale (macro-scale), λ_f. This parameter is a measure of the largest eddy size in the turbulent fluid and it is calculated using the turbulence energy spectrum $E(f, r_w)$ evaluated at *f*=0 as

$$\lambda_f(r_w) = \left.\frac{E(f, r_w)U(r_w)}{4u_{rms}^2(r_w)}\right|_{f=0} \qquad \textbf{(3.52)}$$

Ganz et al. (1998) made measurements of the BL for the 18" fan tested at several fan speeds. The turbulence length scales in the stream-wise, transverse and radial directions are presented in Figure 3.8. The turbulence integral scale and distance to the wall are normalized by the BL thickness. The results for normalized distances $r_w/\delta > 1$ (outside the BL) should be ignored due to noise in the measured data. The results for $r_w/\delta < 1$ shows significant differences in the length scales. The measured data was also compared to previous measurements for a flat plate BL (solid dots). The

measured integral scales are to some extent larger that the measure data in the fan but it follows the same trends.

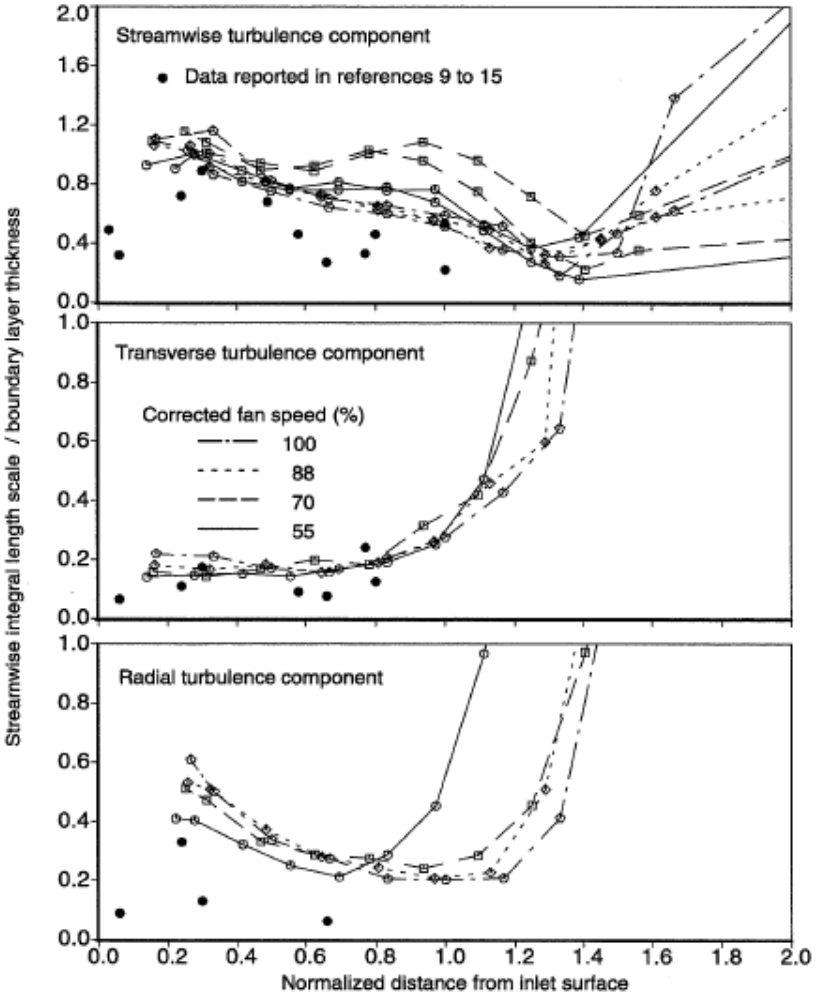

Figure 3.8: Normalized integral length scales of inlet BL (Ganz et al., 1998).

Here the stream-wise turbulence integral scale was estimated by curve fitting the data from a flat plate in Figure 3.8. The expression for the curve fitted data is

$$\frac{\lambda_f\left(R_w\right)}{\delta} = \left(7.3216R_w^3 - 12.877R_w^2 + 5.9577R_w\right) \tag{3.53}$$

3.3.3 Computation of Total Sound Power Spectrum

The acoustic power PSD in Equation (3.36) for RSN and Equation (3.47) for BLTRIN needs to be converted to sound power level spectrum in 1/3rd octave and/or narrow bands for comparison to

the measured data. To this end, the acoustic power PSD is integrated between the band's limits. This integral can be simplified by assuming the spectral density to be constant in the band. Thus,

$$W(\omega_c) = \int_{\omega_\ell}^{\omega_u} S_{WW}(\omega)\, d\omega \approx S_{WW}(\omega_c)(\omega_u - \omega_\ell) = S_{WW}(\omega_c)\Delta\omega \qquad \textbf{(3.54)}$$

where f_c , f_u, and f_ℓ are the band center , upper, and lower frequencies in Hz, respectively.

For the case of 1/3rd octave bands $\Delta\omega = 0.231556 \times \omega_c$. Thus, Equation (3.54) reduces to

$$W(f_c) = \int_{2\pi f_\ell}^{2\pi f_u} S_{WW}(\omega) 2\pi df = S_{WW}(2\pi f_c) 2\pi (f_u - f_\ell) = S_{WW}(2\pi f_c) 2\pi f_c 0.231 \qquad \textbf{(3.55)}$$

For the case of narrowband, using the spectral resolution Δf desired Equation (3.55) reduces to

$$W(f_s) = S_{WW}(2\pi f_s) 2\pi\Delta f \qquad \textbf{(3.56)}$$

where f_s are the frequency vector of the spectrum.

The RSN and BLTRIN are then added incoherently to obtain the total noise spectrum. This assumption is a reasonable first order approximation since the RSN is affected by the turbulence in the inlet duct BL. It is well known that inflow turbulence will result in an increase in the airfoil drag coefficient due to the development of a thicker BL, especially at high angles of attack. This effects is directly related to the turbulence intensity in the duct wall BL and it is not accounted for in the RSN model.

3.4 **Aerodynamics of Duct Geometry**

The duct geometry is designed and analyzed using the open source code Ducted Fan Design Code (DFDC) developed my Mark Drela and Harold Youngren (Drela, 2005). DFDC combines a lifting line representation of the rotor with an axisymmetric panel representation of the duct and hub to compute the self-induced velocities form the fan, duct, and center body. The formulation used in DFDC in part derives from XROTOR which combines the classical blade-element/vortex formulation with simple models to account for the hub and duct.

DFDC uses the panel method (potential flow solver) solution for the velocity distribution and free stream mach number to model the effect of the duct wall BL. The hybrid BL analysis consists of

a two equation momentum/energy method to model the laminar BL and Green's lag entrainment formulation to model the turbulent BL. The momentum and kinetic energy equations for the compressible axisymmetric flow are derived by Drela (Drela, 2014) as

Momentum equation

$$\frac{d\theta}{d\xi}+\left(H+2-M_e^2\right)\frac{\theta}{U_e}\frac{dU_e}{d\xi}=\frac{C_f}{2}-\frac{\theta}{b_n}\frac{dr}{d\xi} \tag{3.57}$$

Kinetic energy equation

$$\theta\frac{dH^*}{d\xi}+\left(2H^{**}+H^*\left(1-H\right)\right)\frac{\theta}{U_e}\frac{dU_e}{d\xi}=2C_{Ds} \tag{3.58}$$

Where b_n is the lateral width parameter. Equation 3.57 and 3.58 are essentially the same 2D integral equations used in MSES (Equations (3.4) and (3.5)) except for the lateral divergence term involving $dr/d\xi$ implemented to account for the axisymmetric flow.

Transition is modeled using the Orr-Sommerfeld equation. Transition from a laminar to a turbulent BL is assumed to occur when the integrated amplitude has grown by more than a factor of e^9 (~8100). The empirical assumption is the weakest link as it can vary between 7-11 depending on the free stream turbulence, surface roughness and background noise level (Drela, 2014). The turbulent BL is modeled by numerical integration of Green's lag entrainment equations (Green et al., 1973)

Momentum equation

$$\frac{d}{d\xi}\left(r\theta\right)=\frac{rC_f}{2}-\left(H+2-M_e^2\right)\frac{r\theta}{U_e}\frac{dU_e}{d\xi} \tag{3.59}$$

Shape factor equation

$$\frac{\theta d\bar{H}}{d\xi}=\frac{d\bar{H}}{dH_1}\left[C_E-H_1\left\{\frac{C_f}{2}-\left(H+1\right)\frac{\theta}{U_e}\frac{dU_e}{d\xi}\right\}\right] \tag{3.60}$$

Entrainment equation

$$\frac{\theta dC_E}{d\xi} = F\left[\begin{array}{l} \dfrac{2.8}{H+H_1}\left\{(C_\tau)_{EQ_0}^{1/2} - \lambda_d C_\tau^{1/2}\right\} + \left(\dfrac{\theta}{U_e}\dfrac{dU_e}{d\xi}\right)_{EQ} - \\ \dfrac{\theta}{U_e}\dfrac{dU_e}{d\xi}\left\{1+0.075M^2\dfrac{\left(1+0.2M_e^2\right)}{\left(1+0.1M_e^2\right)}\right\} \end{array}\right] \quad \textbf{(3.61)}$$

Where C_E is the entrainment coefficient, C_τ is the shear stress coefficient, and λ_d is the scaling factor on the dissipation length. The shape parameters are defined as:

$$H = \frac{\delta^*}{\theta}, \quad \bar{H} = \frac{1}{\theta}\int_0^\infty \left(1-\frac{U}{U_e}\right)d\eta, \quad H_1 = \frac{\delta - \delta^{**}}{\theta} \quad \textbf{(3.62)}$$

The equations are solved on a parametric grid where ξ is constant along each quasi-radial line and η is constant along each streamline as shown in Figure 3.9. The BL ODE's are integrated using a variable step size second order Runge-Kutta scheme. The main assumptions of this method are: Adiabatic wall conditions, Prandtl number of unity, and Isentropic flow. Viscosity is evaluated by Sutherland's law. Empirical relations are implemented for closure of the laminar and turbulent BL ODE's resulting in the output BL analysis variables θ, H, C_f, δ^*, and U_e.

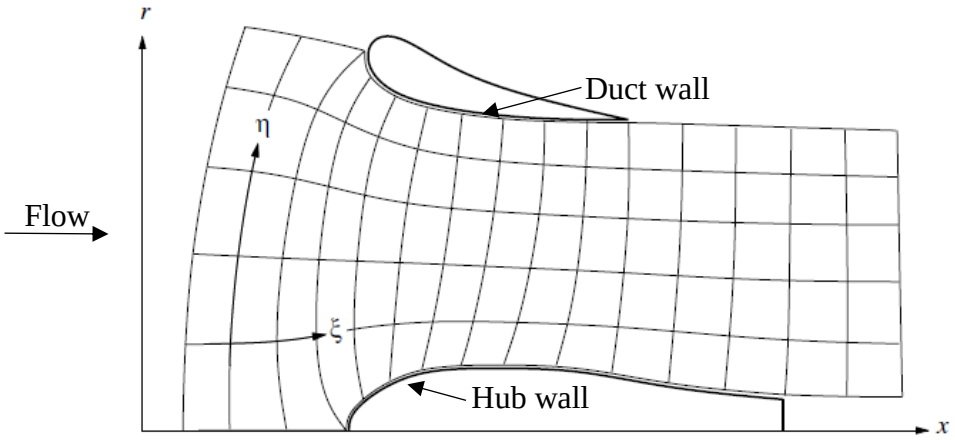

Figure 3.9: Grid and grid parameters defined parametrically as $\xi(x,r)$ and $\eta(x,r)$, taken from Drela (2005).

CHAPTER 4

4 Fan Design

The review of fan design methods in section 2.4 suggests that a comprehensive design approach is needed to fill in the gaps that still persist in the literature. Particularly, considering both the aerodynamic performance and the acoustic signature of low speed fans. To this end, a design methodology was formulated and implemented to design rotor only low pressure ducted axial ventilation fans for minimum noise. The proposed design approach is innovative because it is comprehensive, well though-out, and easy to implement. The design approach has been implemented using the open source codes XROTOR and DFDC described in Chapter 3. These codes are used because they provide accurate and computationally efficient results that can model key effects including induced velocities, blade solidity, and BL properties in the duct. The comprehensive design method is presented in Section 4.1. For the sake of clarity in the presentation, the design approach is presented in the form of a case study. The single input here is the volumetric flow rate of 1000 CFM in conjunction with a compact design.

The case study in Section 4.1 is limited to traditional single element airfoils. The design of fan blades employing multi-element airfoils in presented in Section 4.2. Contrariwise to single element airfoils, experimental data for multi-element airfoil configurations at low Reynolds numbers is non-existent. Consequently, section 4.2 also presents the numerical design of the multi-element airfoil configuration. The multi-element airfoil blade design presented here represents a "proof of concept" design. A comparison between fans designed with multi-element blade and single element blades is also presented in section 4.2. All of the fans are designed using the control vortex methodology. Hence, the fans will be referred to as ***CVS*** (Control-vortex single) for the single element airfoil and ***CVT*** (Control-vortex Tandem) for the multi-element airfoil.

4.1 Proposed Fan Design Approach

The fan design is implemented in a stepwise approach consisting of 4 stages as follows:

1. Selecting the airfoil that will result in the highest profile efficiency.
2. Implementing a multi-objective genetic algorithm to determine the fan size (hub and tip radius), the fan speed, and the span wise axial and swirl velocities that maintain radial equilibrium. This optimization is constrained by using the minimum fan tip speed with maximum possible fan efficiency. Also, the genetic approach provides a family of solutions for the designed to choose from.
3. Inverse design of the blade chord and twist distributions that result in the optimized axial and swirl velocities from the previous step.
4. Design of the fan duct to maximize flow rate and minimize BL thickness.

Although noise is not directly used in the design approach, noise is indirectly accounted for by minimizing the fan tip speed, drag losses, and the duct BL thickness. This approach is justified by considering that the fan noise scales directly with the drag losses and to the 4-6th power of the fan speed, i.e. reducing the speed by half can potentially reduce noise levels significantly. Another reason not to include noise as a metric in the design is that noise prediction tools, in particular for broadband component, lack sufficient accuracy and in some cases require inputs rarely available at the design stage, e.g. turbulence data. Moreover, currently there are no noise prediction tools for multi-element airfoils.

The four design stages are now presented in sub-sections 4.1.1 through 4.1.4.

4.1.1 Airfoil Selection

The fan blade airfoil sections are one of the most important component of axial fans as it determines the maximum attainable aerodynamic efficiency. The design of the airfoil blade sections is not normally carried out by fan designers. Instead, these are selected from open literature based on a high lift to drag ratio. Airfoils have been extensively researched and optimized in the last century, particularly for large scale conventional aircraft. This has resulted in a substantial amount of airfoil geometries and corresponding aerodynamic characteristics in the open

literature. However, these airfoils have been primarily designed to operate at chord Reynolds numbers over 1,000,000. Consequently, these airfoils may not be applicable to the low Reynolds numbers for industrial fans, estimated to be in the range of 40,000 to 400,000 (Eck, 1973), e.g. three orders of magnitude lower than the operating Reynolds numbers for modern airplanes. Figure 4.1 shows the variations of the maximum sectional lift-to-drag ratio with the Reynolds number. It is illustrated here that conventional smooth airfoils designed to operate at high Reynolds numbers ($>10^6$) perform best. However, a significant drop in performance at low Reynolds numbers ($10^5 < Re < 10^6$) is observed. Consequently, the high lift airfoils optimized for aircraft are not suitable airfoils to use for the design of low speed fans. Therefore, airfoils must be designed to operate in low Reynolds numbers.

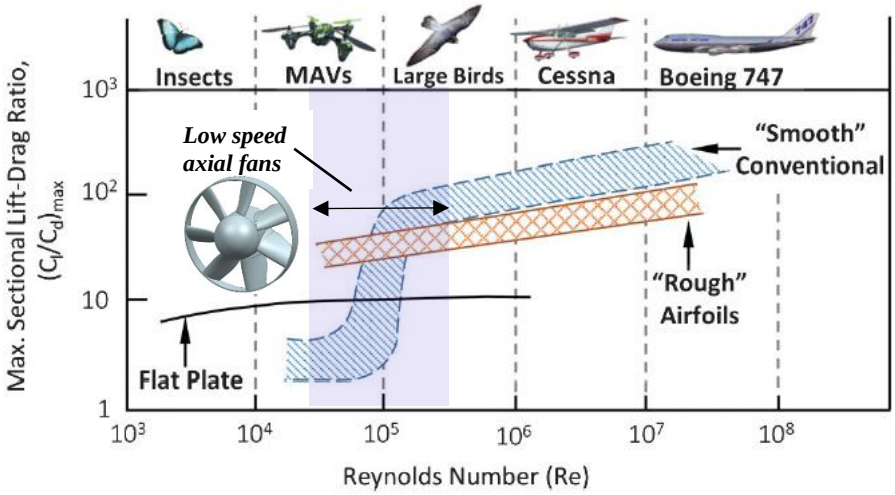

Figure 4.1: Effect of Reynolds number on the airfoil maximum lift-drag ratio, taken from Winslow et al (2018).

Experimental airfoil characteristics for low Reynolds number airfoils is relatively extensive in the open literature thanks to the work of Selig et al. (Selig et al., 1989a; Selig et al., 1989b; Williamson et al., 2012). To this end, this data was reviewed and several airfoils candidates selected based on a high lift to drag ratio at low Reynolds numbers ($Re<10^5$). Figure 4.2 plots the lift to drag ratio as a function of the Reynolds number for the airfoils selected. Figure 4.2 shows that the Clark-y airfoil has a high lift to drag ratio at a Reynolds number of 500,000. However, its performance deteriorates at low Reynolds numbers and it was also excluded from further consideration. Although some airfoils like the FX 63-137 and E423 airfoils have favorable airfoil characteristics at low Reynolds numbers, these type of airfoils were excluded due to a very complex geometry that is difficult to fabricate. To this end, the second criteria for selecting the airfoils was a geometry

feasible for fabrication, in particular using 3D printing technology. Thus, the airfoils considered as part of this research are the E214, SD5060, DF101, SD8020, and SD8000.

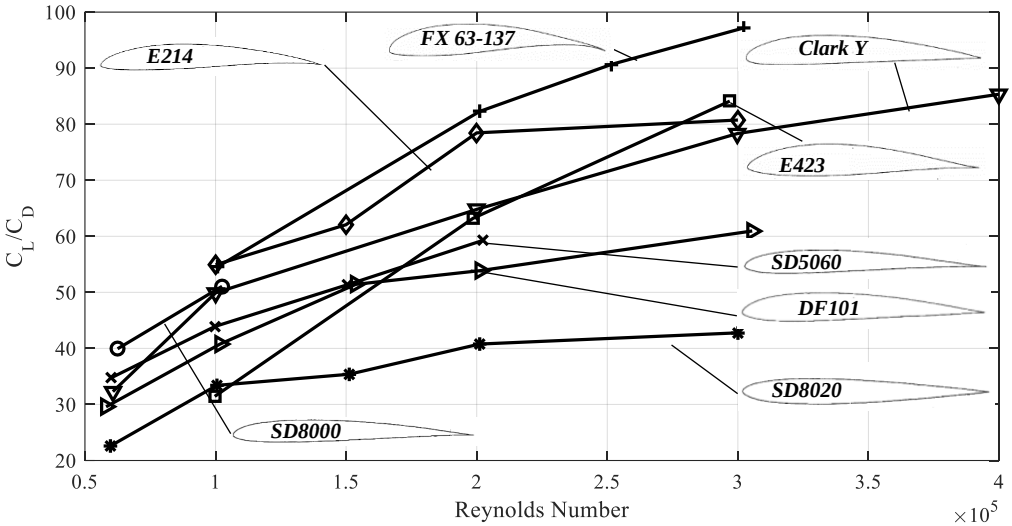

Figure 4.2: Effect of Reynolds number on the maximum lift-Drag ratio of low speed airfoils, experimental data retrieved from Selig et al. (1989).

The performance and efficiency of axial fans is affected not only by the airfoil geometry but also by the air velocity past the blades. To this end, the airfoil efficiency is also investigated for different velocity flow fields, i.e. axial and tangential velocities. The aerodynamic efficiency (η) is the product of the ideal efficiency (η_i) and is the viscous profile efficiency (η_p) as shown in Equation (3.26). The ideal efficiency describes the maximum theoretical efficiency in an inviscid fluid and accounts for the kinetic energy losses. Conversely, the viscous profile efficiency accounts for the viscous profile drag losses of the airfoil (Drela and Youngren, 2003). Due to the viscous features of the flow at low Reynolds number, the focus here is on the viscous profile efficiency only, hereafter referred as simply the airfoil profile efficiency. Assuming that the tangential velocity is larger than the induced tangential velocity, $V_t >> v_t$, Equation (3.27) becomes

$$\eta_p = \frac{\left(1 - \frac{C_d}{C_l}\frac{v_a}{V_t}\right)}{\left(1 + \frac{C_d}{C_l}\frac{V_t}{v_a}\right)} \tag{4.1}$$

where V_t is the tangential velocity [m/s]. To account for the presence of other airfoils, the airfoil efficiency is computed assuming a cascade with the velocity vectors shown in Figure 4.3. Here the solidity due to adjacent airfoils in the airfoil cascade is

$$s = c/d \tag{4.2}$$

where c is the airfoil chord, and d is the distance between succeeding airfoils. The analysis is carried out at a Reference Reynolds number of 60000 assuming the flow is incompressible and steady. Consequently, the unsteady flow effects due to the relative motion between consecutive blades are not accounted for.

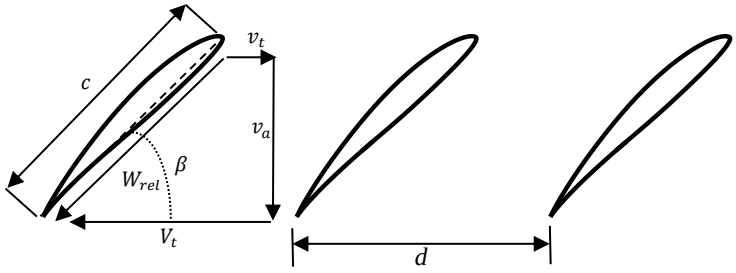

Figure 4.3: Airfoil vectors for numerical analysis of the airfoil cascade.

The maximum profile efficiency (η_p) is computed for a given flow field (v_a and V_t) by optimizing the chord (c) and twist (β) that results in the highest lift to drag ratio (C_l/C_d). To this end, the profile efficiency for an E214 airfoil was computed for a range of tangential velocities between 0 and 0.2 Mach and different axial velocities as shown in Figure 4.4. As illustrated, the efficiency increases as the tangential velocities increases up to a maximum and then roll off with constant slope. Additionally, it can be observed from Figure 4.4 that as the axial velocity increases so does tangential velocity required to maintain high aerodynamic efficiency. Figure 4.4 shows that the airfoil stalls by the sharp roll-off of the profile efficiency at a very low tangential velocity.

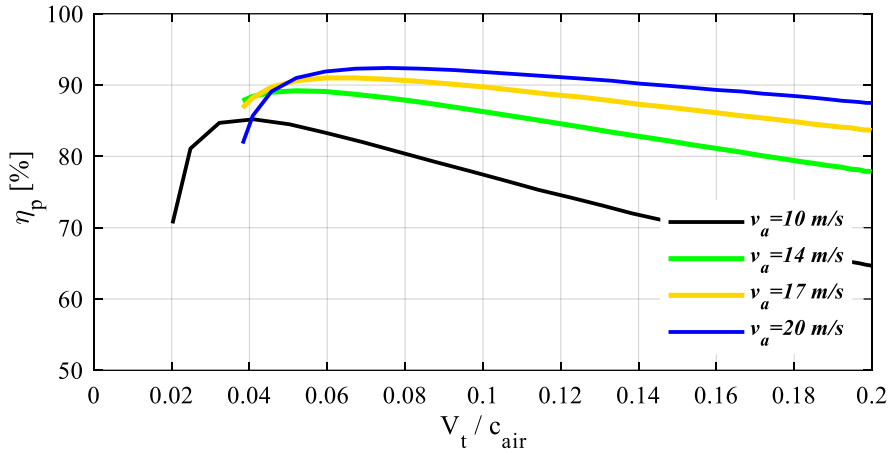

Figure 4.4: Profile efficiency as a function of the tangential velocity for various axial velocities on an E214 airfoil geometry.

Next, the profile efficiency is plotted against the ratio of tangential to axial velocities in Figure 4.5. As illustrated here, all of the profile efficiency tend to collapse into one curve. Therefore, it is evident that there is a velocity triangle that results in the optimum flow angle and highest efficiency. The corresponding velocity ratio (V_t / v_a) concurs with the highest lift to drag ratio. It is also illustrated in Figure 4.5 that as the V_t / v_a ratio increases, the flow angle decreases which subsequently results in a decrease in the AoA. Hence, the roll-off at low V_t / v_a ratios is due to stall as already indicated. As the V_t / v_a ratio is increased, the airfoil operates at lower lift than the lift for the maximum lift to drag ratio.

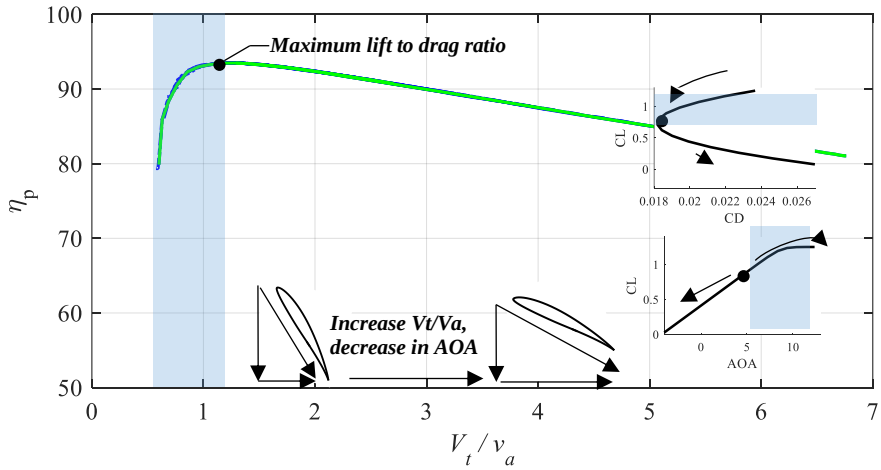

Figure 4.5: Collapsed profile efficiency curves as a function of the Vt/Va ratio for the E214 airfoil.

As previously mentioned, a widely used practice in the design of ventilation fans is to design for the highest lift to drag ratio. However, as illustrated in Figure 4.5 it is possible to operate at lower lift to drag ratios while still maintaining a high aerodynamic efficiency. Therefore, it is possible to design fans at lower angular velocities, i.e. V_t / v_a ratios, to reduce noise while still maintaining a high aerodynamic efficiency.

This process can be repeated for different airfoils as shown in Figure 4.6. As it can be observed from this figure, the profile efficiency varies for different airfoils. Consequently, the normalized profile efficiency curves can be used to directly compare the performance of different airfoils. From this figure, the E214-PT airfoil is the best performing airfoil which is the airfoil with the highest lift to drag ratio. Furthermore, it is also illustrated in Figure 4.6 that regardless of the airfoil geometry, the minimum V_t/v_a ratio occurs at 0.6 for all airfoils. Therefore, the minimum tangential velocity for the design of the blade sections is

$$V_t > 0.6 \times v_a \tag{4.3}$$

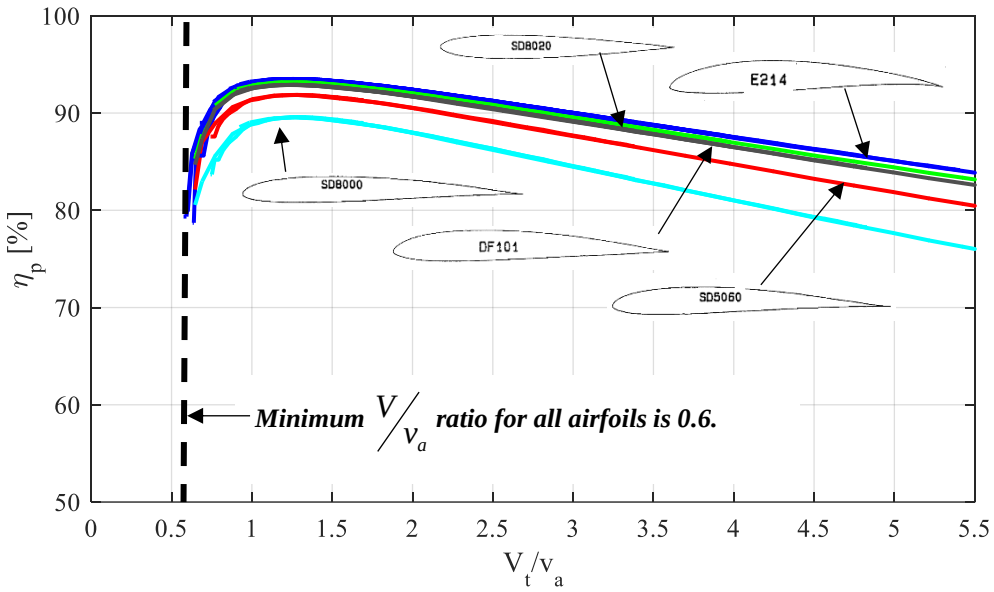

Figure 4.6: Collapsed profile efficiency curves for the E124 (blue), SD8020 (cyan), SD8000 (green), DF101(red) and SD060 (dark grey) airfoils.

4.1.2 Optimum Fan Dimensions and Velocity Profile Design

The second stage is used to determine the fan dimensions, the velocity profile without the need to know the actual blade geometry, and the fan speed. The fan volumetric flow rate ($\dot{V}$) is the integral of the axial velocity profile $v_a(r)$ from the hub to the tip. That is

$$\dot{V} = \int_{r_h}^{R} 2\pi r v_a(r) dr \tag{4.4}$$

Therefore, the design of the velocity profile to generate a target volumetric flow rate involves the following design variables: (1) hub-to-tip ratio, (b) fan diameter, and (c) axial velocity distribution. The selection of these parameters is traditionally based on trial and error methods based on guidelines in the open literature. However, the guidelines vary widely based on the source. For instance, Wallis (1983) recommends a hub-to-tip ratio between 0.4 and 0.7 for well-designed fans However, Osborne (1966) describes efficient fans having a hub to tip ratio less than 0.55. Additionally, fan diameter is also determined based on the empirical Cordier diagram which has been shown to have a very wide range of possible efficient designs.

The axial velocity distribution is often set by a free vortex blade loading. The only known approach for the selection of the non-free vortex velocity distribution is one presented by Castegnaro (2017). This approach uses a Cordier diagram for non-free vortex fans to select the appropriate swirl velocity distribution, i.e. free vortex, forced vortex, etc.

In this work, a multi-objective Genetic Algorithm (GA) was implemented to optimally determine fan dimensions and axial flow profile. The GA (Chipperfield and Fleming, 1995) algorithm searches the design space for the design variables that will minimize the fan tip speed ($M_{tip} = \Omega R / c_{air}$) while generating the target volumetric flow rate ($\dot{V}$). The design axial velocity profile must be selected such that radial equilibrium is maintained along the blades. Consequently, the centrifugal force must be balanced by the radial pressure gradient on the fluid element. If there is no radial equilibrium, there will be a radially outward flow that will increases the tip losses and tip stalling with a potential increase in noise (Vad and Horvath, 2008). Figure 4.7 illustrate forces on a fluid element. Summation of forces in the radial direction gives

$$(p+dp)(r+dr)d\varphi - pdrd\varphi - 2(p+\tfrac{1}{2}dp)dr\sin(\frac{d\varphi}{2}) - m v_\theta^2 / r = 0 \quad \textbf{(4.5)}$$

Here all of the streamlines are assumed to be concentric about the axis of rotation. Ignoring higher order terms, this leads to the simple radial equilibrium equation (Equation (2.6)) first derived and experimentally validated by Kahane (1947) for the design of non-free vortex fans.

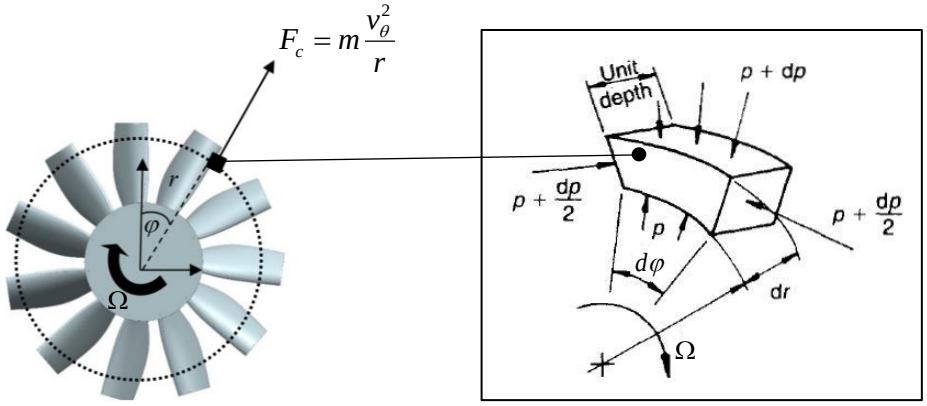

Figure 4.7: Radial forces acting on the rotating fan fluid elements. Radial outward flow results from imbalnce of the centrifugal force (F_c) and radial pressure forces.

The simple radial equilibrium equation (Equation (2.6)) can be expressed using the total pressure ($p_t = p + \tfrac{1}{2}\rho_{air}(v_a^2 + v_\theta^2)$ as:

$$\frac{1}{\rho_{air}}\frac{dp_t(r)}{dr} = v_a(r)\frac{dv_a(r)}{dr} + \frac{v_\theta(r)}{r}\frac{d(rv_\theta(r))}{dr} \quad \textbf{(4.6)}$$

Equation (4.6) is solved for the axial velocity profile ($v_a(r)$) by assuming the swirl velocity has the power law distribution expressed as

$$v_\theta = ar^n \quad \textbf{(4.7)}$$

where a is the swirl velocity coefficient and n is the swirl velocity exponent. The swirl velocity exponent describes the distribution of swirl velocity along the blade, while the swirl velocity coefficient determines the magnitude. Then, using Euler's work equation ($w = \Omega(v_{\theta r}r - v_{\theta r_h}r_h)$) the corresponding axial velocity profile to maintain radial equilibrium is derived by Bruneau as (Bruneau, 1994)

$$v_a(r) = \sqrt{2\Omega a\left(r^{n+1} - r_h^{n+1}\right) - a^2(n+1)\frac{r^{2n} - r_h^{2n}}{n} + v_a^2(r_h)} \quad \textbf{(4.8)}$$

where

$$R(r) = \ln\left(r / r_h\right)^2 \quad for \quad n = 0 \tag{4.9}$$

and

$$R(r) = \ln\left(\frac{r^{2n} - r_h^{2n}}{n}\right) \quad for \quad n \neq 0 \tag{4.10}$$

One main issue with Equation (4.8) is that the velocity at the hub ($v_a(r_h)$) must be assumed. However, in this research the axial velocity at the hub is set such that the velocity ratio at the hub must be $V_t / v_a > 0.6$ as determine from the airfoil analysis in Section 4.1.1. Consequently, the velocity at the hub is conservatively defined as

$$v_a(r_h) = \frac{\Omega r_h}{0.7} \tag{4.11}$$

Therefore, Equation (4.8) becomes,

$$v_a(r) = \sqrt{2\Omega a\left(r^{n+1} - r_h^{n+1}\right) - a^2\left(n+1\right)\frac{r^{2n} - r_h^{2n}}{n} + \left(\frac{\Omega r_h}{0.7}\right)^2} \tag{4.12}$$

The axial and swirl velocity equations to maintain radial equilibrium are therefore expressed by Equations (4.12) and (4.7), respectively. However, the velocity distributing is not defined until the parameters for a and n are specified. There is an infinite number of possible velocity distributions depending on the selected values for a and n. The most common swirl velocity distributions used in industry are: Free Vortex ($v_\theta = ar^{-1}$), Constant Swirl ($v_\theta = ar^0$), and Forced vortex ($v_\theta = ar^1$) (Cory, 2005). Figure 4.8 shows the swirl velocity distributions and corresponding axial velocities. As illustrated here, the free vortex design leads to very high swirl velocities near the hub that will result in a large chord and twist. As described by Wallis (1983), this is the most practical design and thus widely used. The constant swirl velocity leads to an axial velocity distribution that increases from the hub to the tip and a constant swirl velocity distribution. This typically results in a constant chord and low twist distribution along the blades similar to designs by Ruden (1944). Lastly, the forced vortex leads to axial and swirl velocity that increases from the hub to the tip. Consequently, the resulting blades are characterized by a small chord at the hub that increases along the blades span. Forced vortex designs achieve high efficiencies at low pressure coefficients.

However, the reduction of fan efficiency with tip clearance is significantly higher for the forced vortex designs (Castegnaro et al., 2017). Therefore, due to the high efficiency characteristics of the free and constant swirl designs, the present approach focuses on velocity distributions employing a swirl velocity exponent between -1 and 0, i.e. between a free vortex and constant swirl. This range of swirl velocity distribiutions are herein referred to as a control vortex design. To this end, the GA algorithm implements a control vortex design approach to find the axial and tangential flow distributions (find *a* and *n*), fan angular velocity, hub-to-tip ratio, and fan diameter to generate a target volumetric flow rate.

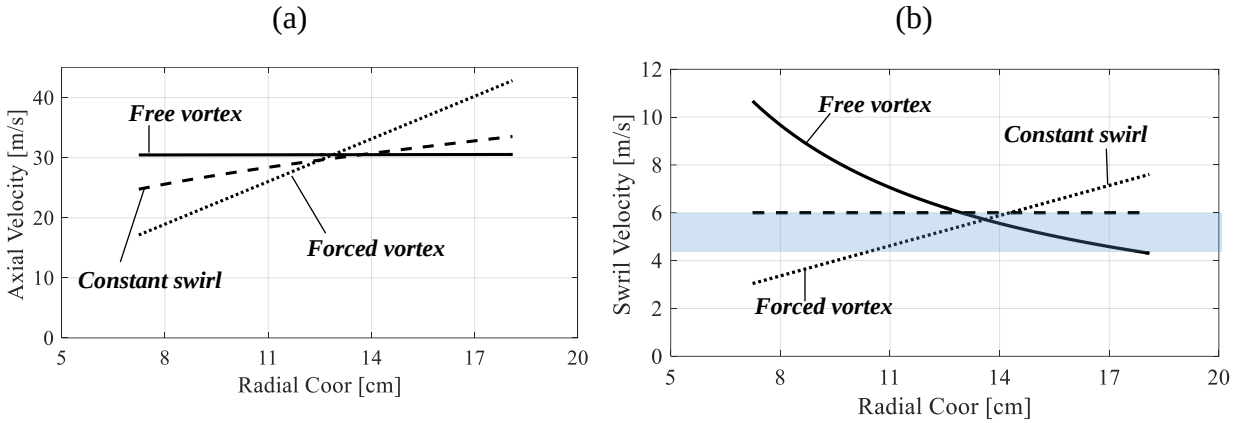

Figure 4.8: Common industry designed **(a)** axial, and **(b)** swirl velocity profiles resulting in radial equilibrium.

The GA algorithm searches the design space to find the combination of input variables (D, υ, and Ω) that minimize the tip speed (M_{tip}) and satisfy the volumetric flow rate requirement. The process begins by setting a set of individuals (initial population) that are characterized by a combination of the design variables. Therefore, a range of values must be specified for each variable. The fitness of each individual (combination of design variables) is evaluated against other individuals with only individuals with a high fitness (individuals close to the minimum tip speed) surviving to the following iteration (generation). The individuals must also satisfy the volumetric flow rate design constraint. To this end, the maximum volumetric flow rate for each individual must be computed. The optimizer finds axial and swirl velocity profiles that will result in the highest volumetric flow rate for the set of design variables (individual). To this end, the swirl and axial velocity profiles are computed using Equations (4.7) and (4.12) respectively for a range of swirl velocity exponents (*n*) between -1 and 0. If the maximum volumetric flow rate is greater than the design flow rate, the set of design variables (individual) are a feasible solution. This process

was repeated for 150 generations. The results are plotted in Figure 4.9 using a Pareto front. The Pareto front describes a set of non-dominating solutions. Therefore, for each hub-to-tip ratio shown in Figure 4.9 the corresponding tip speed (M_{tip}) is the minimum possible, i.e. where $V_t / v_a(r_h) \approx 0.7$. Therefore, the fan designer must prioritize between tip speed and hub-to-tip ratio. The hub-to-tip ratio and corresponding tip speed selected for the design of case study are 0.405 and 0.1, respectively.

The fan tip speed (M_{tip}) is used to compute the fan diameter using Equation (2.3). This is accomplished by matching the fan angular velocity (Ω) to the design angular velocity of the BLDC motor and computing the dimeter (D) corresponding to the design fan tip speed (M_{tip}). This is justified considering that the fan noise is proportional to the fan tip speed (M_{tip}), hence there is no tradeoff between the angular velocity and the diameter of the fan. For the motor selected, the design speed is 3500 RPM, i.e. 366 rad/sec. Then, the diameter is defined to match the designed tip speed. For the case study, the diameter is 0.186 m. The resulting axial and swirl velocities are shown in Figure 4.10.

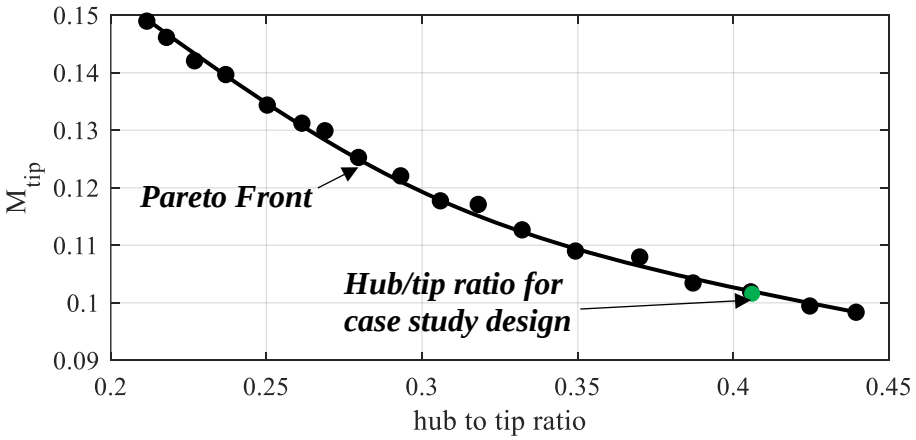

Figure 4.9: Multi-objective GA Pareto front representing the minimum tip speed for the design volumetric flow rate and the best possible compromise with the hub-to-tip ratio.

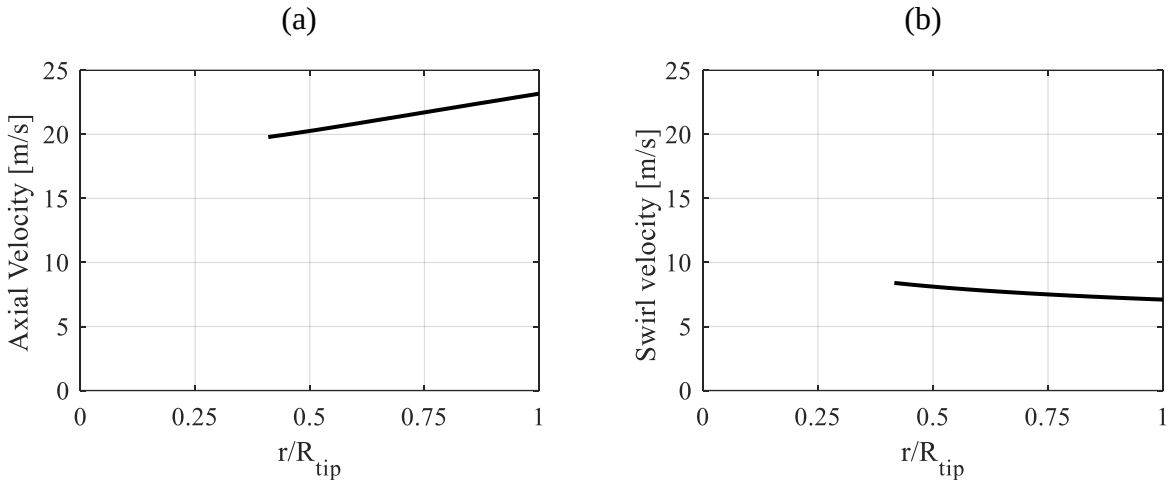

Figure 4.10: Design (a) axial and (b) swirl velocity profiles optimized to minimize the fan tip speed for the design volumetric flow rate of 1000 CFM.

4.1.3 Blade Geometry

In this stage of the process, the number of blades and the blade geometry are defined, e.g. radial chord and twist distributions. To this end, an inverse design approach is implemented to determine the blade geometry that results in the axial and swirl velocity distribution from the previous stage, i.e. velocity profiles in Figure 4.10. The design problem involves decomposing the blade into independent sections with known velocity vectors and prescribed airfoil polars. Figure 4.11 shows the known velocity vectors and blade airfoil, i.e. E214 airfoil selected in section 4.1.1. The solver XROTOR is then used to compute the blade chord and twist that will result in the known velocity vectors at the highest efficiency. As an example, the ideal design of a blade section is where the airfoil operates at the AoA corresponding the maximum lift to drag ratio. This process is repeated for all radial sections to compute the blade chord and twist distribution along the blade span.

It is important to note that for a very low M_{tip} value, it can lead to a very large chord distribution that are geometrically possible but not very practicable. Therefore, it is required to address the feasibility to fabricate an efficient blade. Therefore, three methods for reducing the chord size are possible. They are:

I. increase the number of blades
II. increase the operational tip speed, and
III. select an airfoil geometry with a higher performance, e.g. multi-element airfoil.

The latter is investigated in Section 4.2. Iterations over the first two resulted in a decision to increase the tip speed of the CVS fan to 0.115 and implement a 7 bladed fan. The resulting chord and twist distribution are shown in Figure 4.12 for the CVS fan.

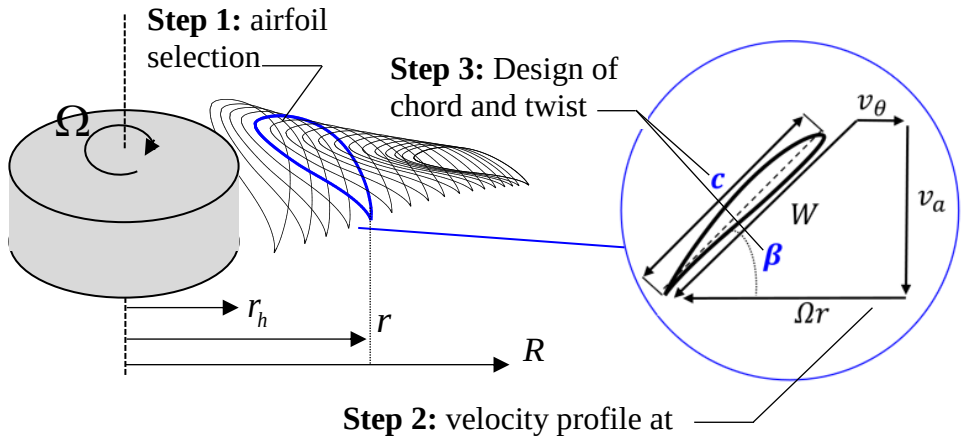

Figure 4.11: Summary of the design process consisting of (1) airfoil selection, (2) Velocity profile design, and (3) inverse design of the blade geometry that will result in the design velocity vectors with the selected airfoil aerodynamic characteristics.

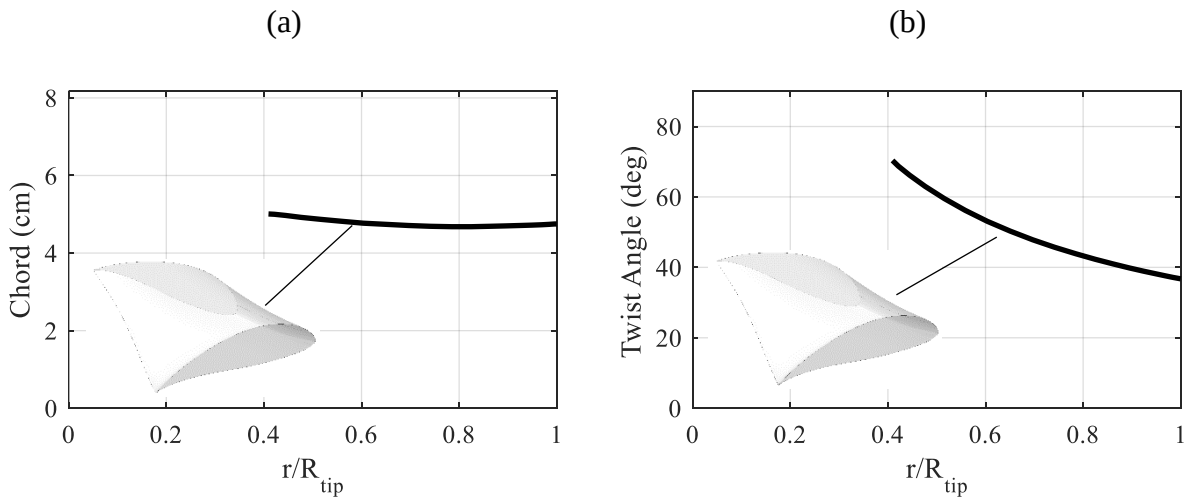

Figure 4.12: (a) chord and **(b)** twist distribution consisting of 5 blades which results in the design velocity profiles with the selected airfoil aerodynamic characteristics.

Figure 4.13 shows the blades integrated into a fan. Particularly, a circular fan hub is added to provide smooth flow to the blade root sections and an outer ring is added to the blade tips to increase its structural strength and to eliminate the tip clearance gap. Longhouse (Longhouse, 1978) demonstrated this to be an effective method for reducing tip gap noise. Tokushige et al.

(2011) demonstrated a decrease of overall noise levels of the ring fan by 3dB relative to a traditional propeller fan.

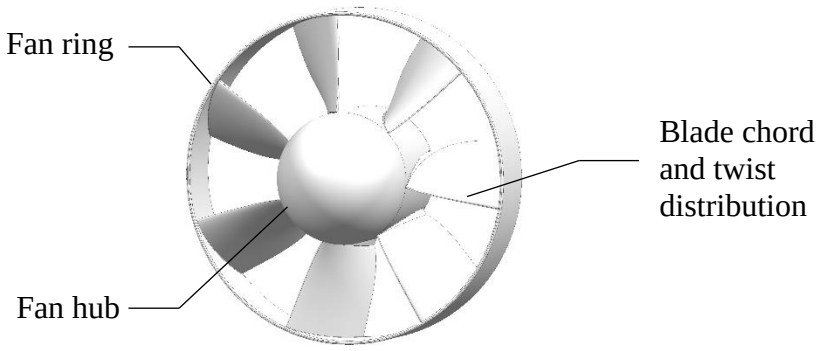

Figure 4.13: Fan blade geometry consisting of the designed blades and added fan hub and ring.

4.1.4 Duct Design

In this last stage, the duct is designed. The use of inlet ducts in low speed axial fans is common given that it helps increase the aerodynamic efficiency and the mechanical strength of the unit (Jang et al., 2001; Longhouse, 1978; Magne et al., 2015; Magne et al., 2012; Piellard et al.; Shimada et al., 2003). Therefore, the inlet duct is an important component that has a direct impact on the performance of axial fans. There are different types of inlets that are frequently used as illustrated in Figure 4.14. Each inlet has different flow characteristics. However, losses are minimized when the curvature of the inflow streamlines is at minimum (Wallis, 1983).

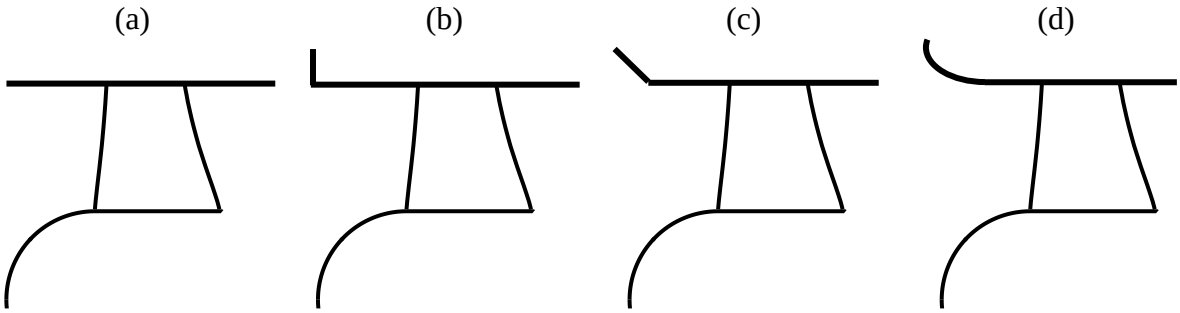

Figure 4.14: Axial fan duct commonly used inlets: **(a)** sharp-edge, **(b)** short flange, **(c)** conical, and **(d)** bellmouth.

The design of inlet ducts expands to any application requiring a fluid to be ingested with minimum losses. That includes compressors, blowers, pumps, jet engines, etc. Consequently, the performance of different inlet geometries is vast. However, the effect of the different geometric parameters on the performance of axial ventilation fans is limited in the open literature. This can

be attributed to the widely accepted understanding that a bellmouth shape will result in lower losses relative to other inlet types (Blair and Cahoon, 2006; Padhy, 1994). The smooth convergent shape of the bellmouth can be accomplished with several methods. Some include airfoil profile shapes (Szafran et al., 2014; Yilmaz et al., 2013), three-circles (Tiwari et al., 2016), and a simple radius. However, the elliptical profile is the best geometry since it results in minimum losses, it is easy to fabricate and it is cost effective (Blair and Cahoon, 2006; Tiwari et al., 2016). To this end, the present section investigates the design of an elliptically shaped inlet duct for rotor-only axial fans. The design parameters for the bellmouth inlet are the vertical ellipse axis (a_1), the horizontal ellipse axis (a_2), and the ellipse angle (Θ). Additionally, the length of the exhaust duct (L_x) is also investigated. Here, the center body is assumed to have a circular shape (radius equal to the hub radius).

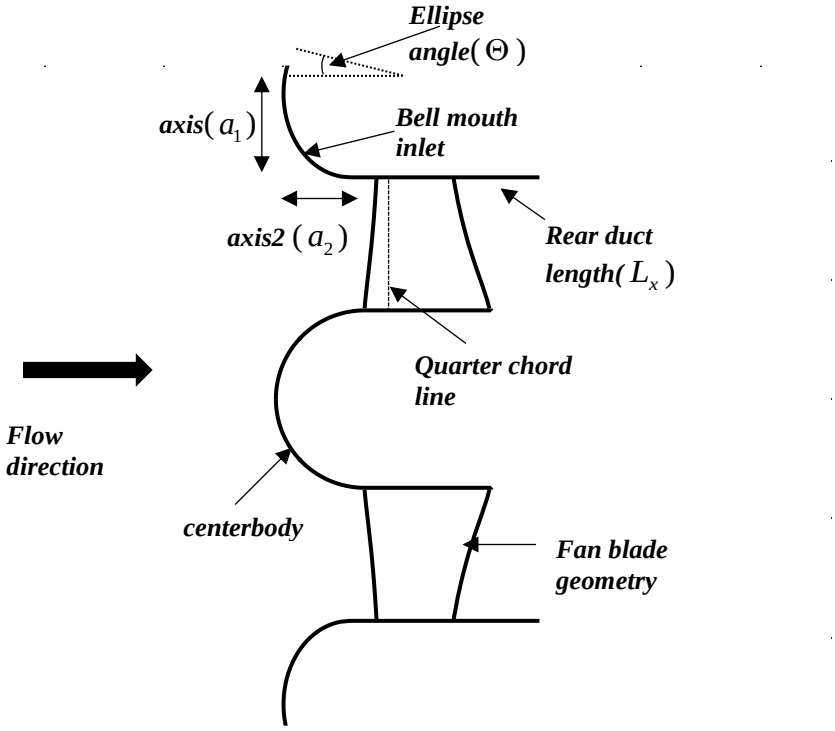

Figure 4.15: Elliptically shaped inlet duct design geometric parameters.

The tapered channel of the bellmouth gradually converges the flow towards the fan inlet. This results in the generation of a BL that can directly impact the aerodynamic performance and the noise radiated by the fan. In general, a thin BL is desirable. Therefore, the metrics of interest for the design of the duct are the inlet BL thickness (δ) and the total volumetric flow. To this end, the open source code Ducted Fan Design Code (DFDC) developed my Mark Drela and Harold Youngren (Drela, 2005) was used for the analysis of the duct geometry and to estimate the BL

thickness. DFDC was selected due to its rapid analysis capabilities and accuracy (Jung et al., 2015; Sargent and Anemaat, 2018). DFDC is a two dimensional code that combines a lifting line representation of the rotor with an axisymmetric panel representation of the duct and hub to compute the self-induced velocities form the fan, duct, and center body. To this end, duct geometry in DFDC is adjusted to an inviscid profile that has the same mass flow near the body as the real viscous profile. This is done using the integral BL equations given by Prandtl. The difference between the real and the inviscid profile is the local BL displacement thickness (δ^*). This is about 1/2 to 1/3 as large as the overall BL thickness (Drela, 1989). In this research, the BL thickness is, therefore, assumed to be approximately 3 times the displacement thickness, i.e. $\delta \sim 3\delta^*$. Although it is an approximate value, it has been shown to agree well with experimental results in Chapter 5. To this end, the velocity profile predicted by DFDC is adjusted to account for the BL. The BL profile was estimated assuming that the flow through the duct has similar characteristics as the flow through a smooth pipe. Therefore, the 1/7th power law empirical equation for the velocity profile is implemented (Schlichting and Gersten, 2016)

$$u(y) = \left(\frac{r_w}{\delta} \right)^{1/7} U_{edg} \tag{4.13}$$

where U_{edg} is the edge velocity and δ is the BL thickness ($\delta = 3\delta^*$ with δ^* estimated by DFDC). For the sake of illustration, Figure 4.16 shows the velocity profile predicted by DFDC and the predicted BL velocity profile at the blades quarter chord using Equation (4.13).

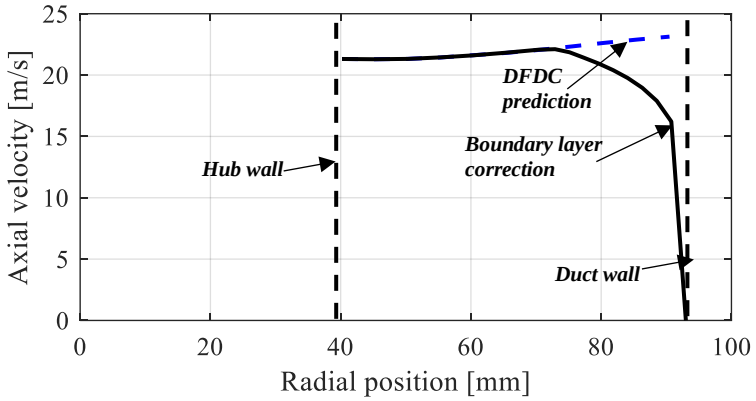

Figure 4.16: Designed axial velocity profile predicted by DFDC and the corrected velocity profile incorporating the BL profile at the blade quarter chord.

Inlet ducts increase the size of the fan unit. Due to work space restrictions, compactness of the design is a desirable attribute (Laboratory, 1989). Therefore, the objectives of the duct design are

to minimize the BL thickness, minimize the size of the inlet duct, and increase the volumetric flow rate. To this end, a dynamic programming methodology has been implemented using DFDC (Puterman, 2014). Illustrative results of the optimization process are presented in Figure 4.17 through Figure 4.20.

Figure 4.17 shows the volumetric flow rate increase for a range of ellipse angles **(** Θ **)** and height to length ratios (a_1 / a_2). As illustrated here the volumetric flow rate increase is not very sensitive to the ellipse angle **(** Θ **)** when it is greater than 0 degrees and independent of the a_1 / a_2 ratio. When the bellmouth inlet is less than a quarter of an ellipse, the performance decreases considerably.

Figure 4.18 shows the BL thickness at the blades quarter chord location (illustrated in Figure 4.15) normalized by duct diameter as a function of the ellipse angles **(** Θ **)** and (a_1 / a_2) ratios. A thin BL is achieved for ellipse angles > 15º again independent of the a_1 / a_2 ratio.

Figure 4.19 shows the BL thickness as a function of the ellipse arc length to diameter ratio (S/D). Thus, this figure assesses the impact of the size of the bellmouth. As shown, the BL thickness reduces as the arc length is increased for all a_1 / a_2 ratios. Thus, results in Figure 49 and 50 indicate that for a thin BL a large bellmoth with a minimum ellipse angle of 15º is needed.

Finally, Figure 4.20 shows the volumetric flow rate increase as a function of the ratio of the length of the rear duct to the diameter. In this simulations, the rear duct is assumed of constant radius. It is illustrated here that the performance of the fan is not very sensitive to the length of the rear duct.

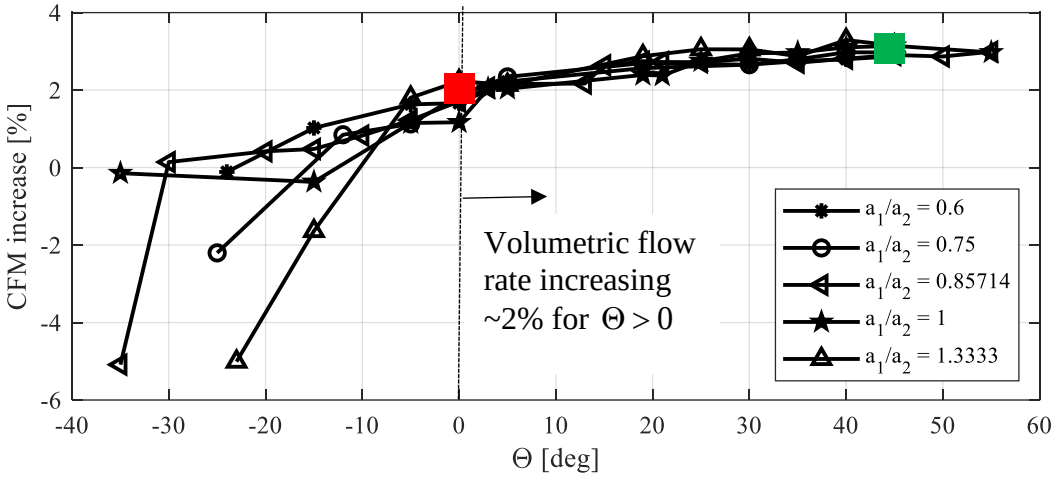

Figure 4.17: Volumetric flow rate increase as a function of the ellipse angle (Θ) and height to length ratio (a_1 / a_2). Red and green squares indicate C and Q-Bellmouth inlet designs.

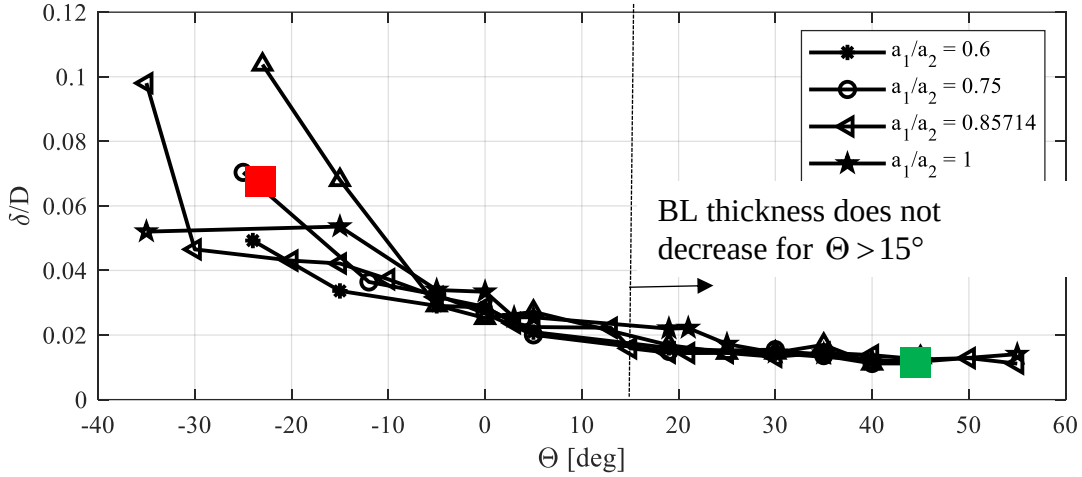

Figure 4.18: BL thickness (estimated by DFDC) as a function of the ellipse angle (Θ) and height to length ratio (a_1 / a_2). Red and green squares indicate C and Q-Bellmouth inlet designs.

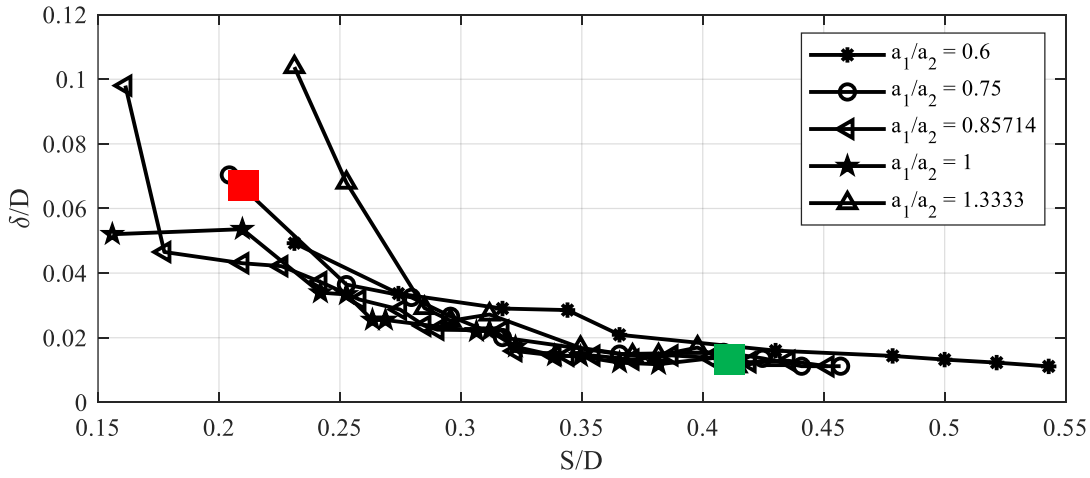

Figure 4.19: BL thickness at the blade quarter chord as a function of arc length for a range of height to length ratios (a_1 / a_2). Red and green squares indicate C and Q-Bellmouth inlet designs.

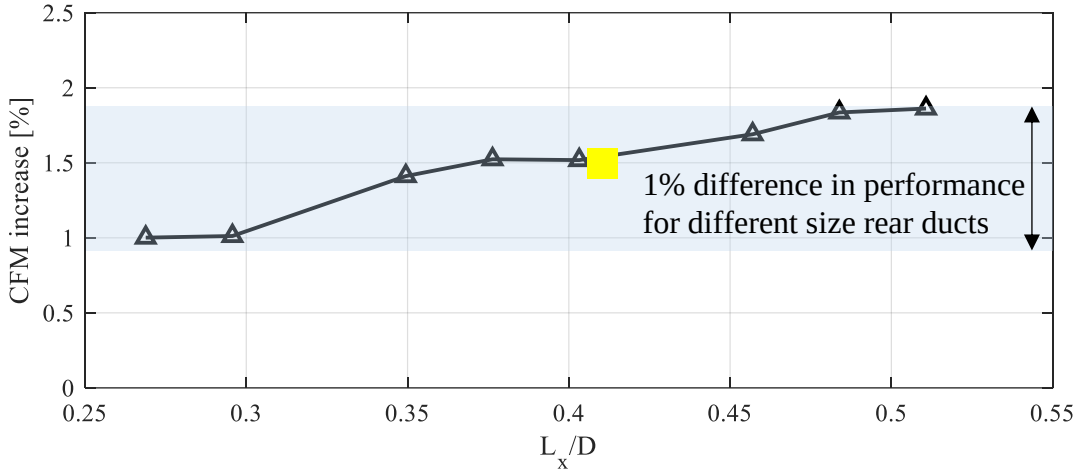

Figure 4.20: Volumetric flow rate (CFM) increase as a function of the length of the rear duct for $a_1 / a_2 = 0.85$, and $\psi = 0$. Yellow square indicates rear duct design.

The design of the inlet and rear duct using the dynamic programming methodology resulted in the geometry shown in Figure 4.21(a). The height to length ratio ($\Theta > 0$) of the bellmouth is 0.64, the ellipse angle is 1º, the arc length to diameter ratio (*S/D*) is 0.21, and the length of the rear duct to diameter ratio is 0.42. The performance of the inlet and rear ducts are indicated by the red square in Figure 4.17 to Figure 4.20. This bellmouth inlet is herein referred to as the C-Bellmouth inlet. The DFDC predicted BL thickness along the duct is also shown in Figure 4.21(a) as a dashed blue line.

An additional bellmouth inlet has been designed with the *S/D* ratio relaxed. The second inlet designed is referred to as the Q-Bellmouth inlet. The Q-Bellmouth inlet has a *S/D* ratio of 0.41 and height to length of 0.8 indicated by the green square in Figure 4.17 to Figure 4.20. The Q-bellmouth inlet and the resulting BL thickness is illustrated in Figure 4.21(b). As illustrated here, the Q-Bellmouth inlet reduced the BL thickness by nearly 70%. A 3D view of the designed inlet ducts is shown in Figure 4.22.

It is important to note that the experimental results do not show the reduction in the BL thickness using the Q-Bellmouth as predicted by DFDC. The reason for this discrepancy is not understood. It is speculated that it can potentially be attributed to the fact that the fan is positioned in very close proximity of the inlet and the blade potential flow field affected the growth of the BL.

(a) (b)

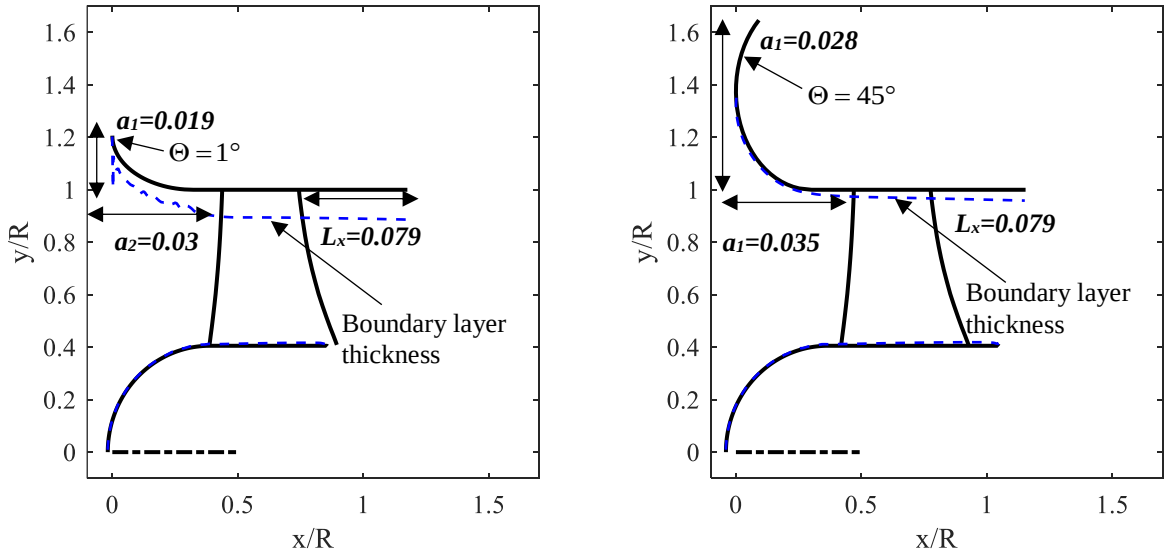

Figure 4.21: Inlet duct geometry and duct wall boundary for the (a) C-Bellmouth and, (b) Q-Bellmouth inlet (units in m).

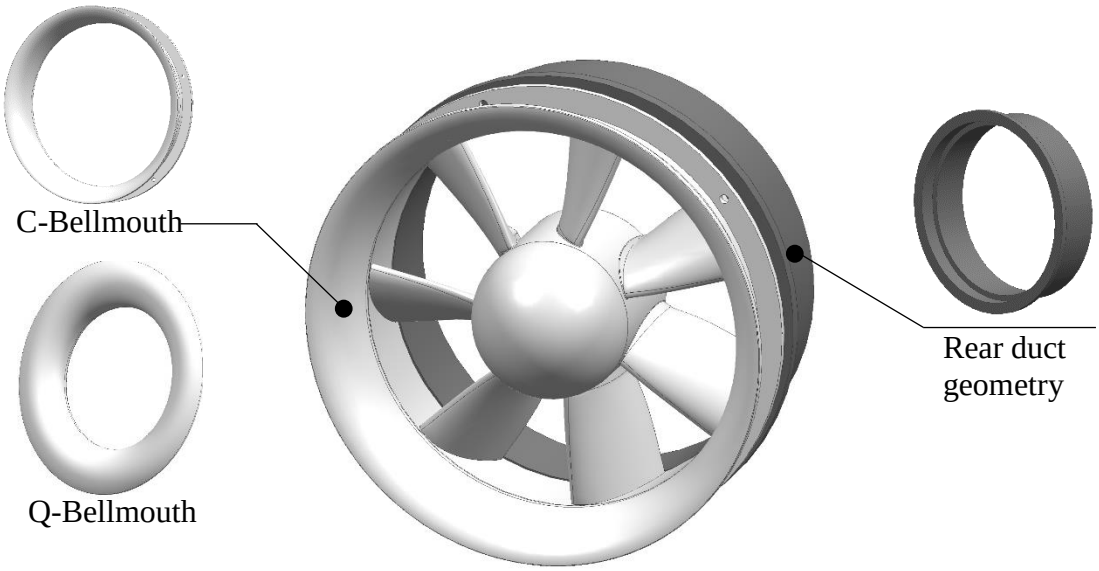

Figure 4.22: Fan C-Bellmouth and Q-Bellmouth inlet and rear duct geometry incorporated in to the fan design.

4.2 **Design of multi-element axial fans**

In this section, the implementation of multi-element airfoils in ventilation fans is investigated. Though multi-element airfoils are complex, a definitive trend towards implementing these geometries to axial compressors, wind turbines, and UAV propeller blades is ongoing. The main aims of investigating multi-element airfoils in this research are to assess their potential to i) improve aerodynamic performance and ii) reduce fan noise due to a decrease in the fan speed. To this end, the fan design approach presented in Section 4.1 is also applied to multi-element airfoils, i.e. design process is the same for single and multiple element airfoils. To this end, the polar for the multi-element airfoil is needed.

Unlike single element airfoils, there is no lift and drag polar data available in the open literature for multi-element airfoils at low Reynolds numbers. Consequently, the approach here is to design the multi-element configuration and to estimate the polars. The optimum design of the multi-element airfoil is a difficult task because of the large number of design variables, e.g. airfoil type, relative placement of elements, size of elements, etc. To simplify the design, it was decided to use the E214 airfoil geometry because its good aerodynamic characteristic at low Reynolds numbers. Secondly, the number of airfoils is limited to two. Consequently, hereafter the multi-element airfoil will be referred simply as a tandem airfoil.

The design of the tandem airfoil configuration using a dynamic programming methodology is presented in Section 4.2.1. The tandem airfoil polars are used to design the axial fan in Section 4.2.2.

4.2.1 Tandem Airfoil Design

The aim here is to design a tandem airfoil configuration with higher lift and lift to drag ratio than the single element airfoil. To this end, the design of the tandem airfoil is carried out at a chord Reynolds number of 200,000 ($RE_c = {c_{total} V_{rel}}/{v_{air}}$) using the viscous/inviscid MSES/MSIS solver presented in Chapter 3. The design parameters for the tandem airfoil are shown in Figure 4.23. They are the chord ratio (c_2 / c_1), gap size (defined when $\delta_1 = \delta_2 = 0$), vertical displacement of the rear element (d_{TE}), and main and rear airfoil deflection angles (δ_1 and δ_2), respectively.

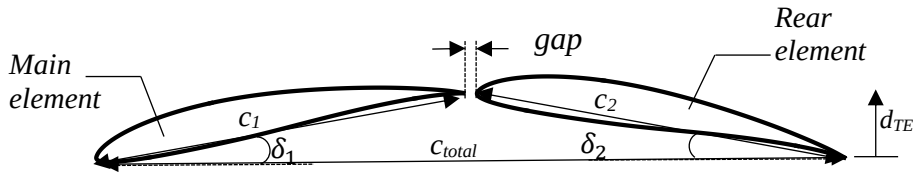

Figure 4.23: Design parameters for the tandem airfoil geometry.

The airfoil design is carried out by first investigating the effect of the design parameters individually in order to gain insight into the sensitivity of airfoil performance to these parameters. The sensitivity studies are presented in the form of plots of lift vs drag for a range of AoAs in Figure 4.24 through Figure 4.28.

Figure 4.24 shows the effect of the rear deflection angle (δ_2) when δ_1=12°, $c_1 / c_2 = 1$, gap =0, and d_{TE} = 0. As illustrated, the coefficient of lift increases as the deflection angle (δ_2) increases for the rear element up to a position where the leading edge of the rear airfoil is near the trailing edge of the main element. After the maximum lift is achieved, further increasing the deflection angle δ_2 results in a decrease in lift and an increase in drag until stall. Therefore, the airfoil polars are strongly sensitivity to deflection angle (δ_2). Figure 4.26 shows a similar trend when $\delta_1 = 10$ °, $c_1 / c_2 = 1$, gap =0, and d_{TE} = 0. However, the maximum CL that can be achieved is lower as δ_1 is decreased. When the rear deflection angle (δ_1) is further reduced to 8° the coefficient of lift is shown to increase with the rear deflection angle δ_2. However, here the CL continues to increase

for $\delta_2 > \delta_1$. Therefore, the rear element does not stall and the BL remains attached to the rear element.

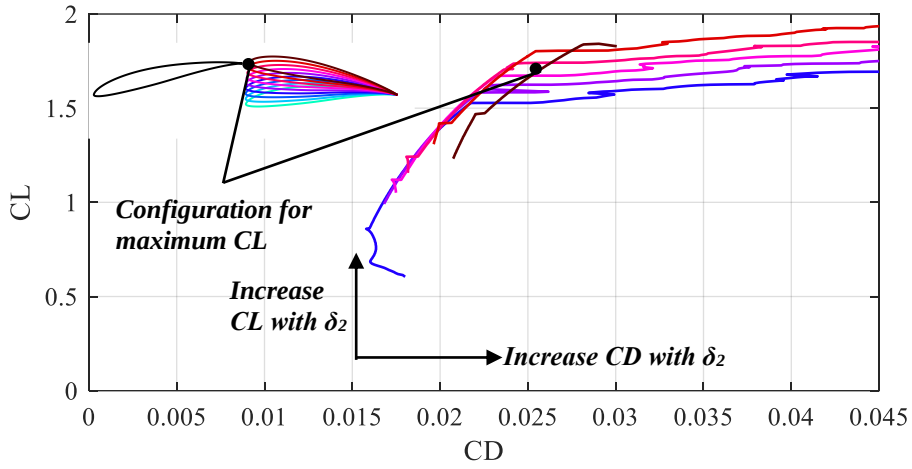

Figure 4.24: Tandem airfoil drag polar for δ_2=-6.5 to 14 when δ_1=12, $c_1 / c_2 = 1$, and gap =0 .

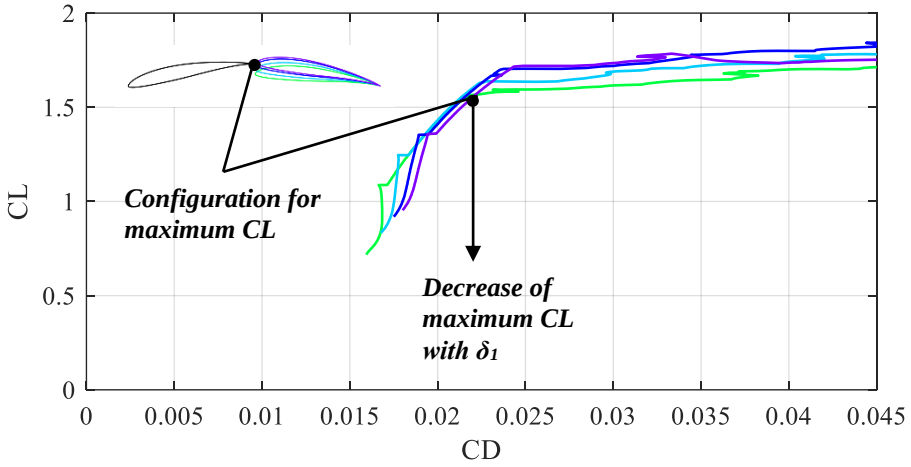

Figure 4.25: Tandem airfoil drag polar for δ_2=5 to 10.5 when δ_1=10°, $c_1 / c_2 = 1$, $d_{TE} = 0$, and gap =0.

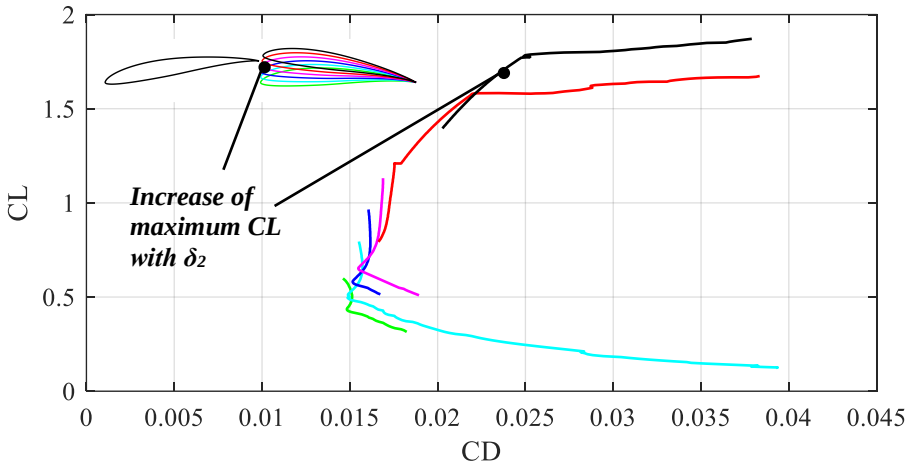

Figure 4.26: Tandem airfoil drag polar for δ_2=0 to 10 when δ_1=8°, $c_1 / c_2 = 1$, $d_{TE} = 0$, and gap =0.

The effect of vertical displacement of the rear element is shown in Figure 4.27. It is shown here that the coefficient of lift increases as the vertical displacement of the rear element (d_{TE}) increases. However, when the trailing edge of the main element is directly aligned to the leading edge of the rear element the lift and drag decrease instantly. This is likely due to the coupled phenomenon between the trailing edge flow of the main element due to the Kutta condition and the stagnation point of the rear element. Further increasing the vertical displacement of the rear element results in an increase of lift and drag relative to the aforementioned configuration.

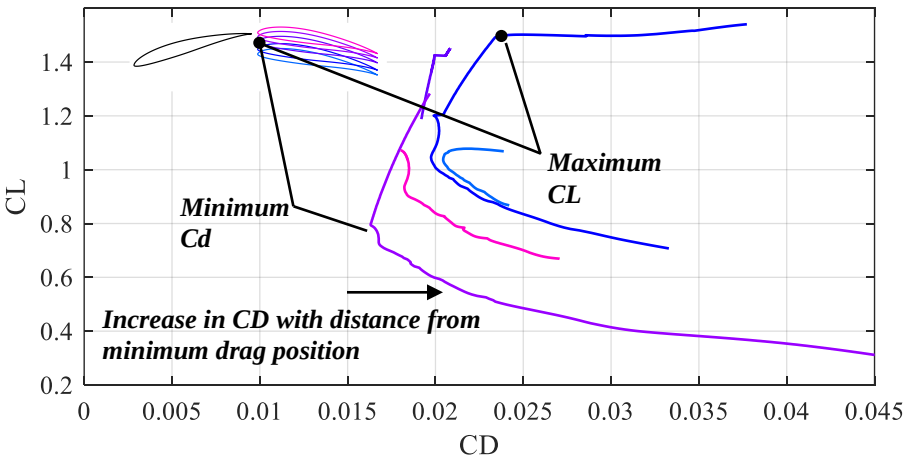

Figure 4.27: Tandem airfoil drag polar for d_{TE} from -0.12 to 0.048 when δ_1=12°, δ_2=10, $c_1 / c_2 = 1$, and gap = 0.

Figure 4.28 shows the effect of the gap size on the lift and drag of the tandem airfoil. As illustrated here, the lift increases and the drag decreases as the gap is reduced.

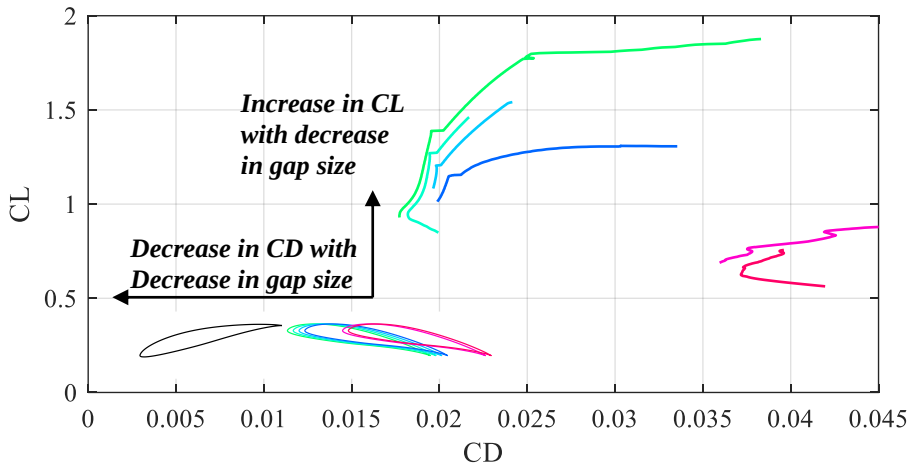

Figure 4.28: Tandem airfoil drag polar when gap/c_1= - 0.04 to 0.4600 when δ_1=12°, δ_2=10 , $c_1 / c_2 = 1$, and d_{TE} = 0.

To design the tandem airfoil, an iteration dynamic programming method was implemented using MSES to compute the aerodynamic properties for each iteration. To this end, various combinations of the variables shown in Figure 4.23 where analyzed resulting in the nearly optimum solution shown in Figure 4.29(a). The E214 tandem airfoil 2 (E214-T2) airfoil geometric parameters are listed in Table 4.1. However, concerns with the proximity of the rear element to the main trailing edge during fabrication of the airfoil led to a new design referred to as E214 tandem airfoil 3 (E214-T3) shown in Figure 4.29(b). The E214-T3 has the same geometric parameters as the E214-T2 airfoil with the exception of the rear element vertical displacement. As shown in Table 4.1, the E214-T3 is displaced down vertically 2% of the total chord relative to the E214-T2 airfoil. The drag and lift polars for both airfoils are shown in Figure 4.30 showing that both airfoils have similar aerodynamic performance. However, the E214-T2 airfoil generated less drag for coefficients of lift between 1.6 and 1.85 as shown in Figure 4.30(a). Figure 4.30(b) shows that the zero lift AoA increases by 1 degree for the E214-T3 airfoil configuration. However, the maximum lift is increased.

Figure 4.29: (a) E214-T2 airfoil geometry resulting in the best aerodynamic characteristics and **(b)** E214-T3 airfoil modified to accommodate for fabrication difficulties related to the proximity of the airfoils.

Table 4.1: E214-T2, and E214-T3 airfoil design geometric parameters.

Geometric parameter	E214-T2	E214-T3
Airfoil geometry	E214 airfoil	E214 airfoil
c_2 / c_1	1.0536	1.0536
Main airfoil deflection angle (δ_1)	12	12
Rear airfoil deflection angle (δ_2)	9.28	9.28
Gap size	0	0
d_{TE} *[% of the total chord]*	0	-2

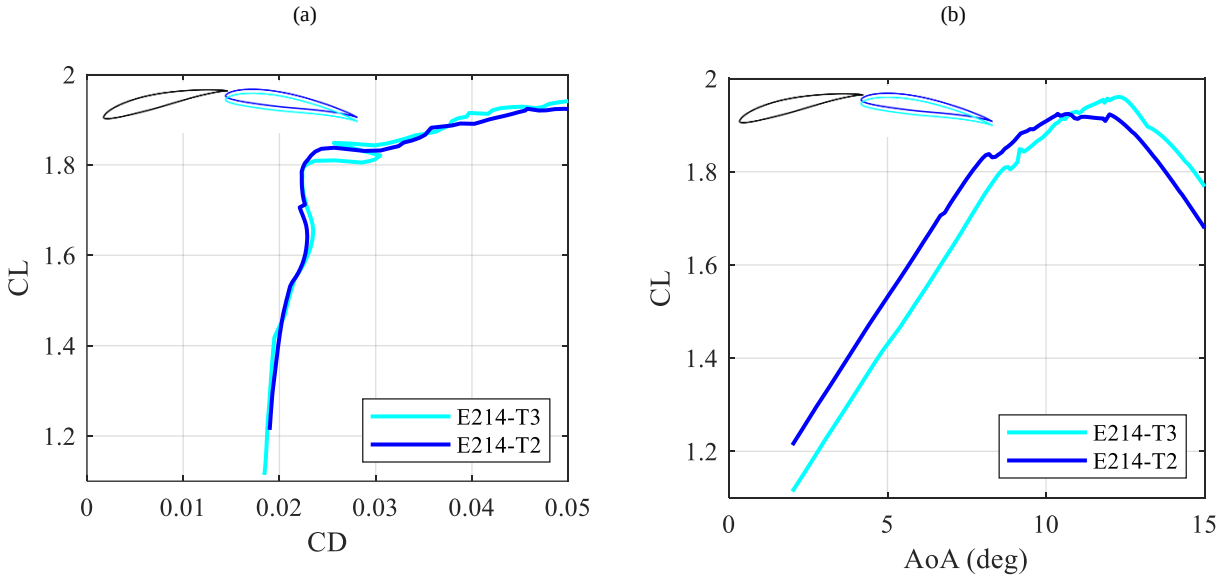

Figure 4.30: E214-T2 and E214 T3 clean airfoil **(a)** drag polar and **(b)** lift polar comparison.

The pressure coefficient of E214-T2 and E214-T3 airfoils at an AoA of 8 degrees is compared to the single element E214 airfoil in Figure 4.31. The chord for the single and tandem airfoils is the same (tandem airfoil chord is from leading edge of main to trailing edge of rear airfoil). As shown, the tandem airfoils increase the pressure difference at the rear end of the airfoil relative to the single element airfoil. The increased in performance is due to the accelerated flow in the gap of

the tandem airfoil that increases the kinetic energy of the flow on the suction surface of the subsequent airfoil. The first half of the tandem airfoil shows a similar pressure distribution as the single element airfoil. However, individual element of the tandem configuration exhibit lower chord Reynolds numbers relative to the single element airfoil. The lower chord Reynolds numbers leads to separation bubbles (shown in Figure 4.31) and a increase in turbulent BL thickness resulting in an increase in parasitic drag (Winslow et al., 2018). The separation bubble can also be seen in the viscous region, i.e. wake, of the rear element in Figure 4.32(a) and (b) for the E214 T2 and T3 airfoils, respectively. Additionally, the stagnation streamlines in Figure 4.32(a) and (b) show that the increased gap size for the E214-T3 airfoil results in higher flow velocities on the pressure side relative to the E214-T2 airfoil which results in a lower coefficient of pressure, i.e. lift. The coefficient of pressure contour for the single element airfoil in Figure 4.32(c) show that the coefficient of pressure is reduced at the second half of the E214 airfoil relative to the tandem airfoils. Therefore, a higher lift is achieved for the tandem airfoils.

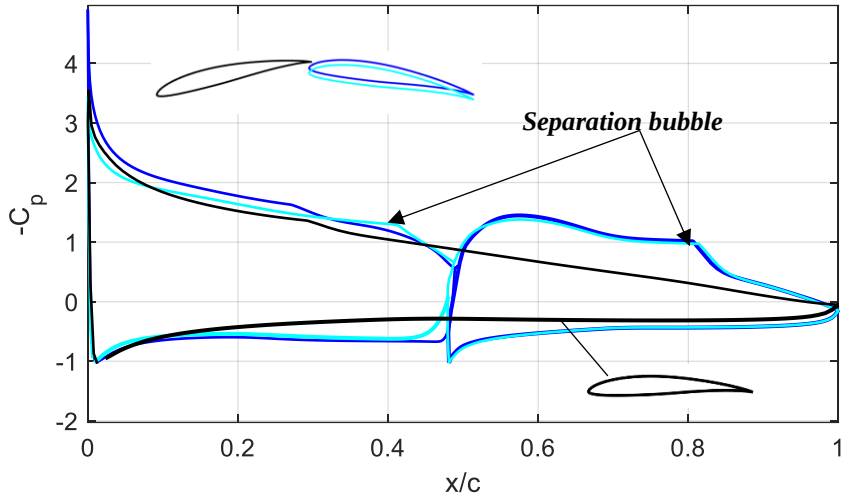

Figure 4.31: Pressure distribution for the clean E214-T2, E214-T3, and E214 single element airfoils at AOA = 8°, and Re = 200,000.

(a)

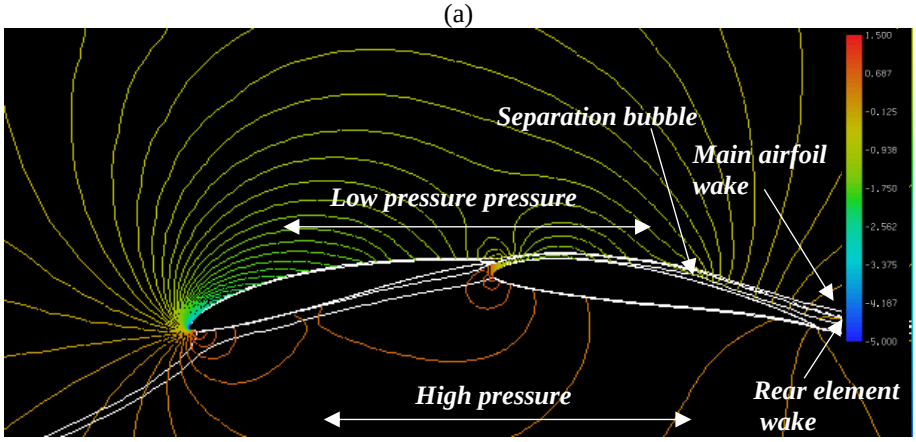

(b)

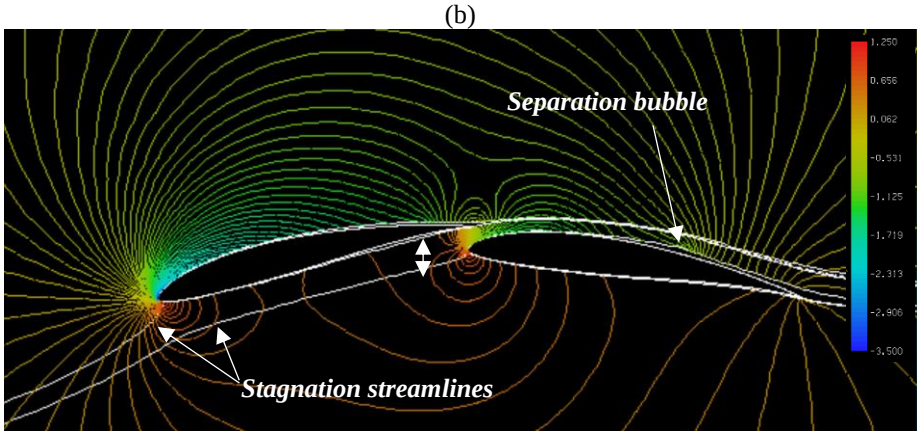

(c)

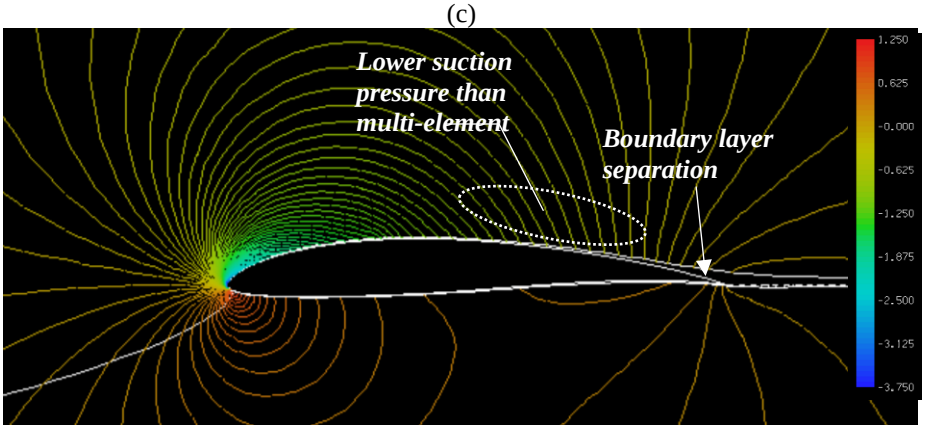

Figure 4.32: (a) E214 T2, **(b)** E214-T3 and **(c)** E214 airfoil coefficient of pressure contours at Re=200,000, and AOA=8deg.

Transition enhancement is a method for eliminating or reducing the intensity of the laminar separation bubble by tripping the laminar BL (Gopalarathnam et al., 2003). The trip enables transition from a laminar to a turbulent BL that is more capable of sustaining adverse pressure gradients. The chord-wise location of the trip has little effect on the drag as long as the trip is located upstream of the laminar separation bubble (Lyon et al., 1997). Consequently, the E214 T2 and T3 airfoils have been tripped upstream of the separation bubbles of the main and rear elements.

The transition locations for each tandem airfoil are presented in Table 4.2. As illustrated in Figure 4.33, tripping of the airfoils resulted in the elimination of the separation bubbles while preserving the same pressure distribution. Consequently, resulting in a decrease in the drag while maintaining a comparable coefficient of lift as shown in Figure 4.34 for the E214-T2 airfoil.

Table 4.2: Tandem airfoil trip locations.

Airfoil	x_1/c_1	x_2/c_2
E214-T2	0.80	0.50
E214-T3	0.70	0.45

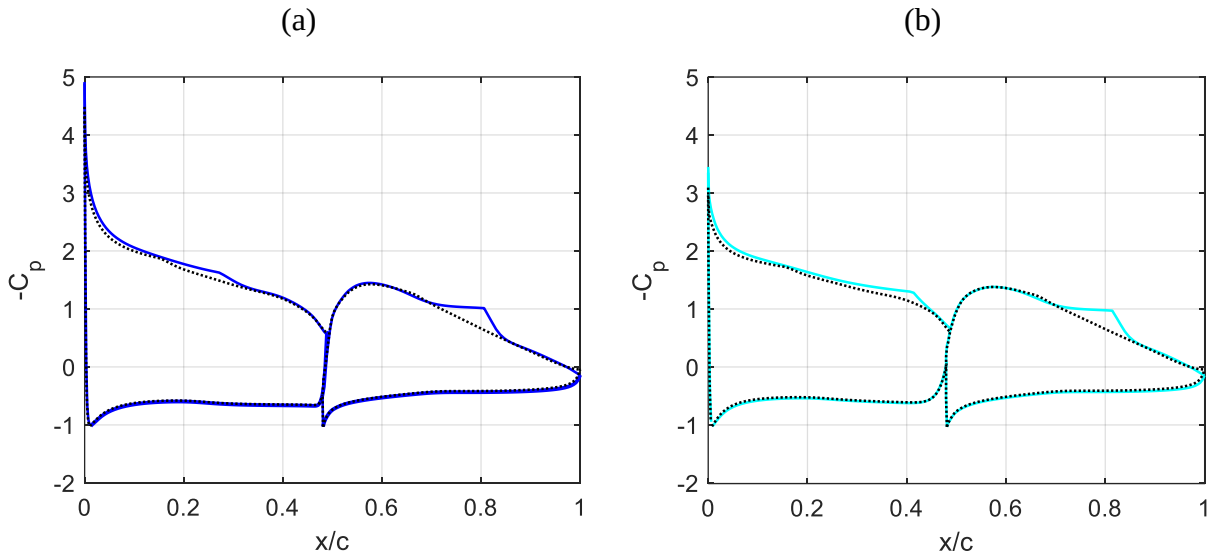

Figure 4.33: Coefficient of pressure for **(a)** E214-T2 and **(b)** E214-T3 airfoils polar for tripped (dotted lines) and clean (solid lines) airfoils at AoA =8 deg, and Re=200,000.

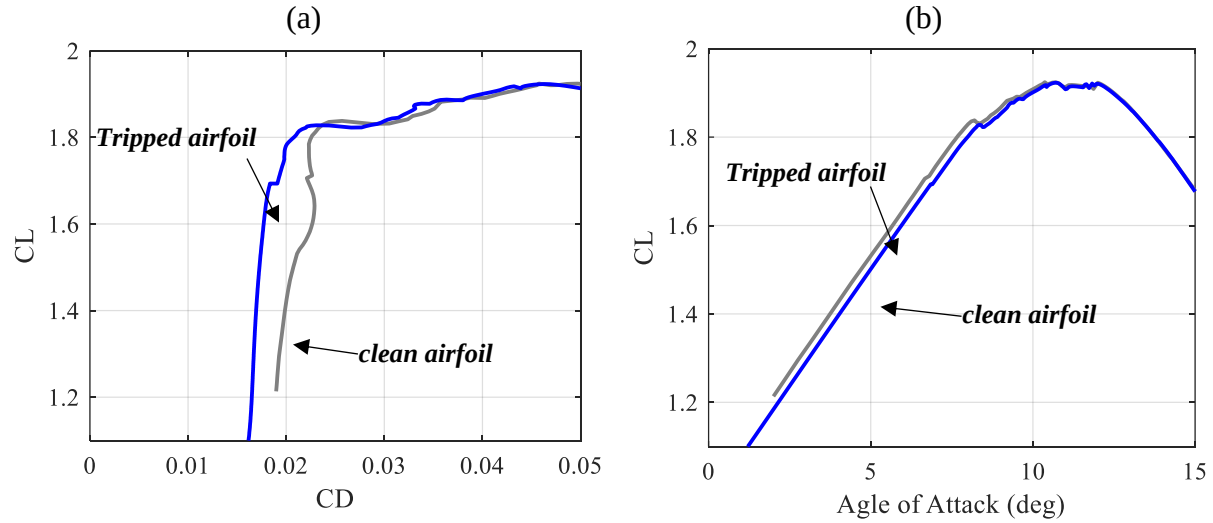

Figure 4.34: Comparison of the **(a)** drag and **(b)** lift polar for the tripped and clean E214-T2 airfoil at a Re=200,000.

The lift and drag polars for the tripped E214-T2 and E214-T3 airfoils are compared to the E214 single element airfoil in Figure 4.35. As illustrated here, the tandem airfoils resulted in an increase of the coefficient of lift by approximately 35%. However, as shown in Figure 4.36 the lift to drag ratio was slightly increased while increasing the coefficient of lift. Therefore, the penalty caused by the increase in drag is more than offset by the gain in the lift coefficient. Table 4.3 directly compares key aerodynamic parameters for the E214-T2, E214-T3, and E214 single element airfoils at their maximum lift to drag ratio. It is illustrated here that the E214-T2 airfoil increased the drag by 36% while increasing the lift by 43%. The E214-T3 increased the drag by 46% while increasing the lift by 46%.

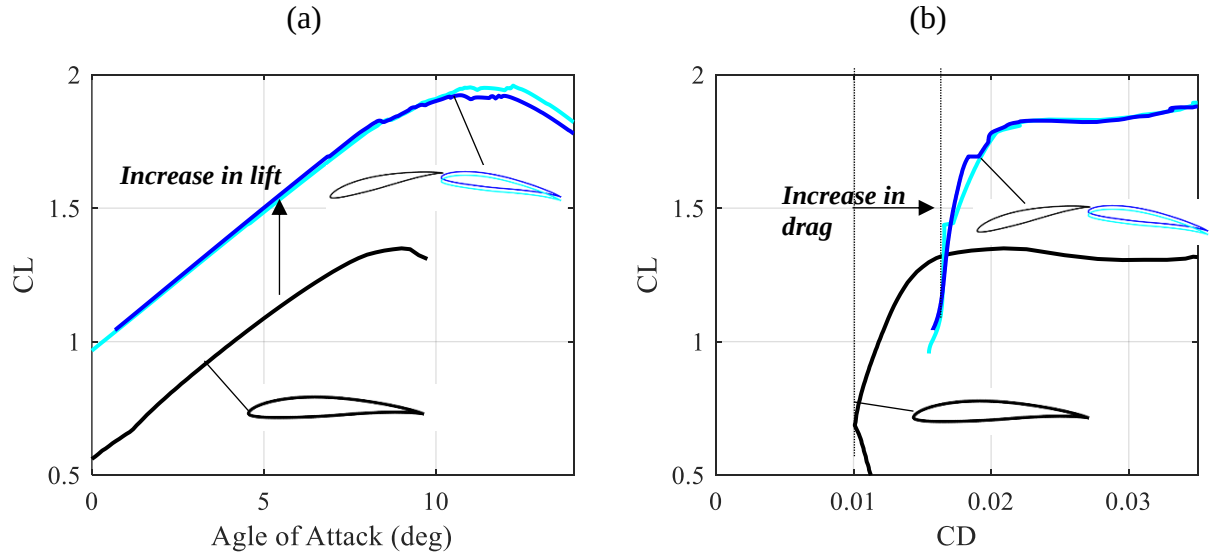

Figure 4.35: Airfoil **(a)** Lift and **(b)** Drag polars comparison for the tripped E214-T2, E214-T3, and Single element airfoils at Re=200,000.

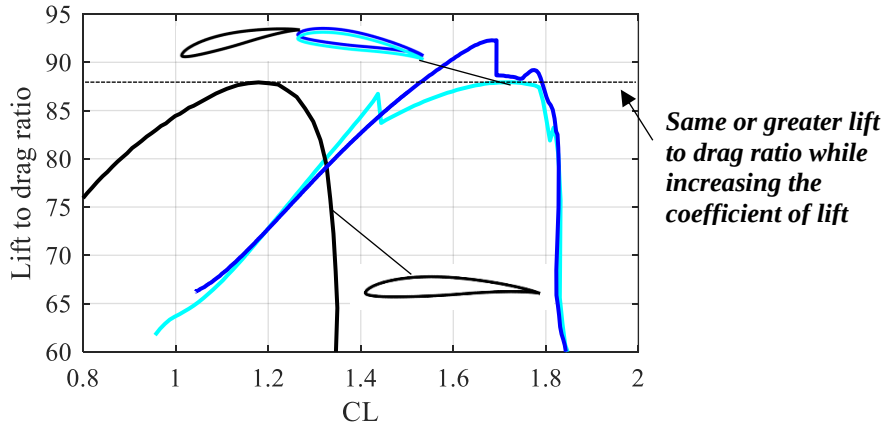

Figure 4.36: Lift to drag ratio as a function of the coefficient of lift for the tripped E214-T2, E214-T3, and Single element airfoils at Re=200,000.

Table 4.3: Direct comparison of the aerodynamic characteristics of the E214-T2, E214-T3 and E214 single element airfoils.

Airfoil	AoA for max CL	CL max	LD max	CD at LD max	CL at LD max
E214-airfoil	9	1.349	87.92	0.01341	1.179
E214-T2	10.7	1.92	92.28	0.01835	1.693
E214-T3	11.4	1.951	87.93	0.01964	1.727

4.2.2 Multi-element Airfoil Blades Design

In this section, the two tandem airfoils from section 4.2.1 have been used in the design of the fan using the approach presented in Section 4.1. The tandem airfoil fans will be referred to as Control Vortex Tandem (**C**ontrol-**V**ortex **T**andem). Hence, CVT2 and CVT3 for airfoils E214-T2 and E214-T3, respectively. The CVT2 and CVT3 fans have been designed to have the same diameter (0.186 m) and volumetric flow rate (1000CFM) as the CVS fan. Hence, the approach here is to design the CVT2 and CVT3 fans to generate the axial and swirl velocity profiles in Figure 4.10(a) and (b) using the polars for the E214-T2 and E214-T3 airfoils, respectively. However, the airfoil characteristics can vary based on Reynolds number as described in Section 4.1.1. Consequently, the two tandem airfoil polars were recomputed for the expected Reynolds number at the hub and tip. Figure 4.37 shows the different polars, polar at 200k Re and the polars actually used at the hub (70k Re) of and at the tip (120 Re) of the blade. It is interesting here that he Reynolds number has a more unfavourable effect on the Coefficient lift than expected relative to a single element airfoil. The reason here is likely that a decrease in the total chord Reynolds number increases the viscous effects of the individual elements of a multi-element airfoil more than a single element airfoil. This is because the chord Reynolds numbers of each element is nearly half of that of the total chord Reynolds number.

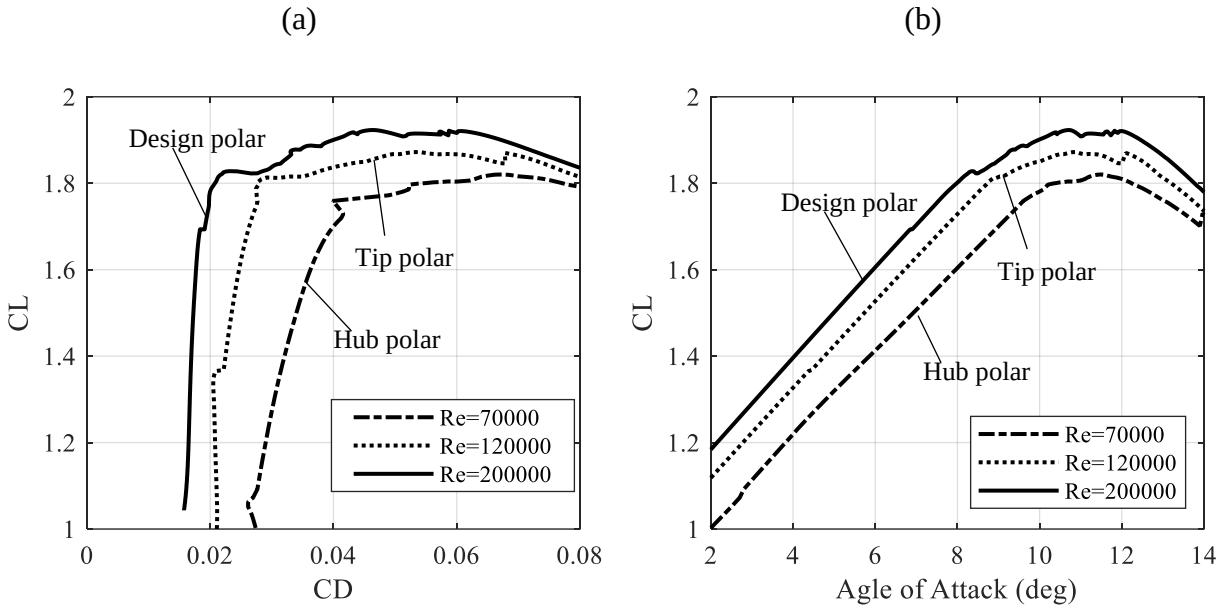

Figure 4.37: E214-T2 airfoil **(a)** Drag, and **(b)** Lift polar at RE=200,000, 120,000, and 70,000.

Unlike the design of the CVS fan, the CVT2 and CVT3 fans were designed to have the minimum tip speed of 0.1 for the 0.405 hub to tip ratio. In fact, the number of blades was reduced to 5 (relative to 7 for the CVS fan) to increase the chord size to be comparable to the chord size of the CVS fan. Figure 4.38 shows the chord and twist for the CVS, CVT2 and CVT3 fans. As illustrated here, the twist increased for the CVT2 and CVT3 fans since the tandem airfoils operate at higher angles of attack. However, the overall change in chord from the blade hub to the tip is the same. Figure 4.39 shows the 3D blade geometry of the CVS, CVT2, and CVT3 fans. As illustrated here, the tandem airfoils are significantly thinner which leads to a reduction in the thickness noise. The geometry of the 3 fans is compared in Figure 4.40. As illustrated here, the CVT2 and CVT3 are geometrically very similar.

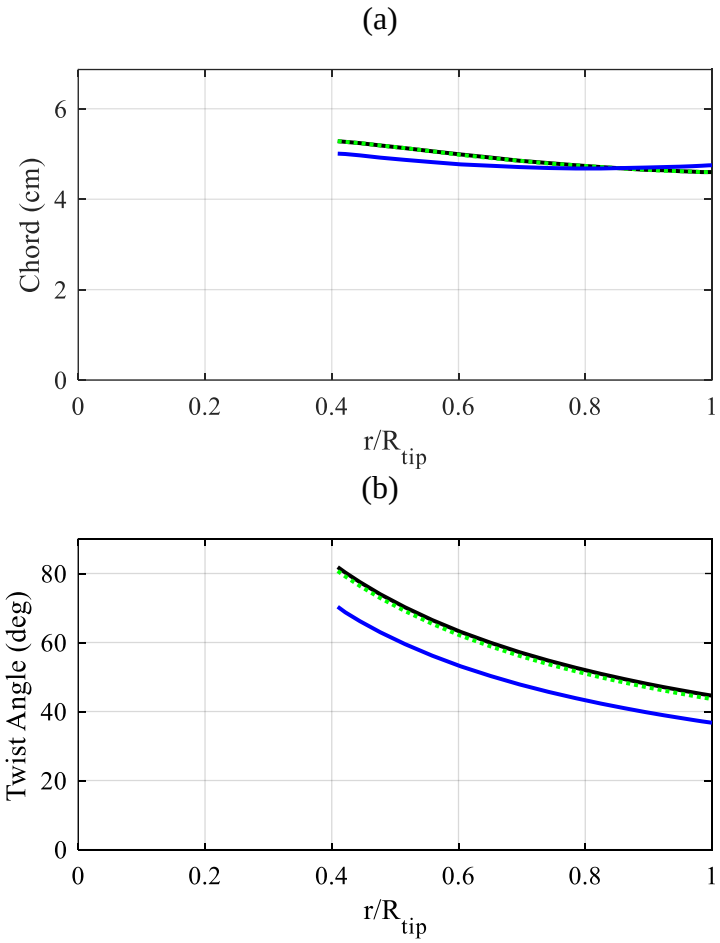

Figure 4.38: Spanwise **(a)** Chord and **(b)** twist distribution for the CVT2 (5 blades) , CVT3(5 blades), and CVS (7 blades) fans.

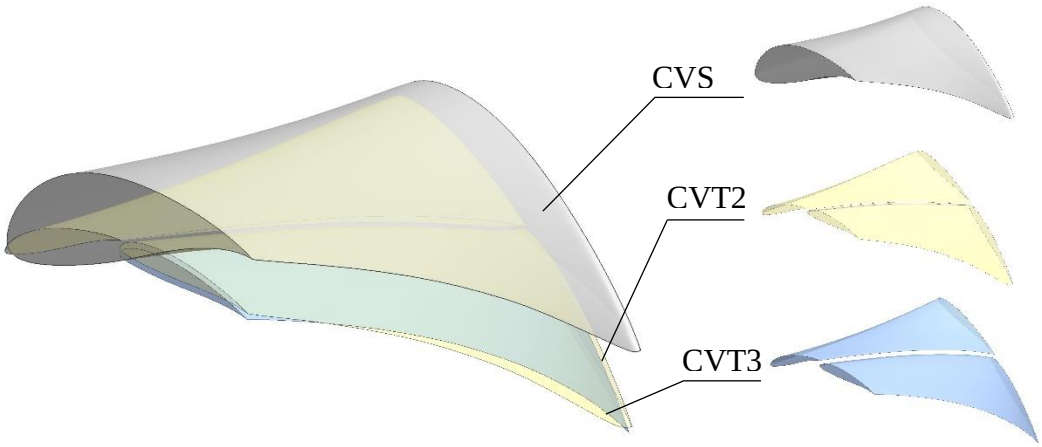

Figure 4.39: Comparison of the blade geometry for the CVS, CVT2, and CVT3 fan.

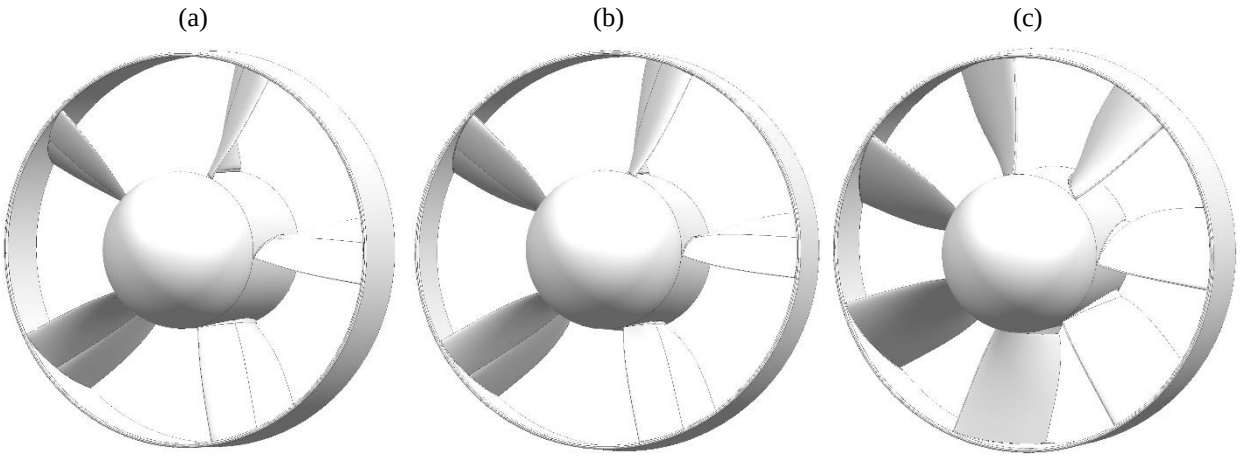

Figure 4.40: (a) CVT2, (b) CVT3, and (c) CVS fans blade geometry consisting of the designed blades and added fan hub and ring.

The overall performance of the CVS, CVT2, and CVT3 is very similar as shown in Table 4.4. However, the CVT2, and CVT3 fans operate at a lower tip Mach number. Figure 4.41 shows the volumetric flow rate as a function of the fan speed. As illustrated here, the CVT2 and CVT3 fans generate a higher volumetric flow rate for the same fan speed. Figure 4.42 shows that the CVT2, and CVT3 fans consume roughly the same power for the same volumetric flow rate.

Table 4.4: Aerodynamic performance of the CVS, CVT2, and CVT3 fans at the design speed.

Fan design	Number of blades	Design Volumetric flow rate	Design Fan speed	Design tip speed [mach]	Design power
CVT2	5	1038	3500	0.105	174
CVT3	5	1038	3500	0.105	174
CVS	7	1037	4000	0.115	165

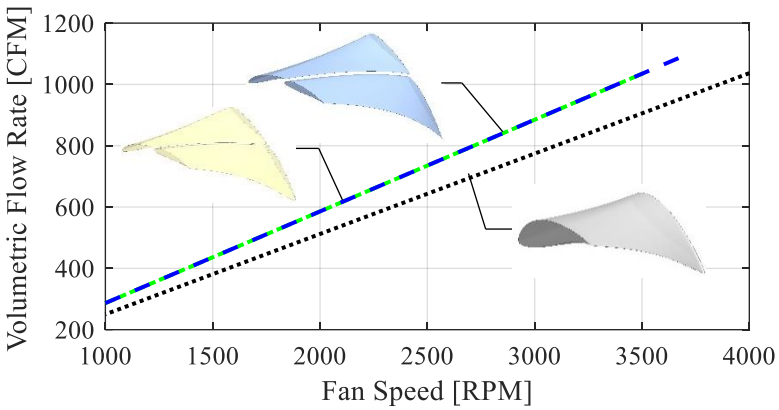

Figure 4.41: Volumetric flow rate as a function of the fan speed for the CVS, CVT2, and CVT3 fans.

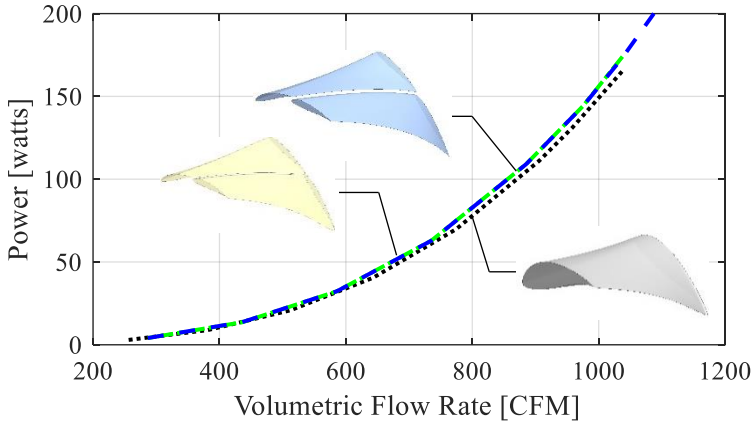

Figure 4.42: Mechanical power as a function of the volumetric flow rate for the CVS, CVT2, and CVT3 fans.

CHAPTER 5

5 Experimental Results and Validation

This chapter outlines the research facility, fan test rig, and instrumentation used in the experiments. Furthermore, a validation of the aerodynamic and acoustic prediction tools is presented. The focus of the noise data is to gain insight into the sources of noise of fans designed with single and tandem airfoils. Additionally, the tandem airfoil data provided is a first step towards development of future acoustic prediction tools that can be used for multi-element airfoil fans.

5.1 Experimental facility, fan test rig, and instrumentation

This section describes the facility, test-rig, and instrumentation developed for the acoustic and aerodynamic experimentation of the fans designed in Chapter 4. To this end, all aspects of the fabrication of the test-rig and the fan prototypes are presented. Additionally, the selection of the quiet motor to drive the fan is described.

5.1.1 Experimental Facility

All of the experiments were carried out inside the Mechanical Engineering anechoic chamber (cutoff frequency of 100 Hz) at Virginia Tech. The dimensions of the anechoic chamber are 5.4x4.1x2.4m from wedge tips to wedge tips. The experiments are focused on measuring the fan speed, flow profile, motor torque and noise.

5.1.2 Fan Test Rig

The prototype of the CVS, CVT2, and CVT3 fans designs in Chapter 4 have been fabricated using additive manufacturing by Protolabs. The material used was an opaque white SLA plastic that behaves similarly to a polypropylene/ABS mix. The tolerances in the X/Y/Z dimension are ±0.001"/in. (0.001mm/mm). The parts are smoothen to a 400 grit standard finish. A comparison of the CAD geometry with the 3D printed prototype of the CVS, CVT2, and CVT3 fans is illustrated in Figure 5.1. A close up view of the leading and trailing edge of the blades is also shown. Figure 5.1(a) shows that the finish of the blades is very good. Particularly the trailing edge

is shown to be very uniform, sharp, and with minimum defects, i.e. chipping of the blades. Figure 5.1(b) shows the finish of the CVT2 fan which is inherently more complex due to the tandem-element airfoil geometry with a small gap. Here the trailing edge of the airfoils are shown to have less uniformity along the blades with chipping of the trailing edge of the main and rear elements. Especially the trailing edge of the rear element shows significant damage from the removal of the support material for 3D printing. As highlighted in Chapter 4, the proximity of the two airfoils significantly increases the difficulty of fabricating the fan. To alleviate this concern, the CVT3 fan was designed with a modified version of the airfoil used for the CVT2 fan. The 3D printed prototype for the CVT3 fan is shown in Figure 5.1(c). Here, it can be shown that the quality of the finish is significantly better. Particularly a decrease in chipping is observed which is complimented by an increase of uniformity along the trailing edge of the blades.

The fabrication of the C-Bellmouth and Q-Bellmouth inlet designed in Chapter 4 have also been fabricated using 3D printing technology. The C-Bellmouth inlet has been fabricated using standard ABS and white SLA plastic materials (used to fabricate the fans) by 3D Hubs and Protolabs, respectively. The standard ABS material is 3D printed using FDM (Fused Deposition Modeling) with a layer thickness of 200 microns. The C-Bellmouth inlet 3D printed using the ABS material is herein referred to as C1-Bellmouth inlet. The C-Bellmouth inlet 3D printed using the white SLA material is herein referred to as C2-Bellmouth inlet. The Q-Bellmouth inlet was 3D printed using the white SLA material. Figure 5.2 shows the bellmouth inlet prototypes.

The prototype fans have been tested in conjunction with the C1, C2, and Q-Bellmouth inlets. Figure 5.3 shows a side view of the experimental test rig with the fan fitted with the different inlets tested. An exploded view of the experimental test rig is shown in Figure 5.4. The test-rig implements a Brushless DC (BLDC) motor to drive the fans. The BLDC motor is coupled to the fans using a motor shaft collar and a mounting plate as shown in Figure 5.4(a). The motor is supported by a motor clamp and a swept strut downstream of the fan. An aerodynamic motor sleeve is added to eliminate the cavity or backward and forward steps between the fan and the motor and the potential for parasitic noise. The fan is then enclosed with an inlet and outlet ducts. Additionally, a rotating shroud is added to the fan to eliminate the leakage flow from generating

tip gap noise as shown in Figure 5.4. The rotating shroud also increases the structural strength of the blades that decrease potential damage of the brittle 3D printed material.

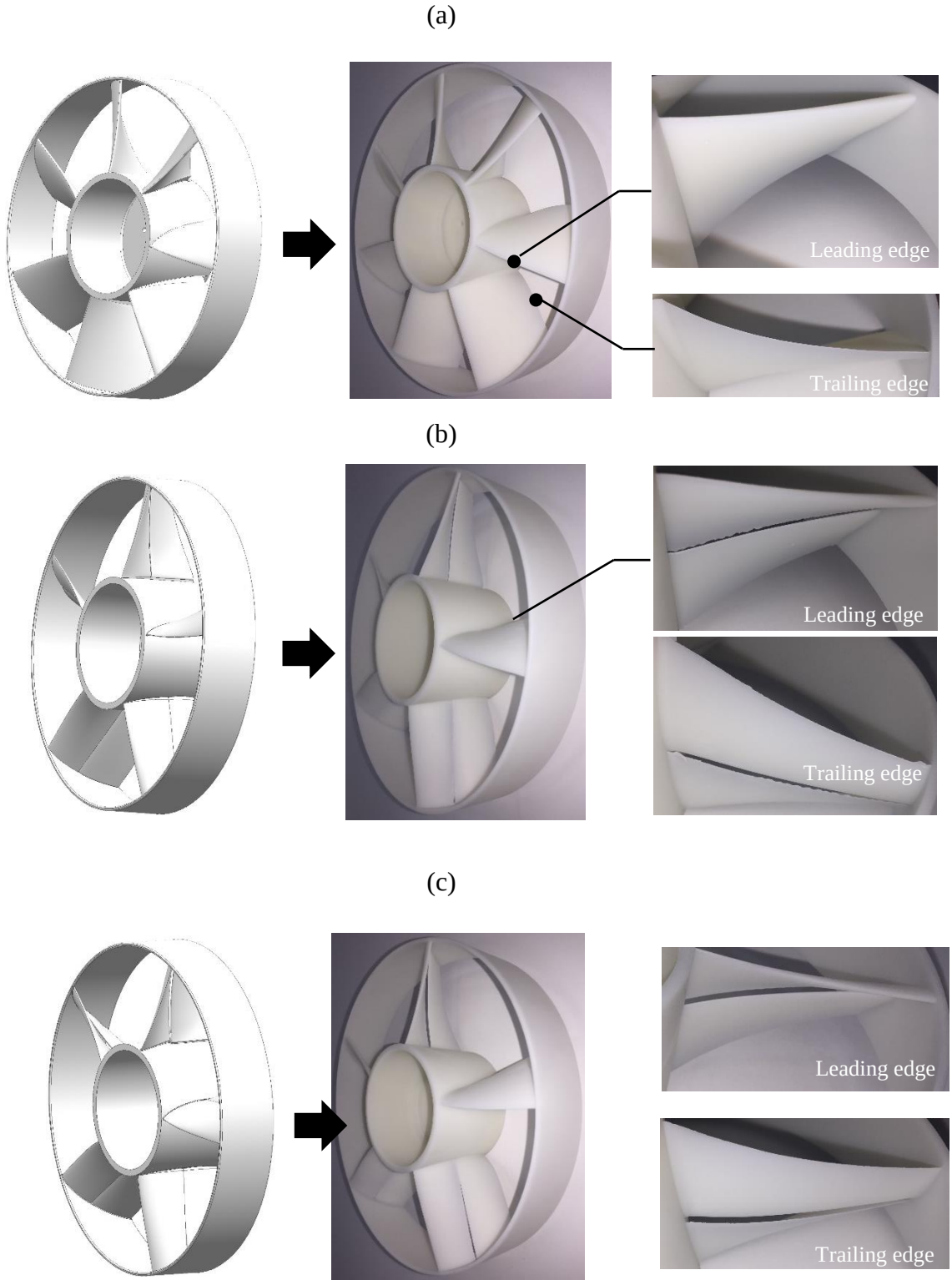

Figure 5.1: Comparison of the CAD geometry and the 3D printed prototype of the **(a)** CVS, **(b)** CVT2, and **(c)** CVT3 fan. Detailed views show the leading and trailing edge along the blades span

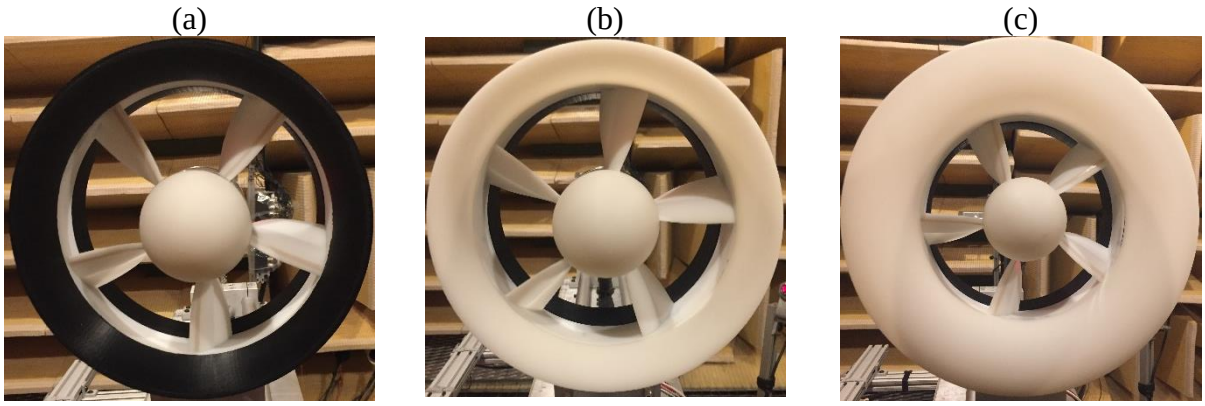

Figure 5.2: 3D printed prototype of the **(a)** C1-Bellmouth inlet, **(b)** C2-Bellmouth inlet, and **(c)** Q-Bellmouth inlet using standard ABS (black) and SLA plastic (white).

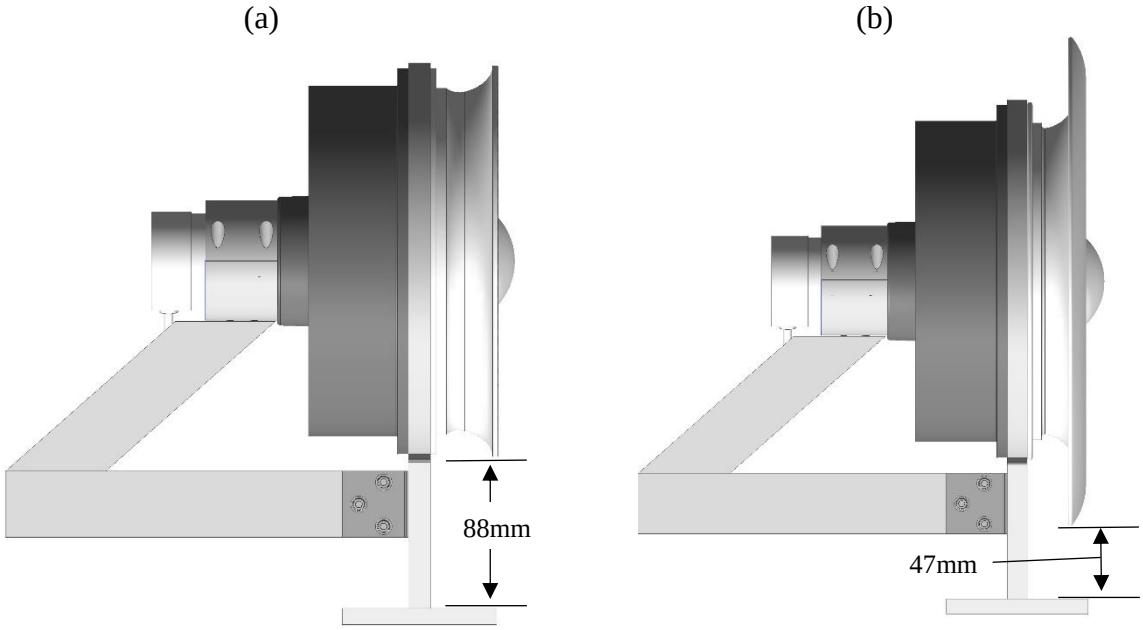

Figure 5.3: Side view of the experimental test rig with **(a)** C-Bellmouth, and **(b)** Q-Bellmouth inlets geometries.

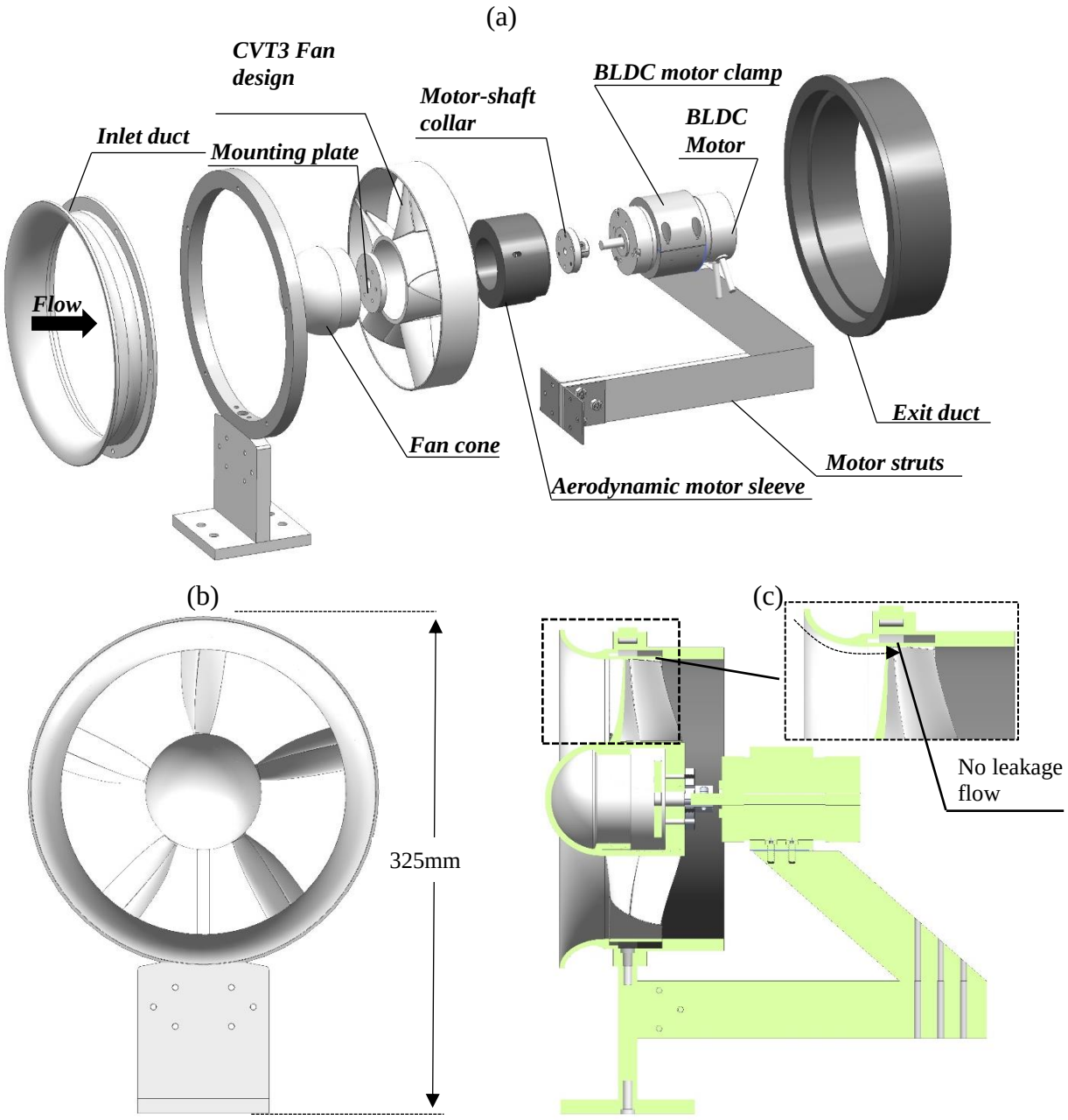

Figure 5.4: Fan test rig **(a)** exploded view showing the components of the test rig. Front view **(b)** shows the motor strut results in small flow blockage. Lastly **(c)** shows the cross section view of the test rig and the method for eliminating the tip leakage vortex.

Several BLDC motors with suitable speed and torque characteristics were consider. However, information regarding the motor noise was non-existent. To this end, 5 candidate motors were selected and tested at Virginia Tech. The aim of this experimental investigation was to select a motor with low noise levels so that the aerodynamic noise was the dominant source. The 5 motors

considered are shown in Figure 5.5 with the corresponding characteristics per manufacturer datasheets shown in Table 5.1.

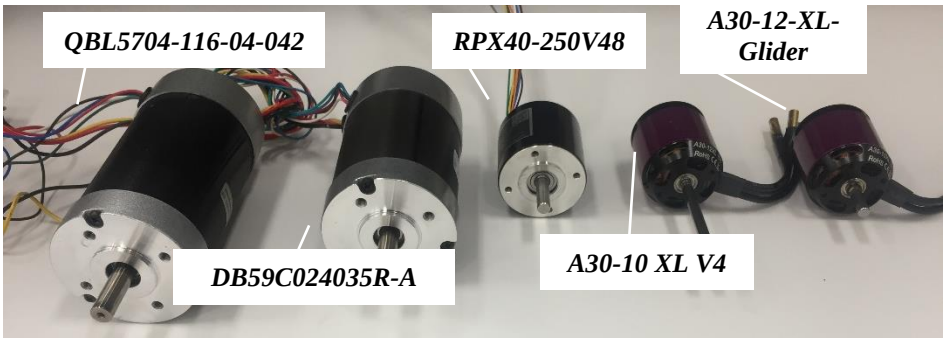

Figure 5.5: Candidate BLDC motors tested for noise to enable the selection of a quiet motor to driving the fan.

Table 5.1: Motor characteristics of the candidate motors.

Motor	Rated torque [n-m]	Rated Speed [RPM]	Power [watts]	Diameter [mm]	Axial length [mm]
DB59C024035R-A	1.79	3500	220	57	93
A30-10 XL V4	0.651	6000	722	43	45
A30-12-XL-Glider	0.5	6100	500	43	48.5
QBL5704-116-04-042	0.42	4000	160	57	116
RPX40-250V48	0.25	4075	140	41	40

The motors were tested unloaded and loaded using an inertial dynamometer. However, the dynamometer rotating flywheel and belt used for loading the motor resulted in high noise levels. Consequently, only results of the unloaded motors were considered to characterize the motor noise at different speeds. Results will show that the motor was not a dominant noise source. The motors were tested in the reverberation chamber at Virginia Tech using the experimental set up shown in Figure 5.6. The volume of the reverberation chamber is 46.67m^3. The measurements were performed using 8 microphones randomly placed in the room away from the source and the hard surfaces (in the reverberant field). The sound power level is computed as

$$L_w(f) = L_{spl,avg}(f) + 10\log_{10}(V_{room}) - 10\log_{10}(T_{60}(f)) - 13.9 \quad \textbf{(5.1)}$$

where $L_{spl,avg}$ is the average sound pressure level measured by the microphones, V_{room} is the volume of the reverberation chamber, and T_{60} is the reverberation time.

The motor's speed was measured using the optical sensor shown in Figure 5.6. The measured 1/3rd octave band sound power spectra for the 5 candidate motors (unloaded) is presented in Figure 5.7 and Figure 5.8 at 3000 and 4000 RPM, respectively. It is clear form these figures, that the DB59 and QBL5704 motors are the better options since they are significantly quieter than the other 3 motors. However, the size of the DB59 motor is significantly smaller than the QBL5704 motor as shown in Figure 5.5. A more compact motor is desirable as it will be less intrusive to the flow measurements. Therefore, due to the compactness, power, design speed, and noise level, the DB59 motor has been selected to drive the fans. The motor spectrum for the DB59 motor at different speeds is presented in Figure 5.9. As illustrated here the overall sound power level for the DB59 motor at full speed (4500 RPM) is 54.4 dBA.

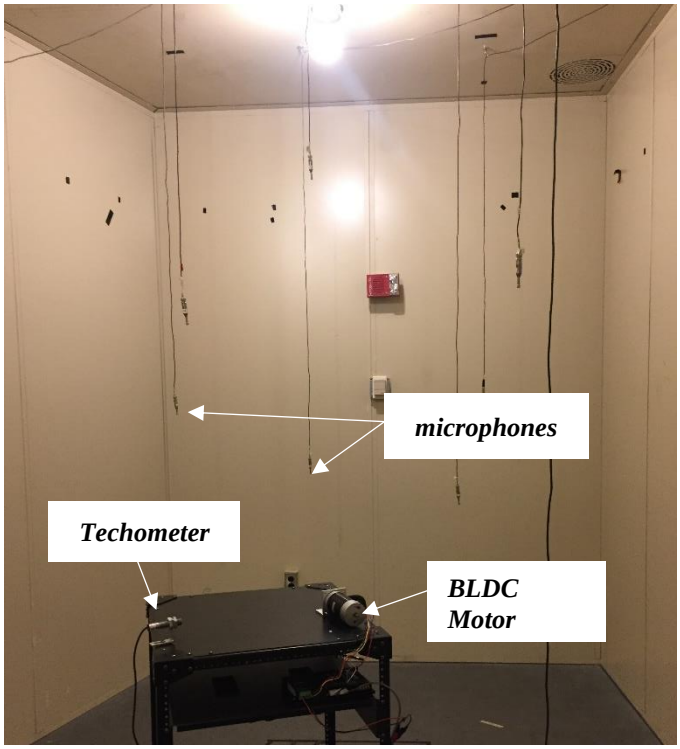

Figure 5.6: Test set up in the Reverberation Chamber consisting of the BLDC motor, tachometer to measure the motor speed, and microphones to measure the sound power level.

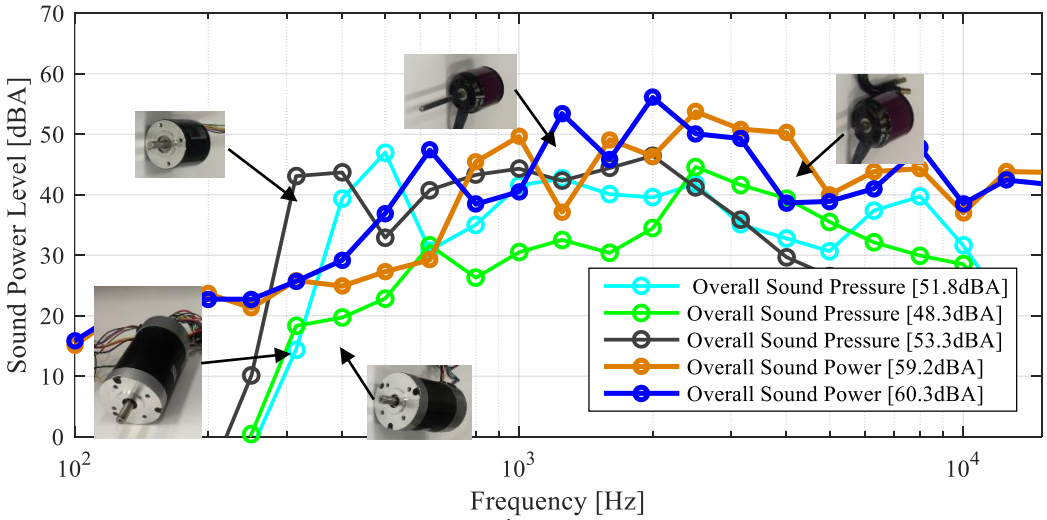

Figure 5.7: Sound power level spectrum in 1/3rd octave bands for the candidate motors at 3000 RPM.

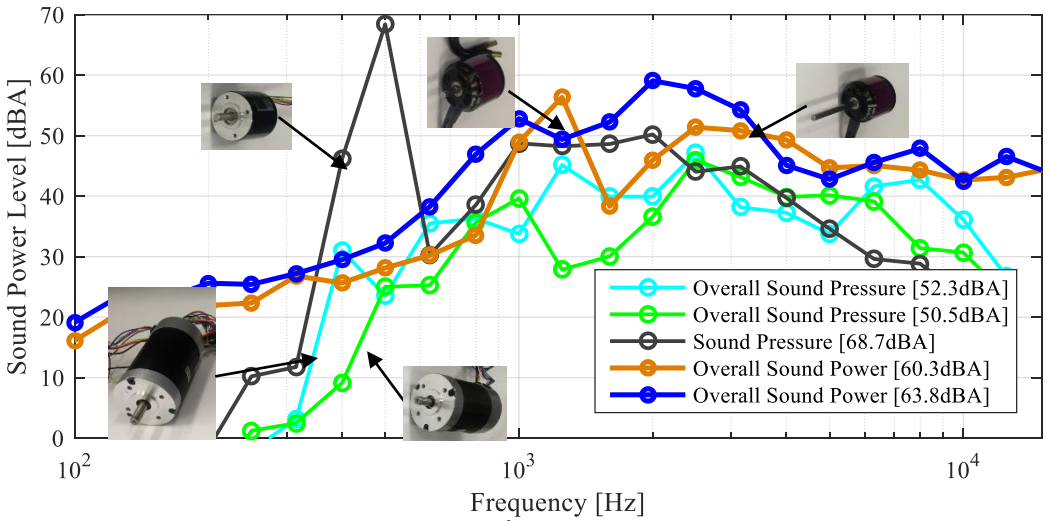

Figure 5.8: Sound power level spectrum in 1/3rd octave bands for the candidate motors at 4000 RPM.

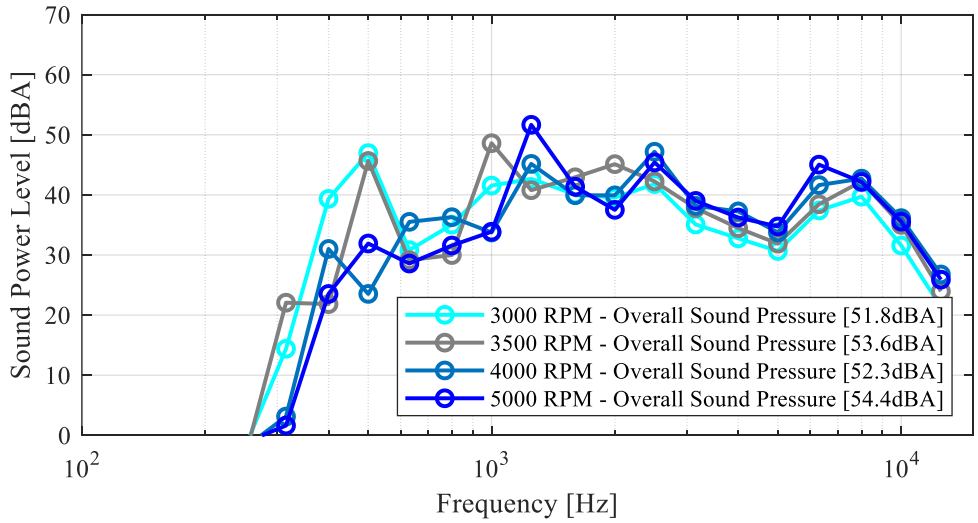

Figure 5.9: Sound power level spectrum in 1/3rd octave bands for the selected motor (DB59) at different speeds.

5.1.3 Instrumentation and Data Processing

5.1.3.1 Noise Measurements

The main noise instrumentation was a 2.8 m diameter far-field arc array shown in Figure 5.10. The far field arc is composed of 19 microphones evenly distributed along its circumference, i.e. from 0 to 180 degrees. The center of the arc array has been placed at the center of the fan. The microphones used in this array are Panasonic model WM-64PNT Electret microphones. These microphones have a flat frequency response from 20-16,000 Hz and a sensitivity of -44 +/- 3 dB Re 1V/Pa at 1 kHz. The microphones were calibrated using a Brüel & Klaer calibrator.

It is important to remark that the picture in Figure 5.10 shows the chamber door closed. However, the door was left completely open for all experiments. The reason is that the fan rig was set in the chamber such that the flow pointed towards the door. This configuration was selected for the purpose of minimizing the generation of turbulence in the chamber that when ingested by the fan results in a noise source.

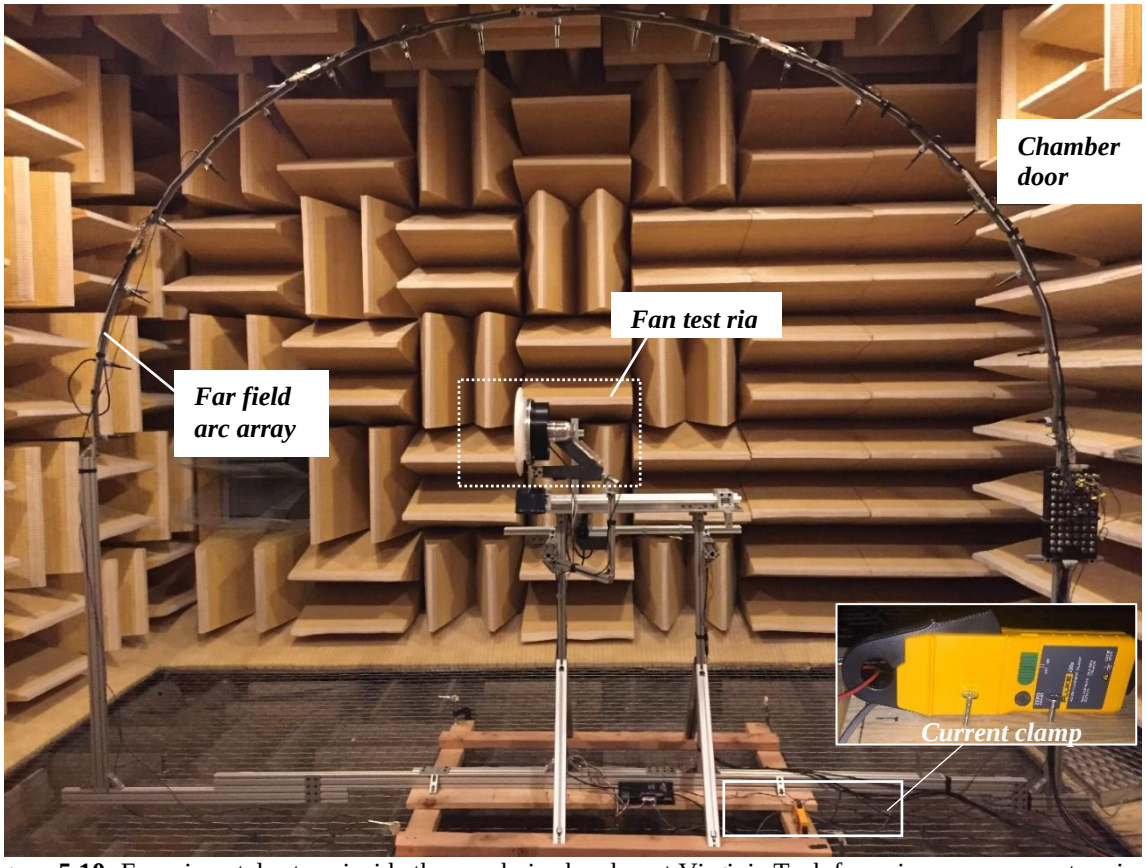

Figure 5.10: Experimental set-up inside the anechoic chamber at Virginia Tech for noise measurements using a 2.8m diameter far field arc array. Chamber door was always open for the noise tests.

The data from the microphones was collected for 20 seconds at a sampling frequency of 51200 Hz. All microphones where calibrated using a Brüel & Klaer calibrator type 4231 (94 dB at 1000 Hz) prior to each test. The sound pressure level spectrum for the calibrated microphone signals was computed using Welch's method with zero overlap, and 8192 length hamming windows. The sound pressure level in dB is then computed as

$$L_p(f) = 20\log_{10}\left(\frac{p_{rms}(f)}{p_{ref}}\right) \quad [dB] \tag{5.2}$$

where the reference pressure (P_{ref}) is $20 \cdot 10^{-6}[Pa]$.

The sound power spectrum is then computed as

$$W(f) \approx \sum_{l}^{N_m} I_l(f) S_l = \sum_{l}^{N_m} \frac{P_{rms-l}^2(f)}{\rho c} S_l \tag{5.3}$$

where N_m is the total number of microphones, $I_l(f)$ is the l^{th} acoustic intensity , and S_l is the surface area through which the intensity (I_l) propagates.

Figure 5.11 shows the top view of the arc array positioned parallel to the floor at the height of the center of the fan. The ring-like surface area S_{13} , corresponding to microphone number 13, shown in Figure 5.11 is computed as

$$S_l = 2\pi R_{arc} z \tag{5.4}$$

With

$$z = R_{arc}\left(\cos\left(\theta_a - \Delta\theta_a/2\right) - \cos\left(\theta_a + \Delta\theta_a/2\right)\right) \tag{5.5}$$

The sound power level spectrum is then computed as

$$Lw(f) = 10 \times \log_{10}\left(\frac{W(f)}{W_{ref}}\right) \tag{5.6}$$

where W_{ref} is the reference power of $10^{-12}[watts]$.

It should be noted here that microphones 1 and 2 in the arc array are located in the wake of the fan as shown in Figure 5.10. Consequently, the measurements from these microphones are

contaminated by flow hydrodynamic pressure. Thus, in the computation of the sound power level it is assumed that the fan radiates equally in the upstream and downstream directions. Consequently, the measurements made in microphones 18 and 19 directly opposite to 1 and 2 are used to compute the sound intensity by these microphones.

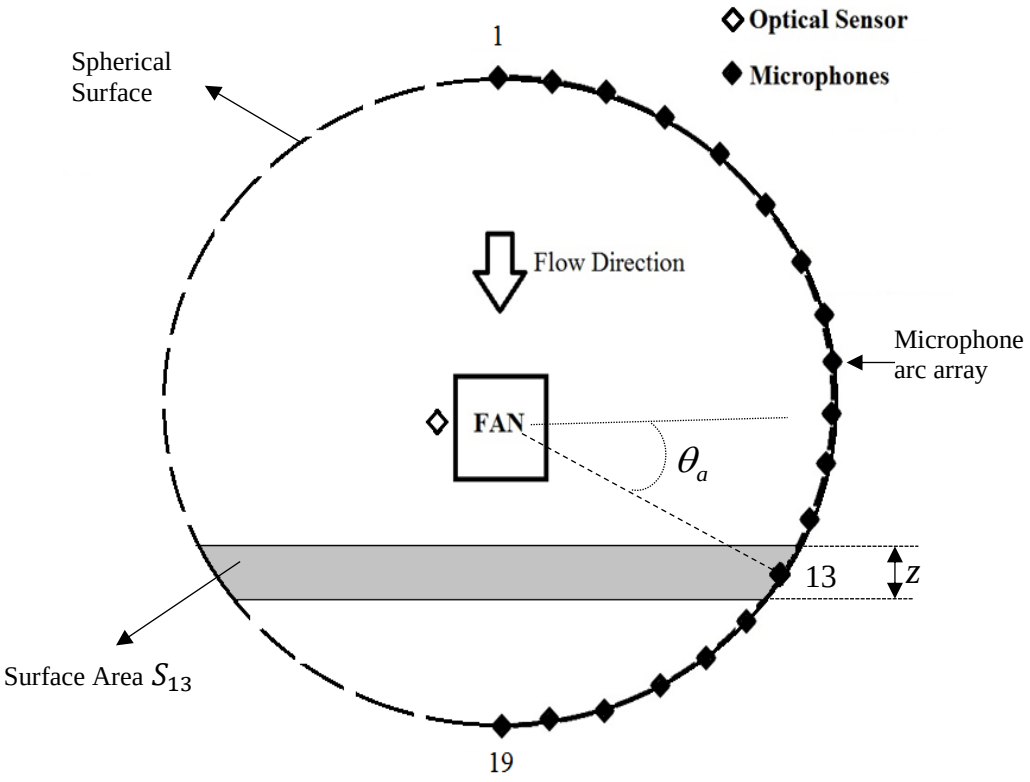

Figure 5.11: Top view of spherical surface through which that noise source's (fan) intensity propagates and surface S_{13} corresponding to the surface through which the intensity I_{13} recorded by microphone 13 propagates.

5.1.3.2 Flow measurements

The flow test apparatus consists of a Haydon LRS linear actuator, a Dwyer Series 160 Stainless Steel Pitot-static tube, and a Setra Systems 264 differential pressure transducer as shown in Figure 5.12. The Pitot-static tube has a calibration factor of 1, i.e. no calibration needed, with an accuracy of +/- 2% (Dwyer, 2016). The linear actuator allowed positioning of the Pitot-static tube with an accuracy of +/- 0.0001 in. The Pitot-static tube is mounted on the linear actuator which it is used to traverse the Pitot-static tube across the duct. The flow velocity profile measurements allowed to estimate the duct wall BL thickness and to compute the volumetric flow rate.

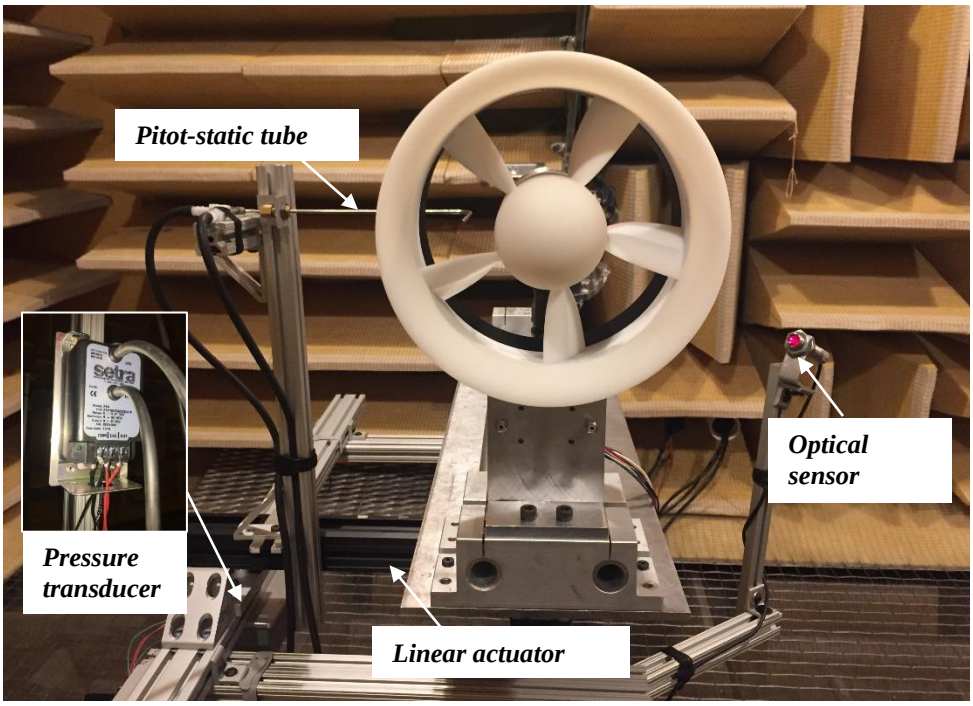

Figure 5.12: Experimental set-up of the test rig for traverse flow measurements using a pitot static tube mounted on a linear actuator. The fan speed is measured using an optical sensor.

The axial flow velocity from the fan is measured using the pitot-static tube shown in Figure 5.12. The pitot static tube measures the static pressure (P_s) and the total pressure (P_t) as shown in Figure 5.13. The pitot-static tube is connected to the differential pressure transducer that uses Bernoulli's law to measure the dynamic pressure (P_v) as

$$P_v = P_{total} - P_s \tag{5.7}$$

The voltage output ($V_{pt,out}$) of the pressure transducer is then related to the dynamic pressure using a best fit line of the calibration data provided by the manufacturer. The calibration data is shown in Figure 5.14 where the best fit line is

$$P_v = V_{pv,out} + 0.0535 \quad [In-WC] \tag{5.8}$$

Using Bernoulli's law, the axial flow velocity can be computed from the dynamic pressure as

$$v_a = \sqrt{\frac{2 \times 248.84 \times P_v}{\rho_{air}}} \quad \left[\frac{m}{s}\right] \tag{5.9}$$

where 1 inch water column is equal to 248.84 Pa. The air density is computed as

$$\rho_{room} = \frac{P_B}{R_c \times T_r} \quad \left[\frac{kg}{m^3}\right] \tag{5.10}$$

where P_B is the barometric pressure in Pascals, T_r is the room temperature in Kelvin and R_c is the specific air gas constant equal to 287.08 *J/(kg*K)*. The barometric pressure due to the 2,077 feet elevation in Blacksburg is 93,947 Pascals. The temperature (*T*) and humidity are measured using a thermometer.

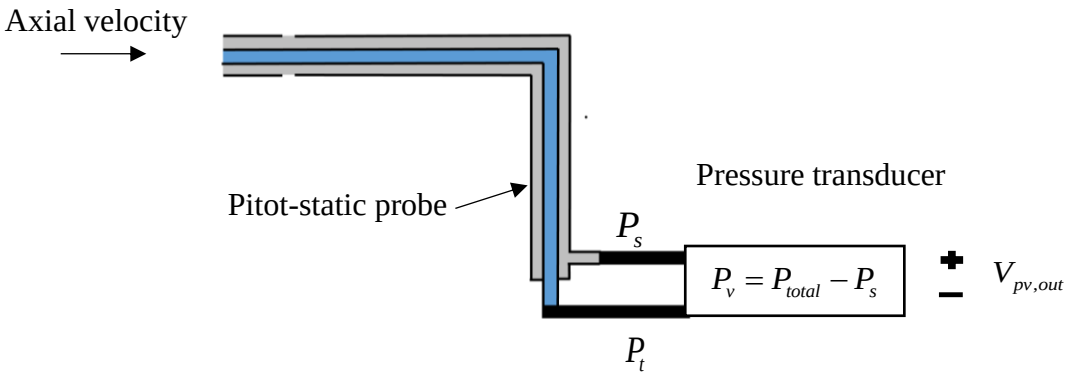

Figure 5.13: Pitot-static tube schematic for measuring the axial flow velocity using pressure transducer to generate an output voltage ($V_{pv,out}$) proportional to the flow velocity.

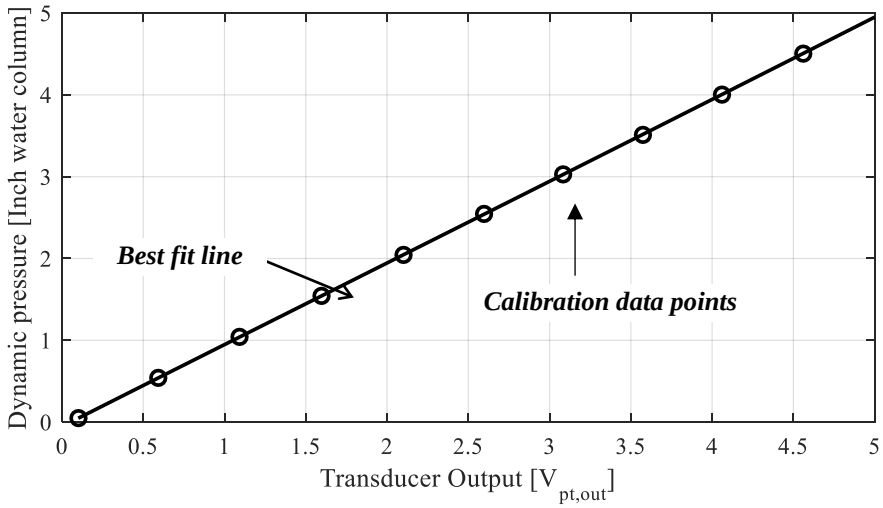

Figure 5.14: Pressure transducer calibration data showing the relationship between the measured voltage and the dynamic pressure.

It is important to note that the Pitot-static tube has its limitations and errors. The most critical error for this instrument is the flow angle error (e.g. yaw and pitch angle of the flow). If the flow stream is not parallel to the probe head, errors occur in both total and static readings. These errors cannot be corrected without taking independent reading with another type of probe (e.g. 3 directional probe). Figure 5.15 shows the errors in total and static pressure, velocity, and weight flow at various yaw and pitch angles (V_p indicates velocity calculated from total and static pressure, w indicates weight flow rate, and w_p indicates weight flow rate from total and static pressure). The errors in total and static pressure tend to compensate each other, so that the probe yields velocity and weight flow reading accurate up to 2% and up to a flow angle of 30º.

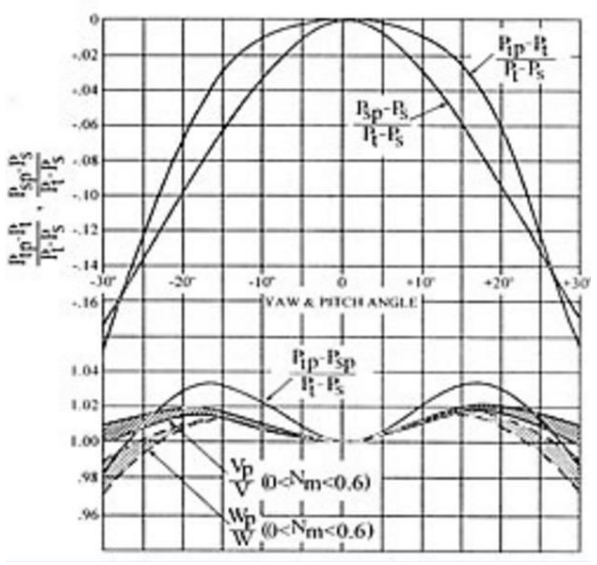

Figure 5.15: Pitot probe errors in total and static pressure at various yaw and pitch angles("Pitot Static Tube: Properties and Characteristics," 2015).

5.1.3.3 Fan speed measurements

The angular velocity of the fan was recorded using the optical sensor shown in Figure 5.16. The optical sensor used for this measurement is model ROS-P-25 by Monarch Instrument. The optical sensor, mounted as shown in Figure 5.12, emits a light beam to the rotating retro-reflective tape on the fan hub. The tachometer uses the optical sensor pulse signal to display the rotational speed in RPM as shown in Figure 5.16. The tachometer used is an AC-1B Series (Model: ACT-1B-1-0-1-310000-001) manufactured by Monarch Instruments.

(a) **(b)**

Figure 5.16: (a) Optical sensor for measuring the fan speed and **(b)** tachometer used to display the fan speed.

5.1.3.4 Fan torque and power measurements

The current in the motor is used to determine motor torque and mechanical power. The current supplied to the DB59 motor was measured using the i30s current clamp shown in Figure 5.17. The i30s current clamp uses hall effect technology to accurately measure currents with a resolution of 1 mA. The measurements are conducted by clamping the i30s current clamp around the motor drive power cable as shown in Figure 5.17. Using the output sensitivity (100mV/A) of the current probe, the measured voltage is used to compute the motor current (i_{motor}) in Amps. The motor torque constant (k_T) is then used to compute the motor torque as

$$Q = i_{motor} k_T \tag{5.11}$$

where $k_T = 0.044\,[nm/A]$ for the DB59 motor. The motor mechanical power (P_{mech}) is then computed as

$$P_{mech} = Q\Omega \tag{5.12}$$

The fan mechanical power is a metric of interest given that it is used to compare to predictions from XROTOR. To this end, the fan mechanical power is computed as the difference between the mechanical power for the fan-motor ($P_{mech,\,fan-motor}$) and the motor only ($P_{mech,motor}$) configurations.

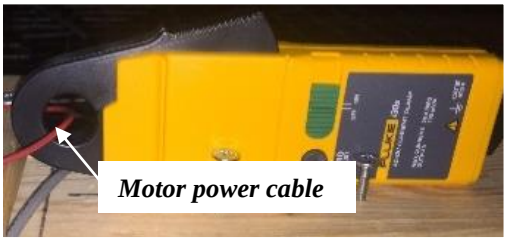

Figure 5.17: Current measurements of motor power cable using an i30s current sensor. Measurements are made by clamping the sensor around the cable.

5.2 Aerodynamic Results and Validation

This section presents experimental results of the fan mechanical power and axial flow velocity profiles to validate the aerodynamic tools used in the design process. The validation of the aerodynamic tools is conducted for the CVS, CVT2, and CVT3 fans in conjunction with the C1-Bellmouth inlet.

5.2.1 Fan Power Results

The measured mechanical power is compared to predictions for the CVS, CVT2, and CVT3 fans in Figure 5.18(a),(b), and (c), respectively. Figure 5.18(a) shows very good agreement between the measured and predicted mechanical power for the CVS fan. A small deviation from the trend is observed between 3500-4000 RPM. The increase in fan power in this range is likely due to a structural resonance of the test rig observed at ~3600 RPM. Figure 5.18(b) shows that the CVT2 fan consumes slightly less power than predicted. Figure 5.18(c) shows excellent agreement between the predictions and the experimental results for CVT3 fan.

In general, the measured power is within ~3% of the predicted values for all fans at all speeds which is excellent. To check repeatability, the power measurements were repeated for all fans and most speeds and also shown in Figure 5.18 demonstrating excellent repeatability.

(a)

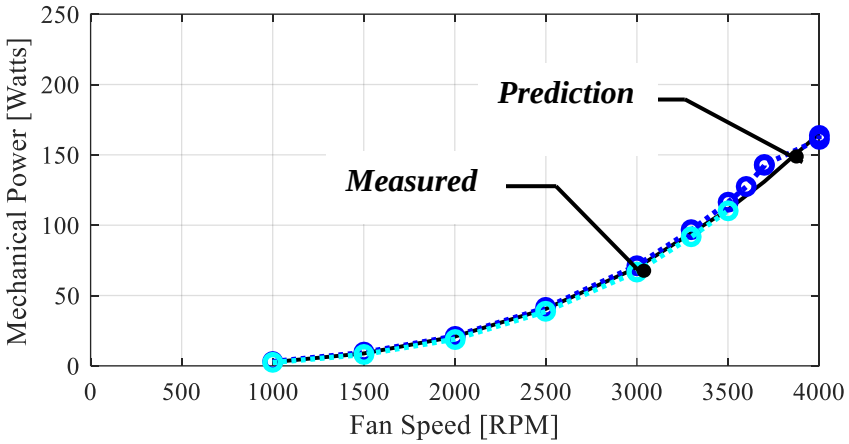

(b)

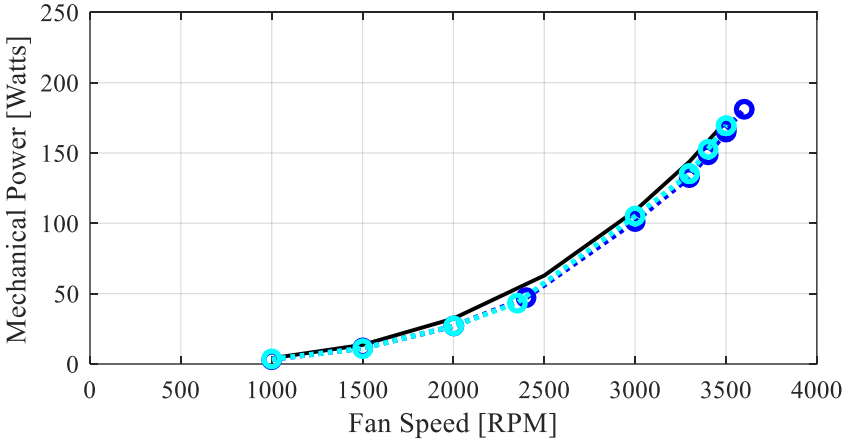

(c)

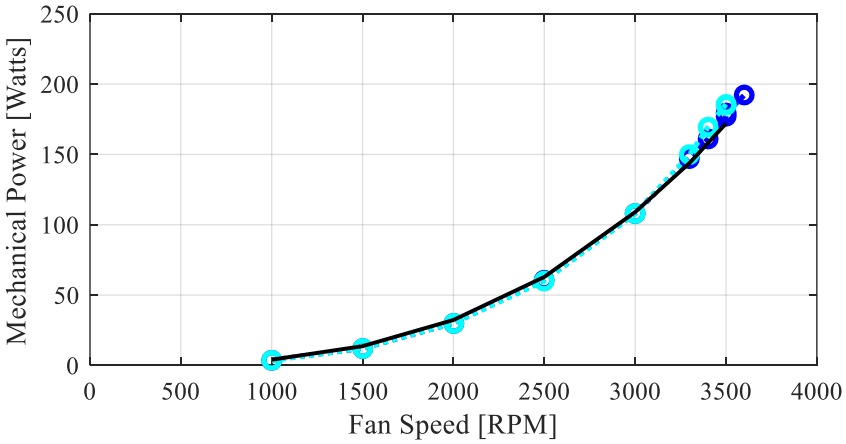

Figure 5.18: Measured mechanical power as a function of fan speed for the **(a)** CVS, **(b)** CVT2, **(c)** CVT3 fans compared to predictions from XROTOR.

5.2.2 Axial Flow Velocity Results

The measured and predicted axial velocity profile for the CVS, CVT2, and CVT3 fans is presented in Figure 5.19, Figure 5.20, and Figure 5.21, respectively. In addition, the estimated BL thickness (using DFDC) along the duct is also plotted. The BL thickness is shown as a dashed blue line over a cross section drawing of the fan. Figure 5.19 shows very good agreement of the flow profile for the CVS fan at 4000 and 3000 RPM. Additionally, Figure 5.19 shows that there is good agreement between the measured BL profile and the $1/7^{th}$ power law empirical BL profile, i.e. Equation (4.13).

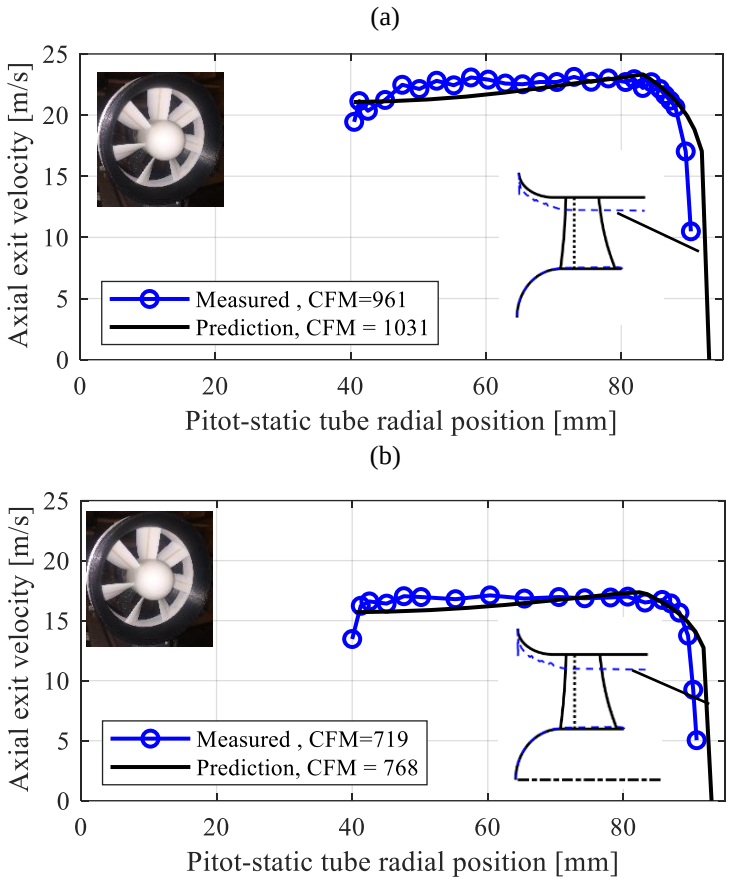

Figure 5.19: Measurements of the CVS fan axial velocity profile at **(a)** 4000 RPM, and **(b)** 3000 RPM compared to predictions from DFDC.

The axial velocity profile for the CVT2 fan is compared to predictions at design (3500 RPM) and off-design (2000 RPM) speeds in Figure 5.20(a), and (b), respectively. Here it can be observed that the measurements agree reasonably well with predictions up to ~75% of the blade span. The deviation between measurements and predictions can be potentially attributed to the increased gap size resulting from chipping of the trailing edge of the main element, i.e. the gap was not accurately fabricated.

(a)

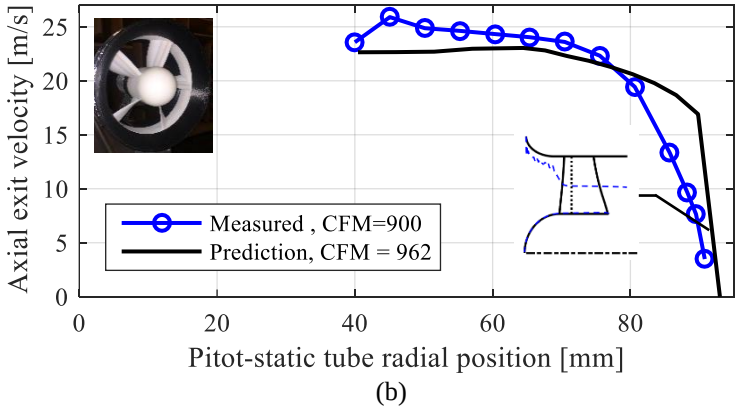

(b)

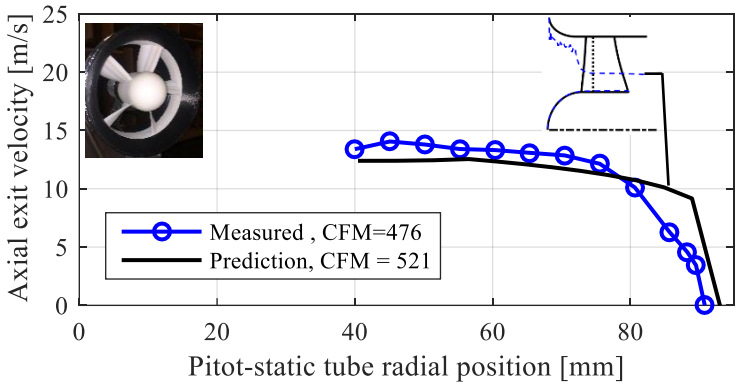

Figure 5.20: Measurements of the CVT2 fan axial velocity profile at **(a)** 3500 RPM, and **(b)** 2000 RPM compared to predictions from DFDC.

Figure 5.21 compares velocity profiles for the CVT3 fan at design (3500RPM) and off-design speeds (3000RPM and 2000RPM). As illustrated here, the measurements agree very well with the predictions. The more favorable agreement relative to the CVT2 fan is attributed to the better finish of the blades, i.e. the gap size was more accurately fabricated due to less damage at the trailing edge of the main element. The excellent agreement here indicates that the predictions of the multi-element polars using MSES/MSIS is very accurate.

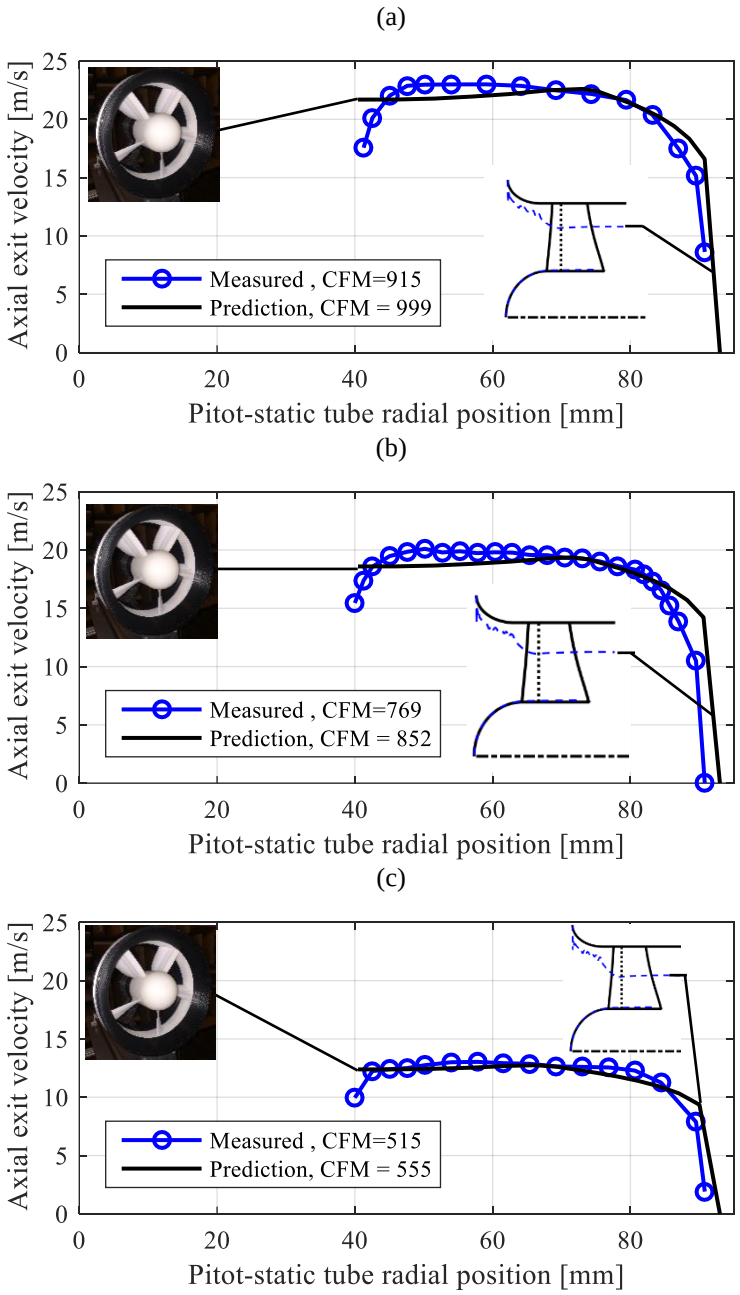

Figure 5.21: Measurements of the CVT3 fan axial velocity profile at **(a)** 3500 RPM, **(b)** 3000 RPM, and **(c)** 2000 RPM compared to predictions from DFDC.

In all cases, the predicted BL is thinner than the measured. The measured BLs are also fairly thick taking as much as 20% of the blade span. Obviously, this is because the constrain imposed in the fan design of implementing a compact inlet duct. As it will be shown later, the dominant noise source is the turbulence in the BL interacting with the blades (BLTRIN). The strength of this noise source is directly related to the thickness of the BL. Thus, additional experiments were performed

by removing the inlet duct, that should result in the largest possible BL thickness, and compared to the BL with C1-Bellmouth inlet. This experiments were carried out using the CVT3 fan. This comparison is shown in Figure 5.22. As illustrated here, a thicker BL (about 30% thicker) is formed due the removal of the inlet duct. This shows that the small C1-Bellmouth inlet duct is only marginally effective at reducing the BL thickness. As it will be shown later, the thick BL is the limiting factor to reduce fan noise since BLTRIN is the dominant noise source.

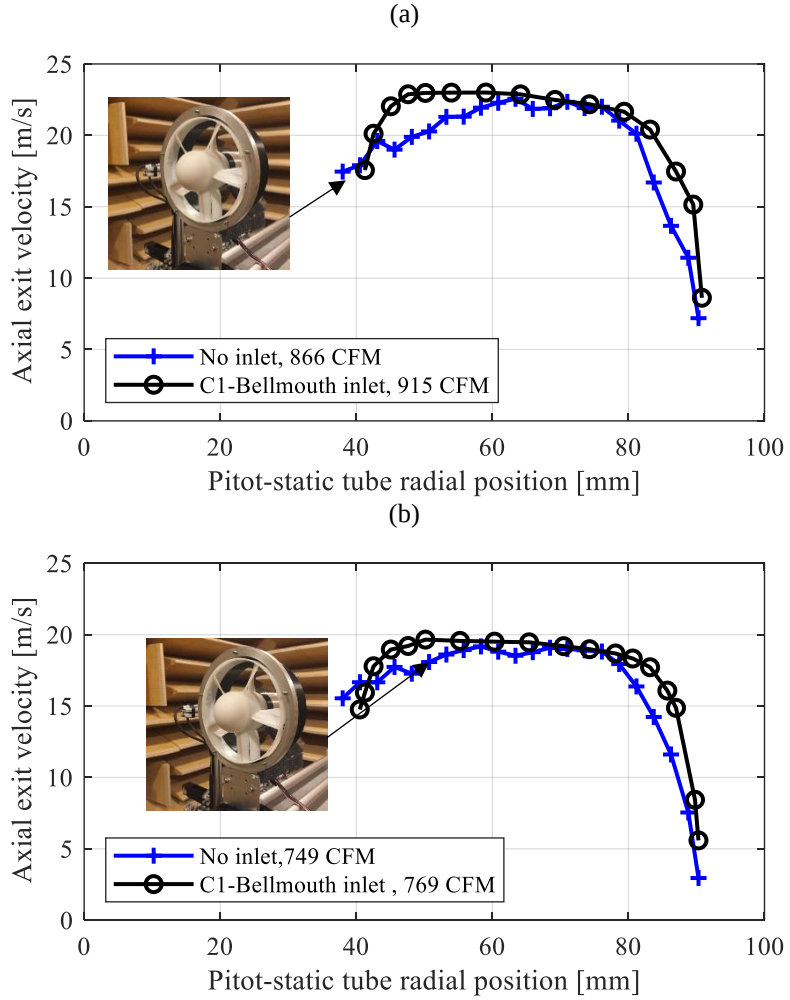

Figure 5.22: Measured axial velocity profile for the CVT3 fan at **(a)** 3500 RPM and **(b)** 3000 RPM with and without the C1-Bellmouth inlet duct.

In an attempt to reduce the BL thickness, the Q-Bellmouth inlet has been designed and tested with the CVT3 and CVS fans and the results are shown in Figure 5.23. Again for ease of comparison, the measured BLs with the C-Bellmouth are also plotted in these figures. The results show that the Q-Bellmouth has opposite effects on the BL (relative to the C_Bellmouth) depending on the fan

used. The Q-Bellmouth when used in conjunction with the CVS fan resulted in a 16% increase in the BL thickness relative to the C1-Bellmouth. On the other hand, the Q-Bellmouth with the CVT3 fan resulted in a 36% decrease in the BL thickness. Given that the dominant noise source is the BLTRIN, the correct pairing of the fan and inlet is important for minimizing fan noise. In summary, the BL thickness is nearly the same for the CVS/C1-Bellmouth and CVT3/Q-Bellmouth combinations.

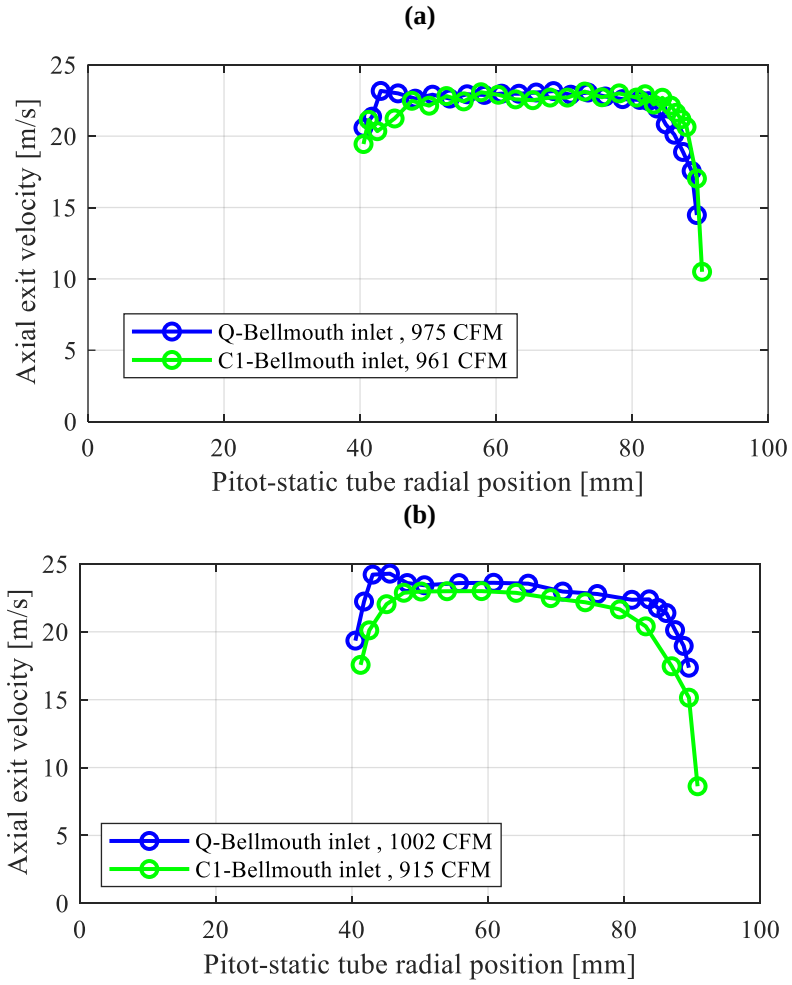

Figure 5.23: Axial velocity profile for the (a) CVS fan at 4000 RPM and (b) CVT3 fan at 3500 RPM measured with the C1-Bellmouth inlet and the Q-Bellmouth inlet.

5.3 Noise results

The aims of the acoustic measurements are twofold: (1) to compare the noise spectrum characteristics for fans designed with single and multi-element airfoils and (2) to provide noise data, in particular for tandem airfoils, for potential validation of future noise prediction tools. The fan noise is presented in the form of A-weighted sound power spectrum in narrow and 1/3rd octave bands. All narrowband results have a frequency resolution of 6.25 Hz.

The effects of tripping the BL on the fan noise is also investigated. All of the BL trips used in this work were constructed using pressure sensitive tape with a thickness of 0.19 mm and 3mm width. They were placed on the suction side of the airfoil such that the center of the tape was at the specified location. In all cases, the pressure side of the airfoil was untripped.

5.3.1 Spectral Characteristics

The measured narrowband spectrum for the CVS fan at 4000 RPM fitted with the C2-Bellmouth inlet is shown Figure 5.24. The unloaded motor only measured noise spectrum is also included in the figure. Figure 5.24 shows that the motor narrowband noise is well below CVS fan aerodynamic noise with a >10dB difference at all frequencies. The multiple tones of the motor noise at ~8kHz and higher frequencies are from the electromagnetic switching process. Consequently, the motor is not a dominant noise source at least in the unloaded condition.

The CVS fan broadband noise component is very broad with the maximum amplitude taking place around 2.5kHz and with a 10dB per octave roll off at high frequencies. The hay stack characteristics of the spectrum at high frequencies is likely due to the blades chopping elongated eddies in the BL. Similar characteristics in the measured noise spectrum for rotor only fans have been observed by other authors (Moreau et al., 2006; Roger et al., 2006). There are also many tonal components in the spectrum. The fan BPF tone (~470 Hz) and the first 3 harmonics are clearly identified in the figure. The other tones are associated to loaded motor noise. The small tone at ~ 130 Hz corresponds to the 2nd shaft order (SO) most likely produced by unbalance of the system exciting the rig. Additionally, three are 3 closely spaced tones at ~1.2kHz. Given that the spacing between these tones is 65 Hz, they are likely associated to the motor rather than the fan. Finally, there are other tones, only a few dBs above the broadband, at around 8kHz that are the

electromagnetic switching related tones. It is important to note that all the tones contribute only marginally to the overall sound power level of 77.7 dBA.

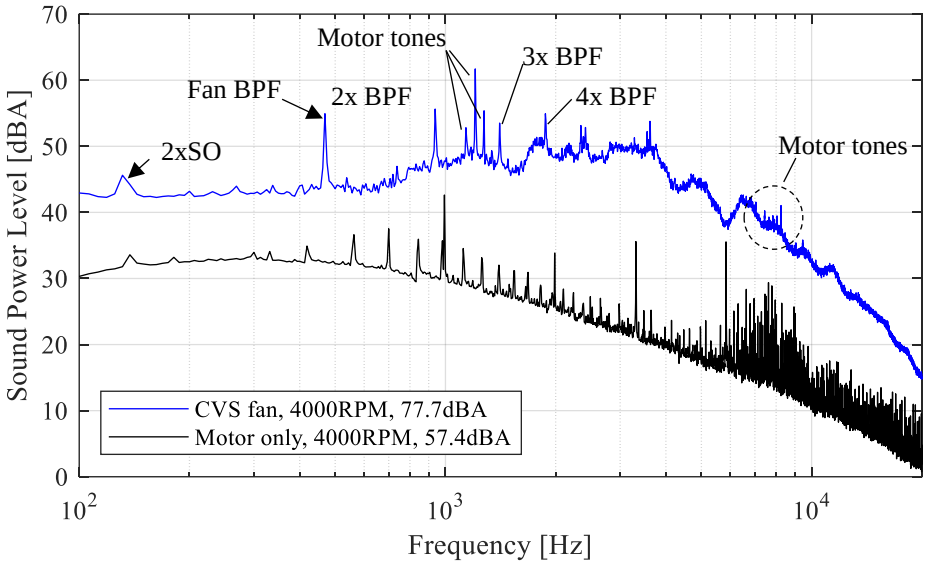

Figure 5.24: Measured fan noise spectrum in narrowband for the CVS fan and BLDC motor at 4000 RPM (C2-Bellmouth inlet).

To stablish the repeatability of the noise results, the noise for the CVS fan at 3300 RPM was measured several days apart and presented in Figure 5.25. The spectrums matched well for frequencies higher than ~600 Hz with a small decrease in the motor tones around 8kHz. Below ~600 Hz there is a small difference that increases from ~0.5 up to 3 dB at 200 Hz. The decrease in motor tones at high frequencies and the increase in low frequency broadband noise cancel each other our resulting in repeatability of ~0.2 dB. The difference in low frequency noise and tones is attributed to small changes in the test set-up over several days, e.g. rig was taken apart and reassembled between the two tests.

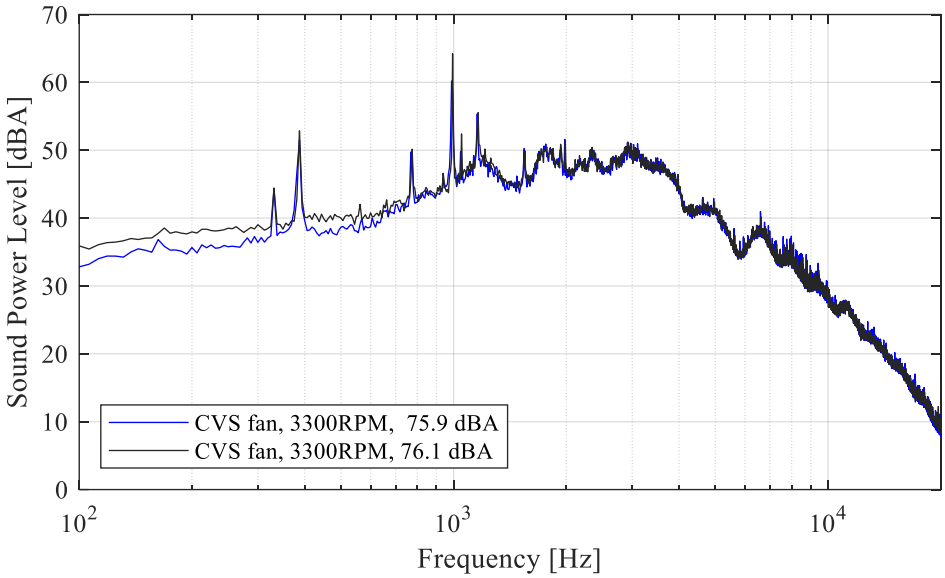

Figure 5.25: Repeated measured fan noise spectrum in narrowband for the CVS fan at 4000 RPM (C2-Bellmouth inlet).

The narrowband sound power level spectrum of the CVS fan (4000 RPM) is compared to the CVT3 fan (3500 RPM) in Figure 5.26. It is evident here that the CVT3 fan results in a decrease in the BPF tones, e.g. 5 and 7 dB at the BPF and 2BPF, respectively. This is likely a results of several factor. Firstly, the CVT3 operates at a lower tip speed leading to reduction of both the thickness and loading noise components. Secondly, the thickness noise component of the CVT3 fan is further reduced due to the thinner airfoils. Thirdly, the A-weighting also contributes to the reduction as the frequency of the tones is lowered. It is also clear in Figure 5.26 that the CVT3 fan results in a small increase in broadband noise levels at high frequencies (>4000 kHz) and a decrease at low frequencies (< 500 Hz). These two broadband effects cancel each other resulting in virtually the same overall sound power level.

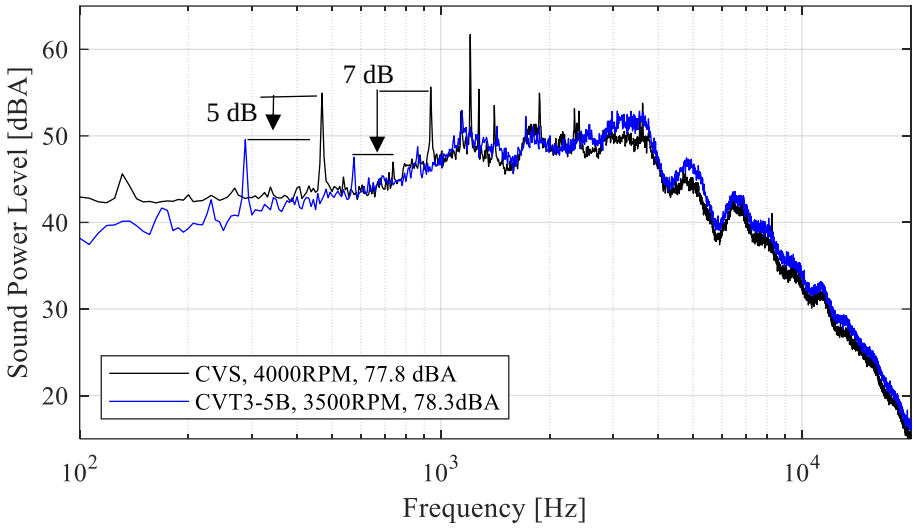

Figure 5.26: Measured fan noise spectrum in narrowband for the CVS and CVT3 fan (tripped at x1/c1=0.25) at their design speeds of 4000 and 3500 RPM, respectively (C2-Bellmouth inlet).

The CVT3 fan noise in one-third octave bands was measured for different fan speeds as shown in Figure 5.27. To check the scaling characteristics, the amplitude of the spectrums in Figure 5.27 were scaled with the 5^{th} and 6^{th} power of the tip speed (or RPM). Figure 5.28(a) shows that the dominant part of the spectrum (1 to 7 kHz) scales very well with the 5^{th} power. The 6^{th} power scaling works better at higher frequencies (>7 kHz) as shown in Figure 5.28(b). Based on the predictive tools and consistent with the literature, the computed scaling powers for the RSN and BLTRIN sources are 5.5 and 6.0, respectively. These results are consistent with the scaling characteristics shown in Figure 5.28(a) and (b) confirming that the dominant noise sources are aerodynamic in nature. Unfortunately, these scaling studies are not sufficient to determine the relative contribution between the RSN and BLTRIN sources.

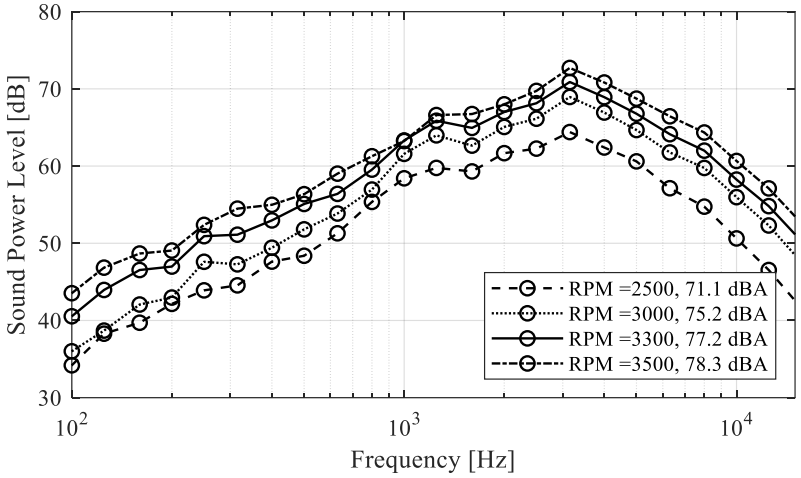

Figure 5.27: Fan noise spectrum in one-third octave bands measured at different fan speeds for the CVT3 fan (C2-Bellmouth inlet).

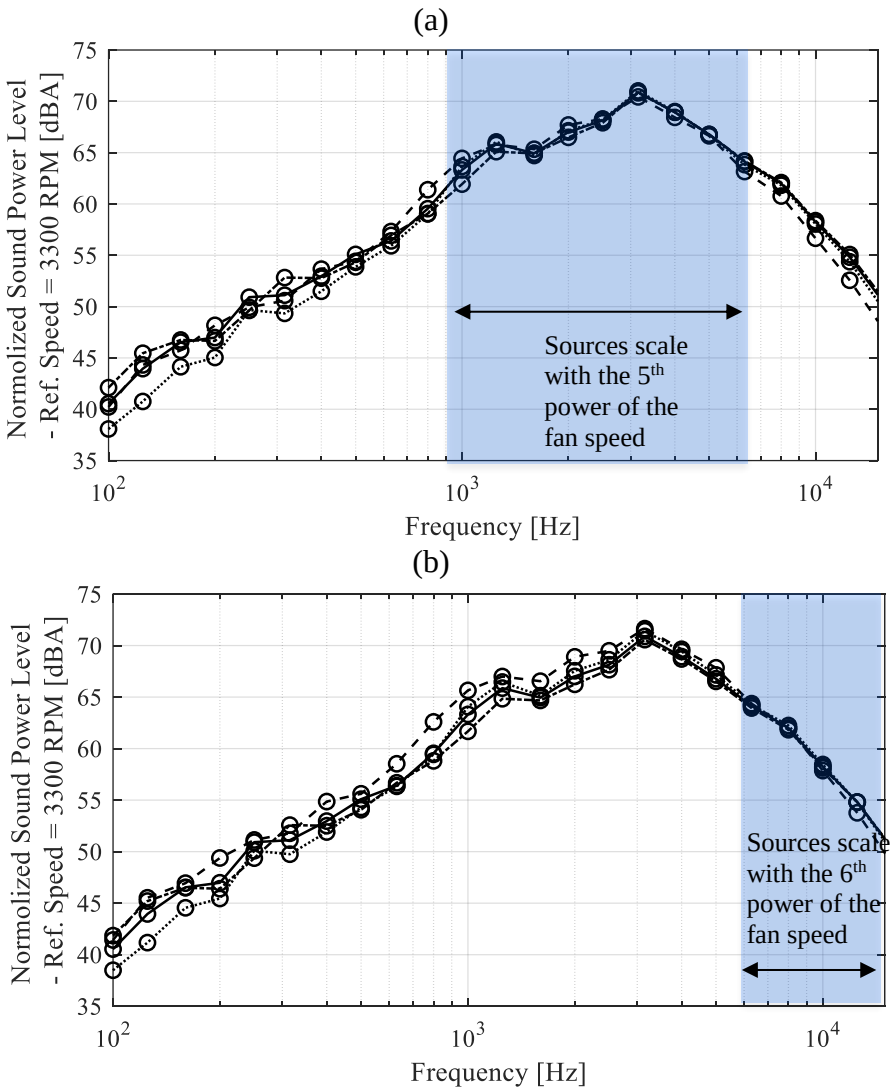

Figure 5.28: Normalized sound power level spectrum with the **(a)** 5th power, and **(b)** 6th power of the fan speed (CVT3 fan with C2-Bellmouth inlet).

5.3.2 Noise Source Identification

The aim of this section is to find the dominant broadband noise sources both through predictions and experimental data.

The first study to gain insight into the dominant broadband noise sources was based on the prediction tools for the RSN and BLTRIN sources discussed in Section 3.3. These tools were used to predict the noise for the CVS fan. In these calculations, all inputs needed for the codes were predicted, i.e. no experimental data was used. The computation of the total noise was by incoherently adding these two sources.

The predicted RSN, BLTRIN, and total sound power level spectrum has been compared to the measured (total) sound power level in one third octave bands. The comparison is carried out at the design speed (4000 RPM) and off design speeds (3700 and 3000 RPM) and shown in Figure 5.29. As illustrated here, fairly good agreement between the predictions and measurements is observed. It is evident here that the BLTRIN is the dominant source for the CVS fan for most frequencies.

(a)

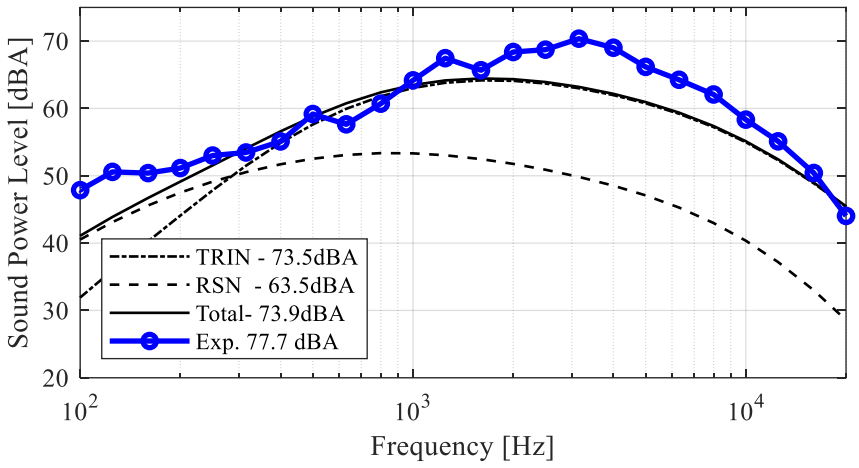

(b)

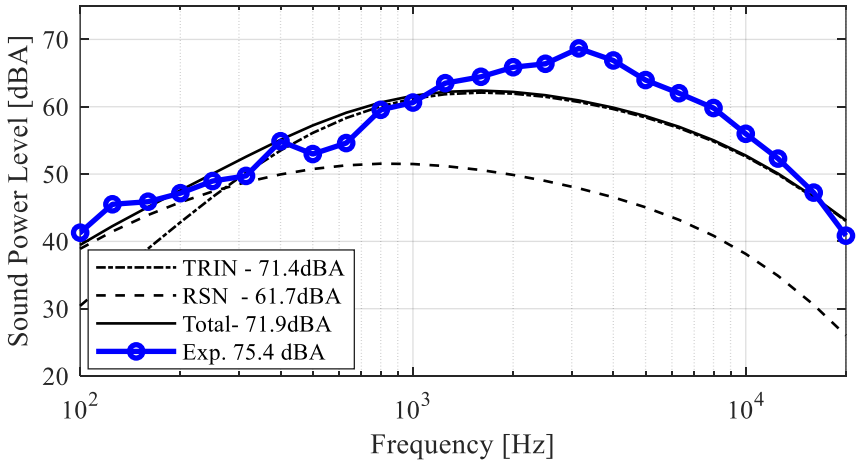

(c)

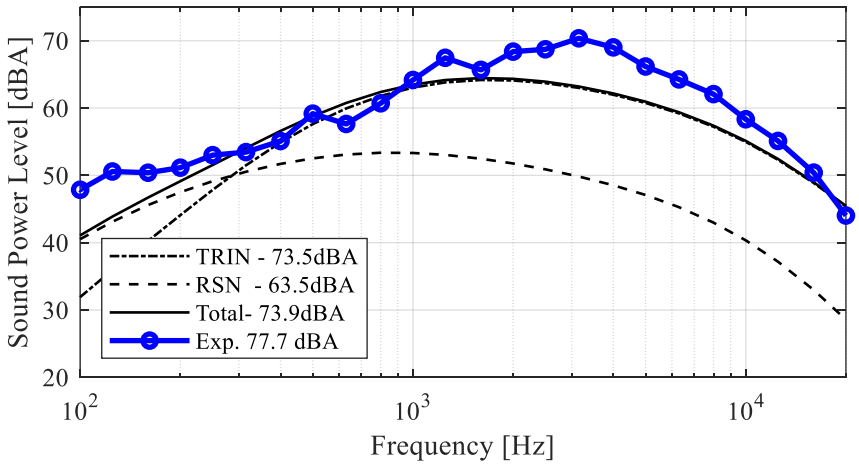

Figure 5.29: Predicted sound power level spectrum in one third octave bands implementing the RSN and TRIN noise models. The predictions are tested against experimental results for the CVS fan at **(a)** 3000 RPM, **(b)** 3700 RPM, and **(c)** 4000 RPM.

The next set of studies are based on experiments. The first experimental study focuses on assessing if the strut was a broadband noise source, e.g. primarily if turbulence from the fan interacting with the strut is a significant noise source. Several treatments of the strut were implemented to reduce the rotor-strut interaction noise. The treatments involved a fairing to aerodynamically shape the strut leading edge, covering the strut with a soft foam, Mylar serrations, and combinations of these approaches. The best results were observed with the aerodynamically shaped strut covered with foam. Figure 5.30 compares the noise spectrum with and without treatment. As shown in this figure, the only discernable difference is in the fan tones. The tone at the fan BPF and harmonics are reduced by a few dBs. However, the effect to the broadband noise and overall sound power level are negligible. This can be attributed to the forward axial swept strut which has clear acoustical advantages as documented by several authors (Dalton et al., 1999; Envia and Nallasamy, 1999; HM Schulten, 1997). Therefore, the strut clearly is not a significant noise source.

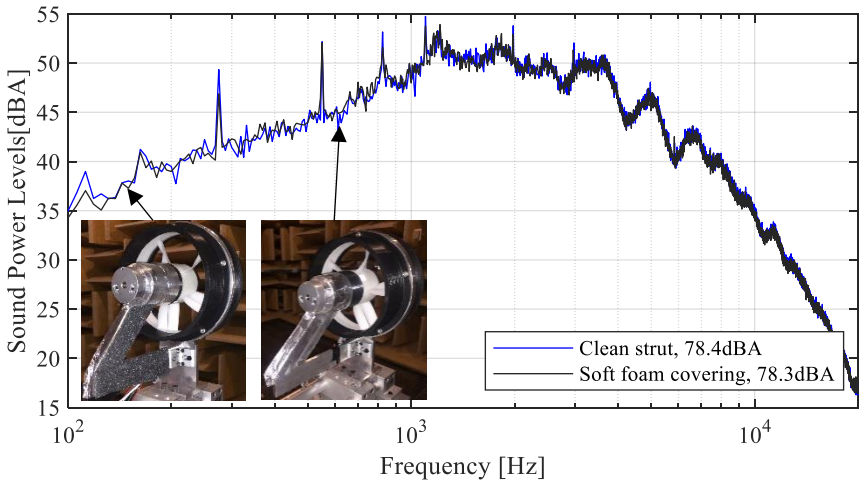

Figure 5.30: Effect of the foam covering strut on the measured sound power level spectrum for the CVT3 at 3300 RPM fitted with the C1-Bellmouth inlet.

As described in section 5.3.1, the dominant source of noise in axial fans is generated from the interaction of the blade with the turbulence in the duct wall BL. In addition, ingestion of turbulence from inside the chamber could also be a noise source. The BL turbulence intensity is highest near the wall as shown in Figure 3.7 (inner part of the BL). Consequently, the turbulence intensity is largely influenced by the inlet surface roughness. Thus, the CVS and CVT3 fans were tested with both the C1 and C2-Bellmouth inlets. These inlets have surface finishes that consist of closely spaced circumferential grooves resulting from the 3D printing process. The approximate height of

the grooves is 0.2 and 0.001 mm for the C1 and C2-Bellmouth inlets, respectively. Thus, the C1-Bellmouth surface is significantly rougher than the C2-Bellmouth and thus conducive to produce an increase in BLTRIN. Figure 5.31(a) and (b) show the 1/3rd octave band noise spectrums for the CVS fan at 4000 RPM and CVT3 fan at 3500 RPM, respectively, with both C-Bellmouth inlets. The smooth C2-Bellmouth inlet resulted in a 2.1 and 1.2 dB overall noise reduction for the CVS and CVT3 fans, respectively, relative to the C1-Bellmouth inlet. For the CVS fan, the reduction in the spectrum takes place in the 1 to 8 kHz frequency range. This demonstrates that the BLTRIN BL is the dominant source of noise in this frequency range as predicted (see Figure 5.29). This result also suggests that the recirculating atmospheric turbulence inside the anechoic chamber is not a dominant source of noise, at least in the 1 to 8 kHz frequency range. For the CVT3 fan in Figure 5.31(b), the reduction in levels when using the smooth C2-Bellmouth inlet is less pronounced and over a smaller frequency range. The results for frequencies > 10 kHz remain unchanged for both fans. This effect can have two possible explanations. The first one is that the RSN source dominates at these frequencies while the second one is that the roughness of the C1-Bellmouth doesn't increase the intensity of the small scale turbulence responsible for the noise at these higher frequencies. It is also important to note that the RSN predictions, with all the limitations discussed in Section 3.3, does not indicate that this source dominates at high frequencies.

At low frequencies (≤400 Hz), the rough C2-Bellmouth reduced the noise levels for the CVS fan while the levels remained virtually unchanged for the CVT3 fan. It is likely that these results are due to poor repeatability given that the CVS tests were performed months apart while the tests for the CVT3 fan were performed on the same day (back-to-back) with exactly the same set up. Figure 5.25 shows that this frequency range (<600 Hz) has poor repeatability.

(a)

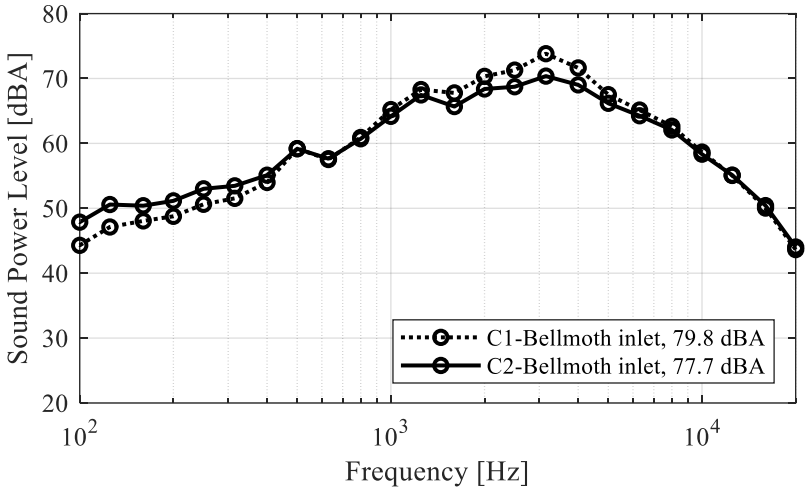

(b)

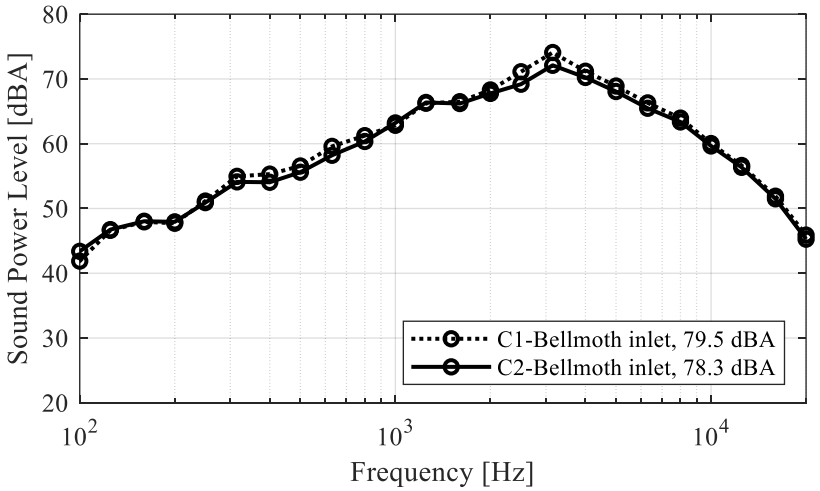

Figure 5.31: Measured sound power level spectrum in one-third octave bands for **(a)** CVS fan (4000 RPM) and **(b)** CVT3 fan (3500 RPM) fitted with the C1-Bellmouth and the C2-Bellmouth inlets (untripped fan).

The next set of experiments were performed to investigate the effect of tripping the blades on noise. This is important given the separation bubble observed (Chapter 4) in the MSES aerodynamic results (polars, pressure distribution, etc.) for the tandem airfoil used in the CVT3 fan, primarily in the rear airfoil (see Figure 4.32 through Figure 4.34). It was observed in Chapter 4 that a separation bubble is not expected for the single element airfoil at the chord Reynolds number for the fan design (70-120k). The presence of a separation bubble can generate Tollmien–Schlichting instability waves. These waves are generated by a BL instability point on surface of

the airfoil and travel down to the trailing edge where scattering generates acoustic waves. The acoustic waves then travel back to the point of instability creating a feedback loop. If proper phase occurs, amplification of the sound occurs (Jianu et al., 2012; Longhouse, 1977). The roll-up vortices observed in separation bubbles can also induce unsteady surface pressure fluctuations as they convect past the trailing edge resulting in radiated sound waves as described by classical trailing edge noise (Kurelek et al., 2016).

Thus, experiments were performed by tripping the fans with the 0.19 mm tape. The trip extended the full blade and in all cases the smooth C2-Bellmouth inlet was used. Figure 5.32(a) shows the result of tripping the CVS fan operating at 4000 RPM. As observed, tripping the CVS fan did increase the noise levels at the low frequencies (< 400 Hz) and remains unchanged for the rest of the spectrum. The unchanged levels at high frequency is easily explained by the fact that the BLTRIN dominates here and it will not be affected by the trip. On the other hand, the increase at low frequency could be due to the repeatability issues shown in Figure 5.25. In summary, it is likely that the CVS fan doesn't experience a separation bubble and tripping is not advisable.

On the other hand, the chord based Reynolds number decreases by nearly half for the CVT fans due to the smaller chord of the individual airfoils. Consequently, they are more susceptible to the generation of a separation bubble as described in Chapter 4. Several preliminary tests were conducted to investigate the effect of the trip tape thickness and location. To this end, the trip was tested in the main, rear, and both airfoils. Multiple trip locations and thicknesses were tested. The main observation was that tripping the front element upstream of the separation bubble with the thinnest trip results in the highest noise reduction. This agrees well with results from Chapter 4 which indicated that the chord wise location of the trip is not important to eliminate the laminar separation bubble as long as it is located upstream of the bubble. Thus, the results here corresponds to the main airfoil tripped at 20% of the chord c_1 from the leading edge.

Figure 5.32(b) shows the results for the CVT3 fan at 3500 RPM. It is observed that tripping the CVT3 fan results in a noticeable decrease in noise level at frequencies > 4kHz. The reduction could obviously be explained by the reduction in drag associated with tripping the airfoil (See Figure 4.34) which directly relates to fan noise. Unlike for the CVS fan, this implies that RSN is

likely dominant in the high frequency range for the CVT3 fan. This is also consistent with the fact that the tandem airfoil has 2 trailing edges that can radiate at higher frequencies.

(a)

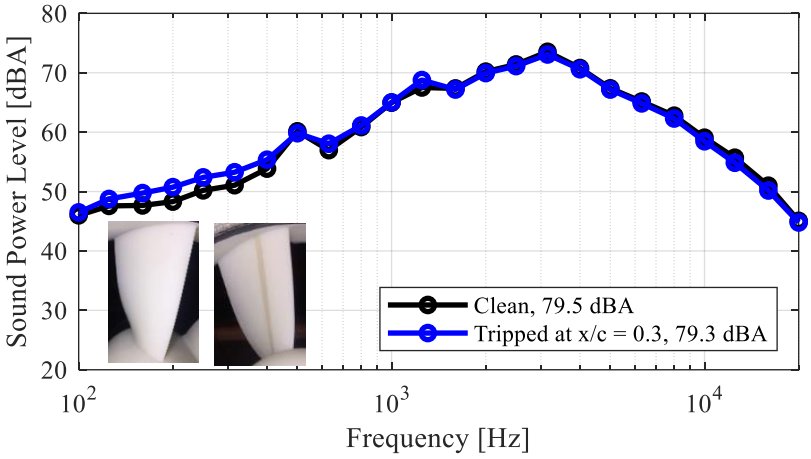

(b)

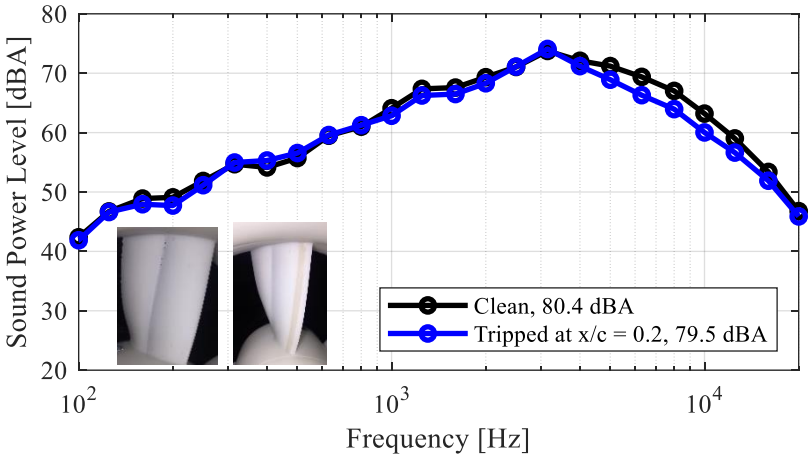

Figure 5.32: Effect of tripping the airfoil BL on the sound power level for the **(a)** CVS (4000 RPM) and **(b)** CVT3 (3500 RPM) fans (C2-Bellmouth inlet).

5.4 Overall Comparison of CVS and CVT3 Fans

In this section, an overall assessment of the performance of the two fans is presented. The CVS and CVT3 fans have been designed to generate the same volumetric flow rate with the same geometric constraints. The comparison was carried out for the operating range of the fans and the main metrics of interest are the overall sound power level, aerodynamic efficiency, and volumetric flow rate.

In this comparison, the CVS and CVT3 fans were operated in conjunction with the C2-Bellmouth and the Q-Bellmouth inlet, respectively. The reason is that the resulting BL is nearly the same for these two fan-inlet combinations. To prove this point, Figure 5.33 shows the measured velocity profiles for both cases. This figure clearly shows that the BL thickness is very similar.

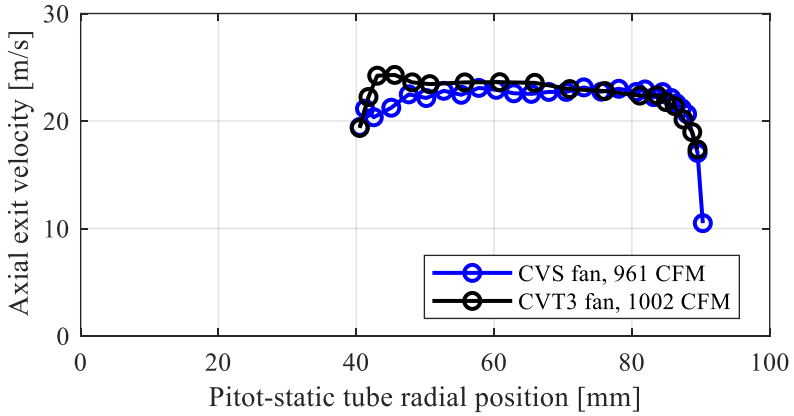

Figure 5.33: Measured axial velocity profile for the CVS (4000 RPM) and CVT3 (3500 RPM) fan in conjunction with the C and Q-Bellmouth inlets, respectively.

The overall sound power level as a function of the volumetric flow rate is presented in Figure 5.34. It is evident here that the CVS and CVT3 fans generate nearly the same noise levels near the design volumetric flow rate of 1000 CFM. The CVS fan is quieter by about 1 dB than the CVT3 fan for the mid operating range. However, the CVT3 fan outperforms the CVS fan in the lower operating range.

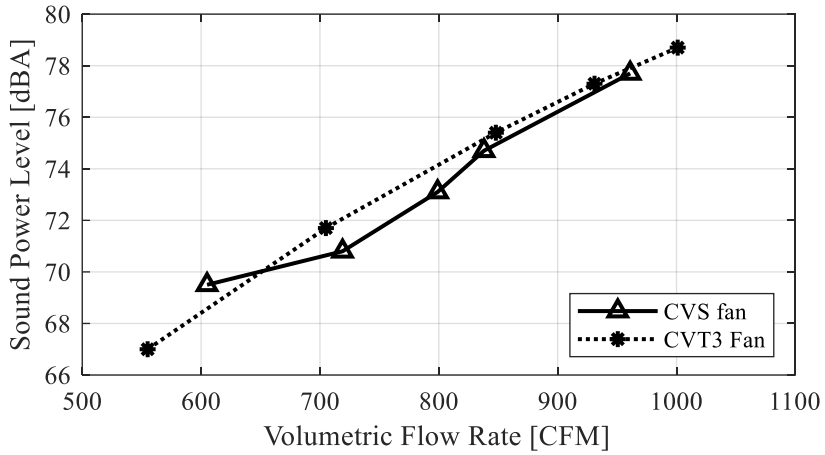

Figure 5.34: Measured sound power level as a function of the volumetric flow rate for the CVS and CVT3 fans.

The results from the previous section suggest that the BLTRIN is the loudest noise source for the dominant part of the spectrum (1 to 8 kHz) for both fans which it is easily explained by the thick BL present in both fans. The RSN appears to contribute to the CVS fan noise only in the low frequencies (< 400 Hz). On the other hand, the RSN is observed to contribute in the high frequency part of the spectrum (> 6 kHz) for the CVT3 fan, likely at similar levels as the BLTRIN source.

The mechanical efficiency of the CVS and the CVT3 fan has been computed using measured data and Equation (2.4). Figure 5.35 shows the mechanical efficiency as a function of volumetric flow rate. It is illustrated here that the CVT3 fan can generate a higher volumetric flow rate at a higher efficiency. Additionally, the CVT3 outperforms the CVS fan by up to 6% in the volumetric flow rate range of 700 to 900 CFM.

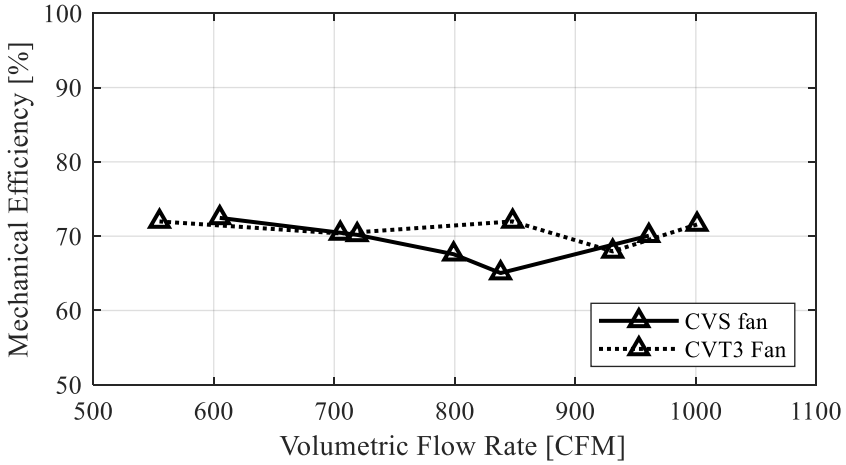

Figure 5.35: Measured mechanical efficiency as a function of the flow rate for the CVS and CVT3 fans.

Figure 5.36 shows the measured mechanical power as a function of the volumetric flow rate. The CVT3 shows a slight decrease in required power due to the higher blade profile efficiency of the blades. This is illustrated in Figure 5.37 that shows the XROTOR predicted blade profile efficiency distribution for the two fans. The CVT3 fan blades clearly have a higher profile efficiency, primarily in the out section of the blade that does most of the aerodynamic work. To further corroborate this improve in efficiency, the predicted lift to drag ratio distribution along the blade is shown in Figure 5.38. Once again, the CVT3 fan clearly outperforms the CVS fan.

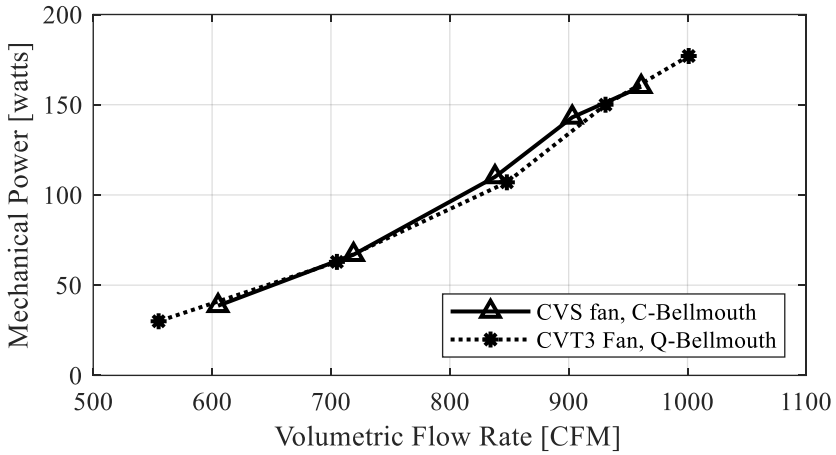

Figure 5.36: Measured Mechanical Power as a function of the volumetric flow rate for the CVS and CVT3 fans.

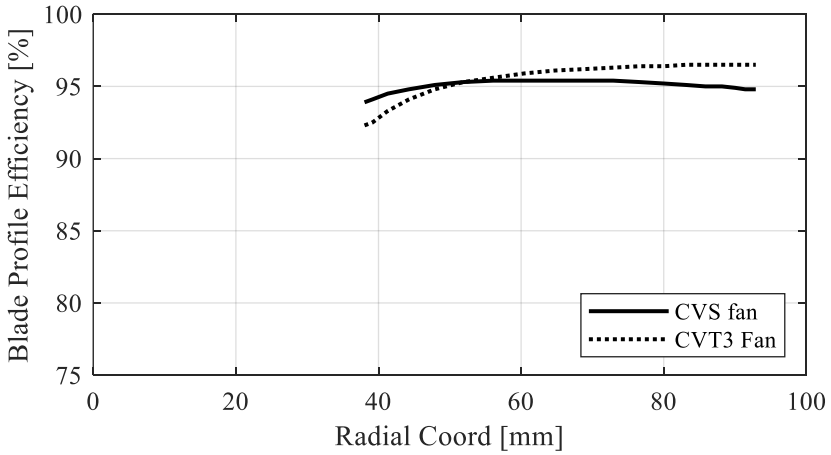

Figure 5.37: Predicted blade profile efficiency for the CVS (4000 RPM) and CVT3 (3500 RPM) fans.

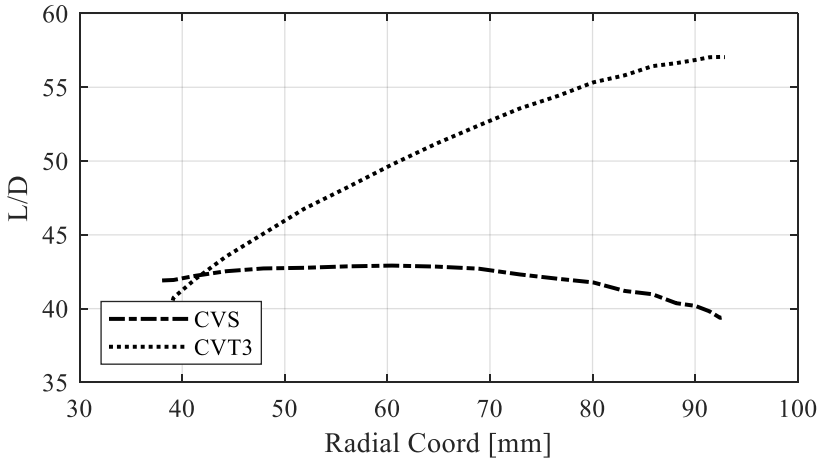

Figure 5.38: Predicted blade profile lift-to-drag ratio for the CVS (4000 RPM) and CVT3 (3500 RPM) fans.

In summary, this comparison shows that the CVT3 fan using multi-element technology outperforms aerodynamically the conventional single element airfoil CVS fan. It is also fair to say that the acoustic benefit is rather marginal in terms of overall sound levels. It is also obvious that a reduction in the BL thickness is the clear pathway forward to get additional noise reduction for both types of fans.

CHAPTER 6

6 Multi-fan design

The review of data pertaining to noise levels of commercial fans highlight the need for quiet compact fans with a high volumetric flow rate. To this end, this chapter describes a practical implementation of the CVT3 fan design into an advanced fan array system. The mechanical design is innovative given that a multi-fan unit has not been previously designed for commercial ventilation fans in the open literature.

The advanced fan array system designed is herein referred to as the VTFA (**V**irginia **T**ech **F**an **A**rray) unit. The design of the VTFA unit is presented in Section 6.1. VTFA unit has been experimentally tested against a baseline commercial fan. The commercial fan selected as the baseline fan is the Cincinnati model 24631 manufactured by Cincinnati Fan & Ventilator Co shown in Figure 6.1. The Cincinnati fan has 6 blades and a rotor diameter of 24 inches (0.610 meters). The Cincinnati fan was chosen because its sound power level falls on the trend line of the data collected for commercial ventilation fans in Figure 2.5. Therefore, it represents a typical commercial fan. To this end, the Cincinnati baseline fan was fully characterized by measurements of the radiated noise and flow profile identical to the ones for the VTFA unit as described in section 6.2. Thus, the results can be compared directly.

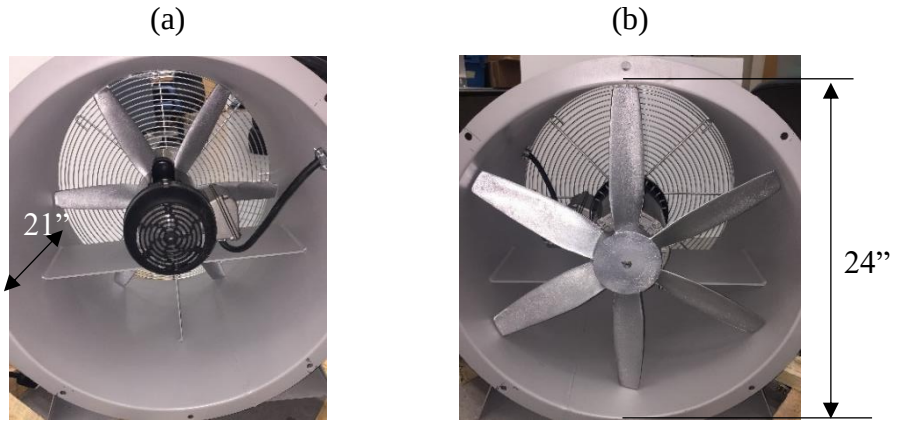

Figure 6.1: Baseline Cincinnati fan model 24631 (a) inlet, and (b) outlet with the screens removed.

6.1 VTFA Unit Design and Fabrication

The VTFA unit has been designed with seven CVT3 fans connected in parallel. Figure 6.2 shows the CAD drawing of the VTFA unit. The seven fans are mounted to the motors using the same mechanism used in the design of the single fan test rig, i.e. same components shown in Figure 5.4. The fan-motor assemblies are then mounted to an aluminum baseplate fixed inside of a cylindrical duct. The VTFA incorporates an inlet bell-mouth to clean the inflow and minimize inflow turbulence due to the sharp leading edge of the duct. Additionally, all seven fans have individual bellmouths (labeled as inlet channel) with the same geometry used for testing the single fan (C-Bellmouth inlet). The inside diameter of the VTFA unit is 0.68 m (27 inches) while the length is 0.4 m (16 inches).

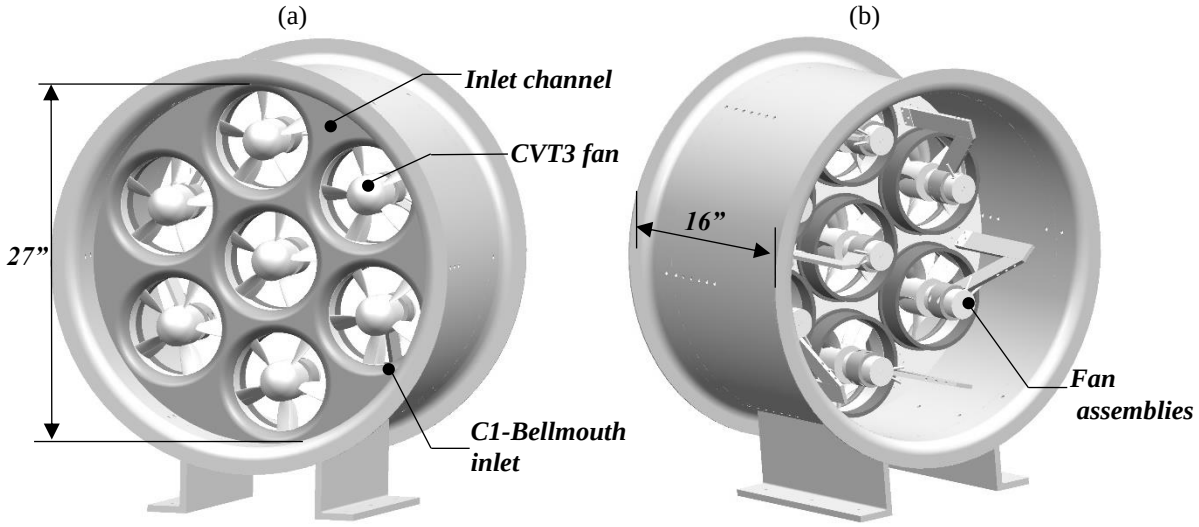

Figure 6.2: VTFA mechanical design consisting of 7 CVT3 fans and an inlet channel composed of individual C1-Bellmouth inlets for each individual fan.

The inlet channel and fans were fabricated using standard ABS and opaque white SLA 3D printing material, respectively. A multi-axis DMC-4070 controller is used to drive all of the fans. The controller is powered by an AC-DC Power Supply. Figure 6.3 shows a front view of the VTFA unit and components. The rear view of the VTFA unit is shown in Figure 6.4. As illustrated here, obstructions downstream of the fans are minimized, i.e. motor power cables are taped downstream of the fan struts. Figure 6.4 also shows that the soft foam has been added to the motor struts as they help reduce fan-strut interaction noise. The motor encoder shown in Figure 6.4 is used to drive the motors using the DCM-4070 controller at a given speed.

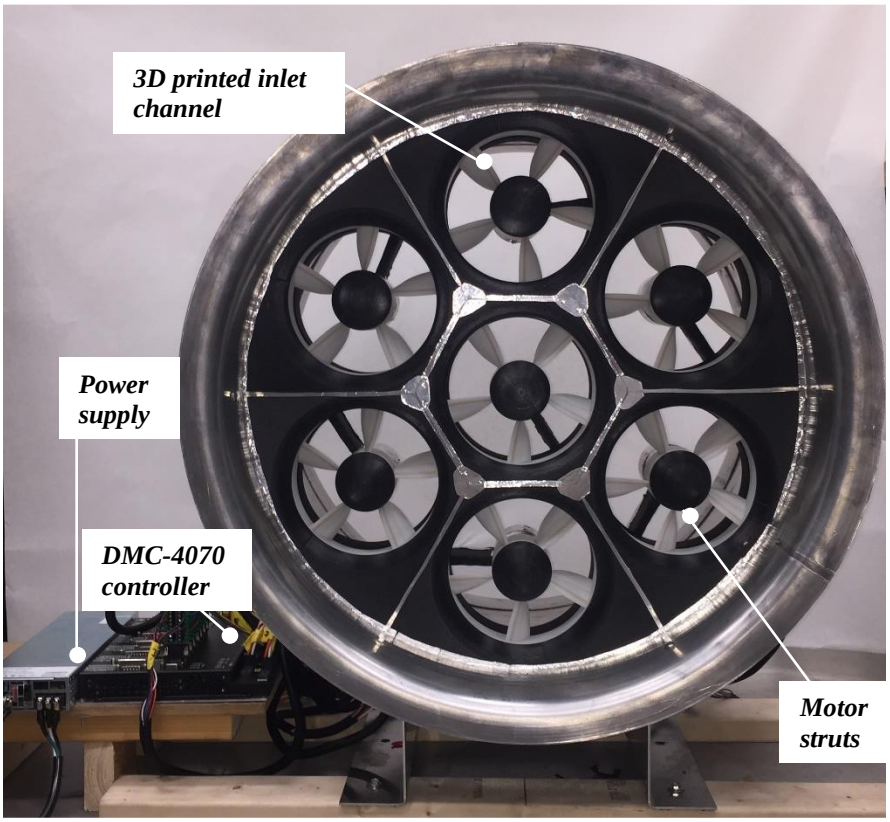

Figure 6.3: Front view of the VTFA unit prototype. The fans are operated by individual DB59 BLDC motors and controlled using a DMC-4070 multi axis controller.

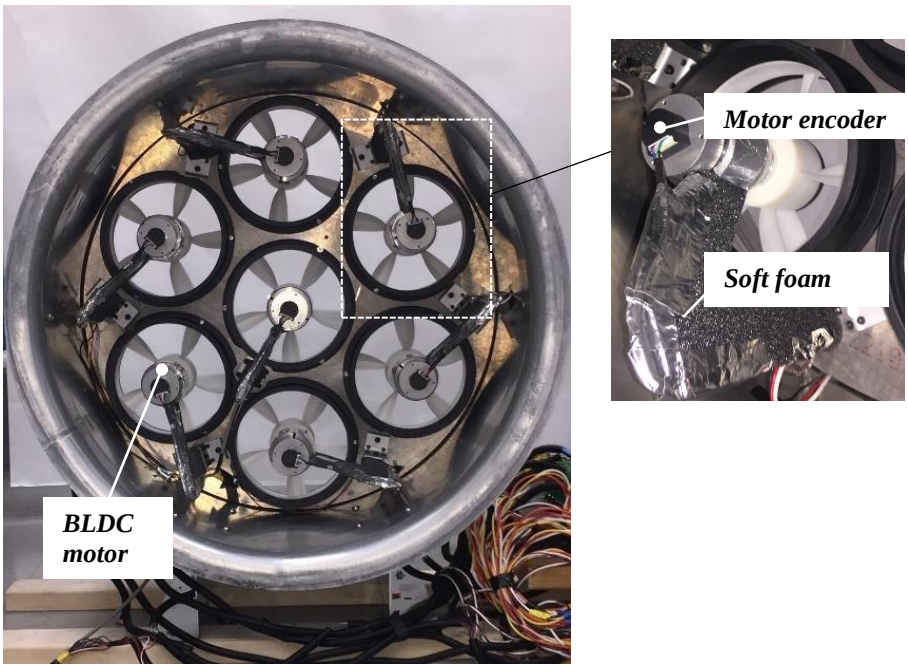

Figure 6.4: Read view of the VTFA unit prototype highlighting the soft foam added to the struts to reduce rotor-strut interaction noise.

6.2 VTFA Experiments

This section presents the experimental investigation of the VTFA unit and baseline fan. To this end, the experimental set-up and instrumentation used to characterize the acoustic and aerodynamic performance are described.

6.2.1 Experimental set up

Noise measurements of the VTFA unit and baseline fan were performed outdoors due to the large size of the units. Figure 6.5 shows the VTFA unit under test. To reduce reflections a 3.5 feet tall and 8.5 ft wide wall of acoustic wedges was built on both sides of the fan. The measurements were made with an arc array of 19 microphones evenly distributed along its circumference.

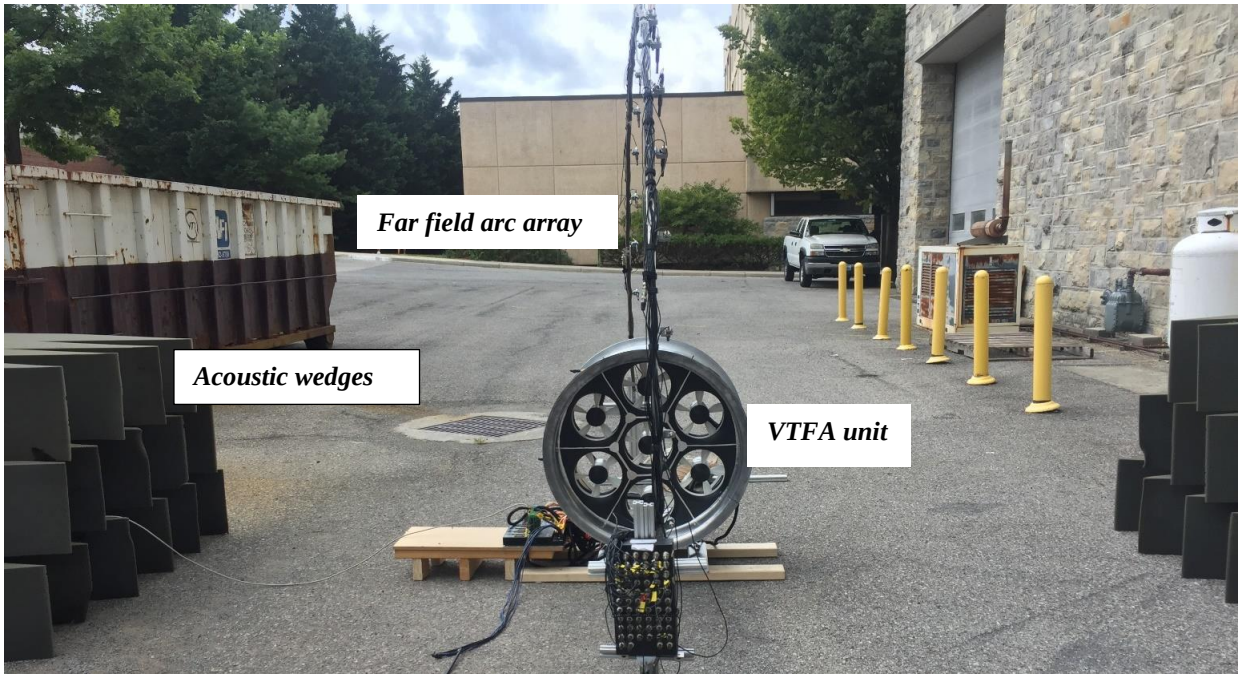

Figure 6.5: Noise measurements experimental setup (flow into the page).

The main instrumentation used for the flow measurements is a Digi-Sense Data Logging Vane Anemometer model 20250-22. The Anemometer has an accuracy of +/- 3% and a resolution of 0.1 m/s. The Anemometer is fully calibrated to NIST-standards. The axial velocity measurements of the VTFA unit were collected at 57 locations on the exit at azimuth angles of 0, 45, 90, 135, 180, 225, 270, 315 degrees and at 7 radial positions ($r / R = 0.15, 0.3, 0.45, 0.6, 0.75,$ and 0.95). The speed of the fans was controlled using the multi-axis DMC-4070 controller. The fans were assigned identification numbers as shown in Figure 6.6. A total of 13 axial flow measurements were made along the diameter of the baseline fan as shown in Figure 6.7 (0", ±3.5", ± 4.5", ± 6.0", ±7.5", ± 9.0", and ±11.0").

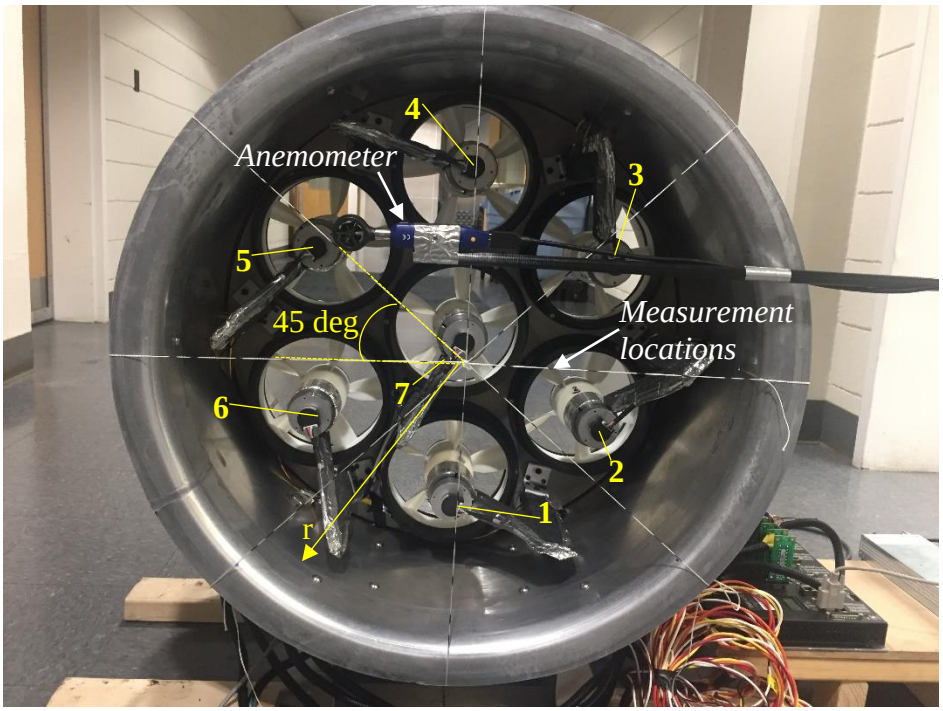

Figure 6.6: Flow measurement locations and fan identification number (view from the back). Measuremetns were conducted using a hand held Anemometer in 56 different locations.

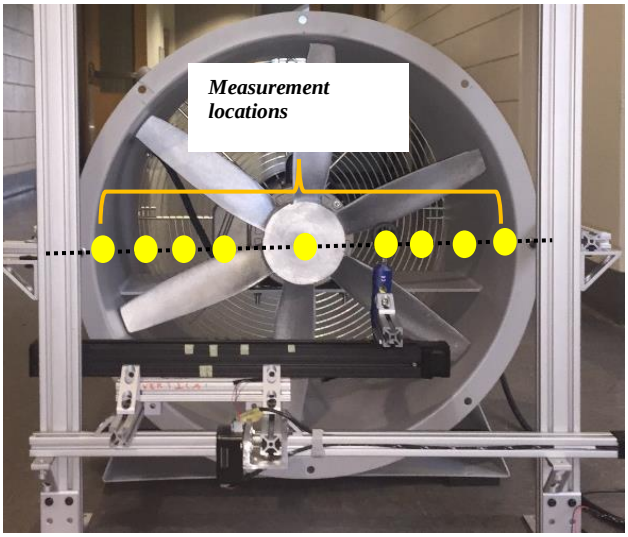

Figure 6.7: Flow measurement locations for the baseline Cincinnati fan. Measurements were made in 13 different positions along the fan diameter.

6.2.2 Aerodynamic Results

The flow measurements for the VTFA unit have been interpolated to generate axial flow velocity maps. This is necessary since the flow cannot be assumed to be axisymmetric. Figure 6.8(a) shows the flow map at a fan speed of 2800 rpm with all of the motors on and (b) at a fan speed 3064 rpm with motors 1 and 4 turned off. The axial velocity distribution is shows as a color map.

(a)

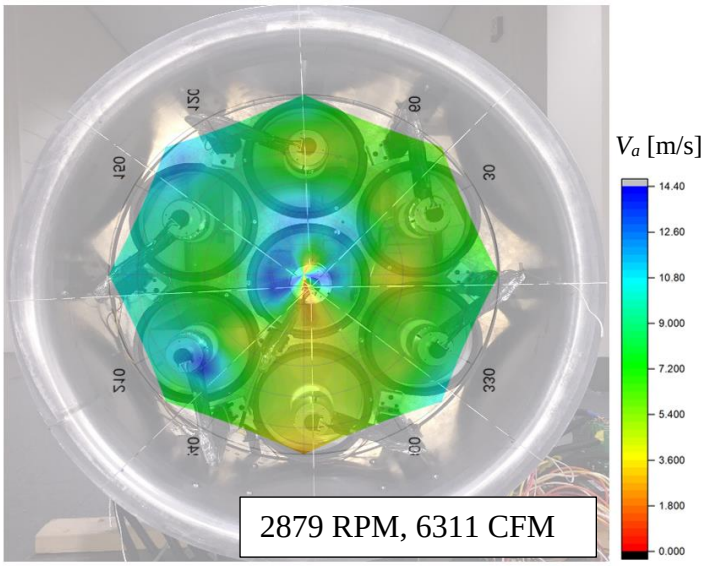

(b)

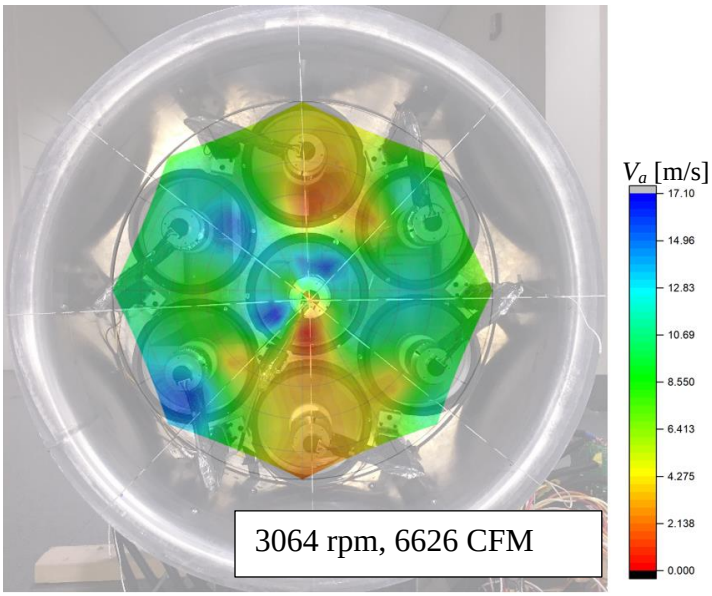

Figure 6.8: Measured axial flow velocity maps at **(a)** 2800 RPM with all motors on, and **(b)** 3000 rpm with motors 1 and 4 off (view from the back).

Figure 6.9 presents the measured volumetric flow rate as a function of fan speed for the VTFA unit. For reference, the results for the single CVT3 fan tested in Chapter 5 is also plotted. Figure 6.9 shows that the measured volumetric flow rate for the VTFA unit is within 15% of the volumetric flow rate estimated from measurements of the single fan. For example, at a fan speed of 3000 rpm the single fan generates 768 CFM. Thus, assuming 7 individual fans the total volumetric flow rate would be 769x7 = 5383 CFM. However, testing of the VTFA unit shows 6311 CFM at 2900 rpm. The dashed line in the figure is the estimate volumetric flow rate for the VTFA unit based on the single fan volumetric flow rate data. The difference in volumetric flow rate for the VTFA is probably due to a few factors: a) the addition of the unit inlet bell-mouth and (b) the large duct aligning the streamlines more in the axial direction as the flow travels downstream. A computational fluid dynamic (CFD) analysis would be required to fully investigate this benefit in volumetric flow rate but it is outside the scope of the thesis.

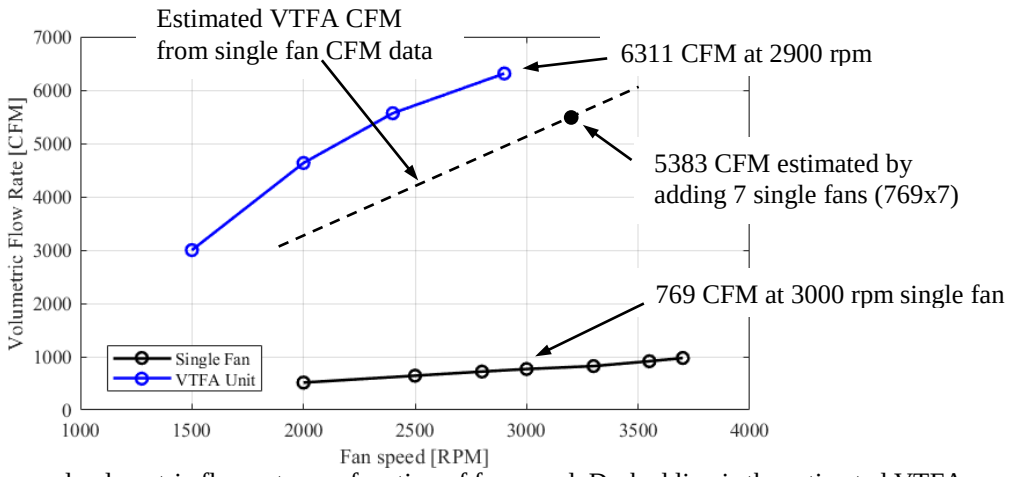

Figure 6.9: Measured volumetric flow rate as a function of fan speed. Dashed line is the estimated VTFA volumetric flow rate based on adding the contribution of 7 single fans.

The axial flow velocity measured along the diameter of the baseline Cincinnati fan is shown in Figure 6.10. It shows that the fan generated most of its flow in the center section of the blades. There are significant losses in the center of the duct due to the motor blockage and at the blade tips due to the large tip gaps, thick BL, and potentially poor blade design.

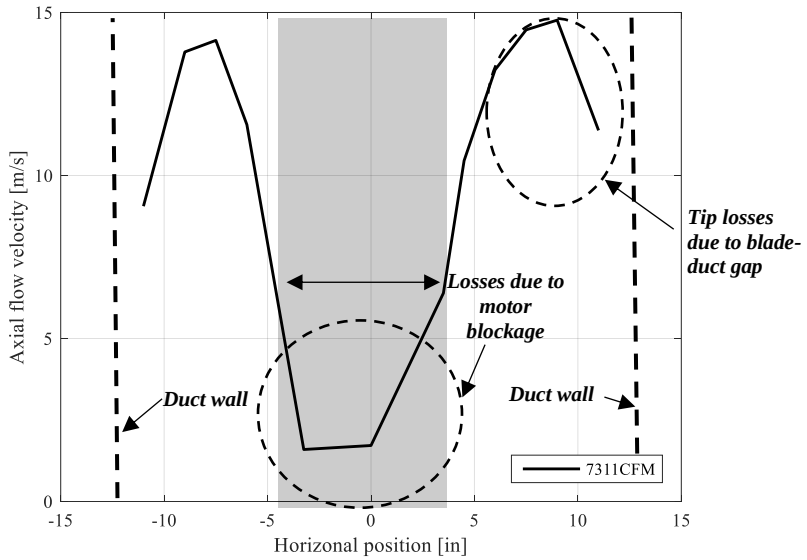

Figure 6.10: Measured axial velocity profile along the diameter of the baseline Cincinnati fan.

6.2.3 Noise Results

Figure 6.11 shows the narrowband sound power spectrum measured for the VTFA unit at 2500 rpm (red line). The background noise was also measured and plotted (blue line). The signal to noise ratio is ≥10 dB at 400 Hz and higher frequencies. Thus, there is no need for background correction in this frequency range. The overall sound power level for the VTFA unit is 84.6 dBA. The spectrum reveals a few interesting and important features. Firstly, the spectral shape is a very smooth broadband component with a strong roll off starting at 4000 Hz. Secondly, a hay-stack at ~1000 Hz is observed for the VTFA unit that was not present in the test of the isolated fan in Chapter 5 (black line). This hay-stack mechanical noise is due to vibration induced by the fans. It is believed that the struts supporting the motor-fan go into resonant motion at ~ 1000 Hz driven most likely by the unbalance of the motor-fans. The vibration can be significant and resulting in some of the fans touching the duct exacerbating the problem. Thirdly, both the VTFA unit and the background spectra show highest broadband levels below 400 Hz (yellow zone). This effect is very likely due to the windy conditions the day of the test (steady wind of 8 mph with some gusts) and the turbulence ingested due to the fan been so close to the ground (see later results in Figure 6.12 for more details). The ingested turbulence interacting with the fans results in the high VTFA unit noise levels in the low frequency range.

To gain more insight, an estimated of the VTFA unit noise was performed by taking the spectrum from the single fan noise measurements in the anechoic chamber and assuming that all 7 fans produce the same noise incoherently. That is the VTFA unit noise can be estimated as

$$L_{w,VTFA}(f) = L_{w,\text{single fan}}(f) + 10\log_{10}(7) \tag{6.1}$$

where $L_{w,\text{single fan}}(f)$ is the sound power spectrum of a single fan, and 7 is the number of fans resulting $10\log_{10}(7) = 8.5dB$. The estimated noise for the VTFA unit, $L_{w,VTFA}(f)$, is shown in Figure 6.11 (black line) with an overall power level of 79.5 dBA. The estimated (black line) and measured (red line) VTFA noise remarkably matches very well at ≥2000 Hz. Since the single fan noise spectrum was determined in the anechoic chamber, it is not affected by turbulence. Thus, the measured VTFA noise (red line) in the low frequency range is clearly due to turbulence (caused by the windy conditions and close proximity to the ground) interacting with the fans. Thus, the difference between the overall noise level 84.6 dBA (measured) and 79.5 dBA (estimated) is due to turbulence ingestion (noise at low frequency).

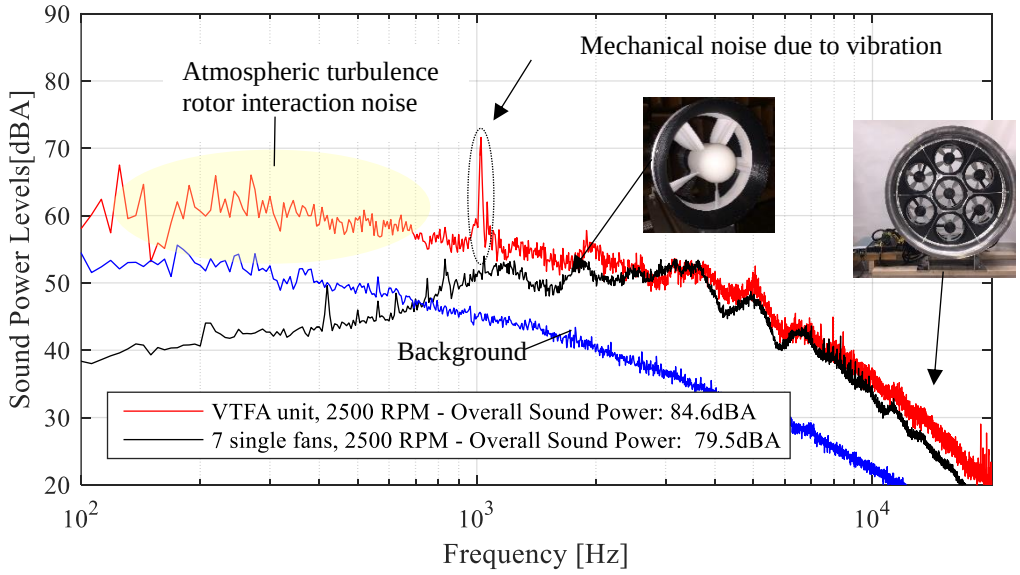

Figure 6.11: VTFA unit narrowband sound power spectrum measured and estimated: a) red line is measured VTFA unit, b) black line is estimated from single fan test in anechoic chamber and increased by 8.5 dB to account for 7 uncorrelated fans, an c) blue line is background noise.

The measured narrowband spectrum for the VTFA unit and baseline Cincinnati fan is presented in Figure 6.12. In this figure, the measured narrowband acoustic power spectrum for the VTFA unit at two configurations and for the baseline Cincinnati fan are shown. In Figure 6.12(a), VTFA unit was operated at 2800 rpm with all fans on. In Figure 6.12(b), the VTFA unit was operated at 3100 rpm but with fans 1 and 4 turned off. The results in both cases show that the VTFA unit produces significantly less noise over the key frequency range of interest (100 to 4000 Hz). The noise from the motor is visible in the tones at high frequency (7 to 10 kHz) in Figure 6.12(b). Motor noise has nearly insignificant contribution to the overall noise level. The results also show that the VTFA unit do not shows any blade passage frequency (BPF) tones typical of fans. However, it is possible that they could be masked by the turbulence ingested noise. Though, they are not expected to be as prominent as in the Cincinnati fan. The reason is that the individual fans were operated all at slightly different fan speeds (approximately +/- 10 rpm) thus eliminating the constructive interference between the fans at the BPF tones, e.g. acoustic energy was scattered out over a range of frequencies rather than a single one.

It is also interesting to note that the VTFA unit is significantly quieter for the case in Figure 6.12(b) (fans 1 and 4 are off while the other fans operate at 3100 rpm) as compared to the case in Figure 6.12(a) (all fans operating at 2800 rpm). However, in both cases the volumetric flow rate is nearly the same, e.g. 6311 vs 6626 CFM. The decreased in noise for the case in Figure 6.12(b) (fans 1 and 4 off) is likely due to fan 1 ingesting significant amount of flow distortion and turbulence because of proximity to the ground and hence it generates the most noise.

(a)

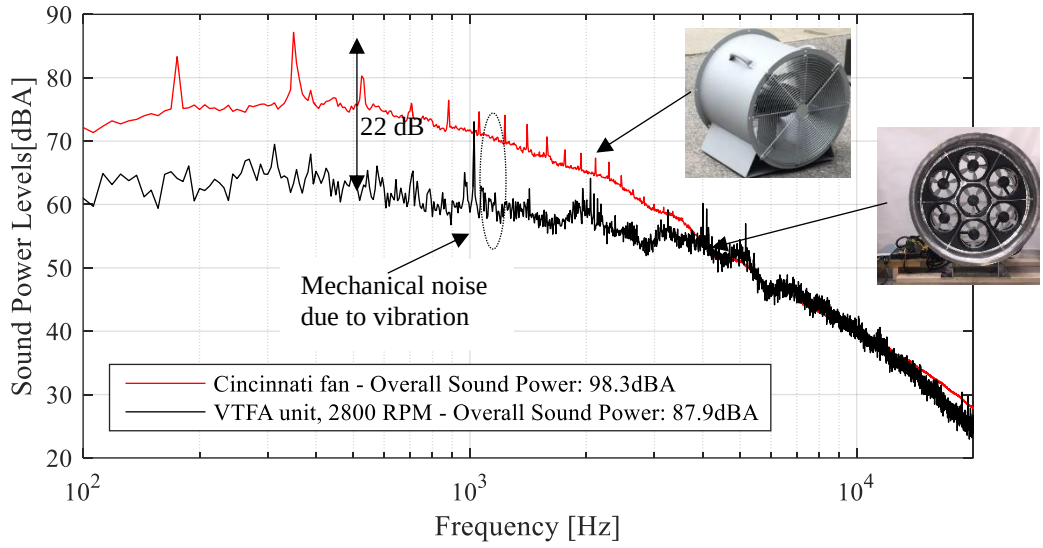

(b)

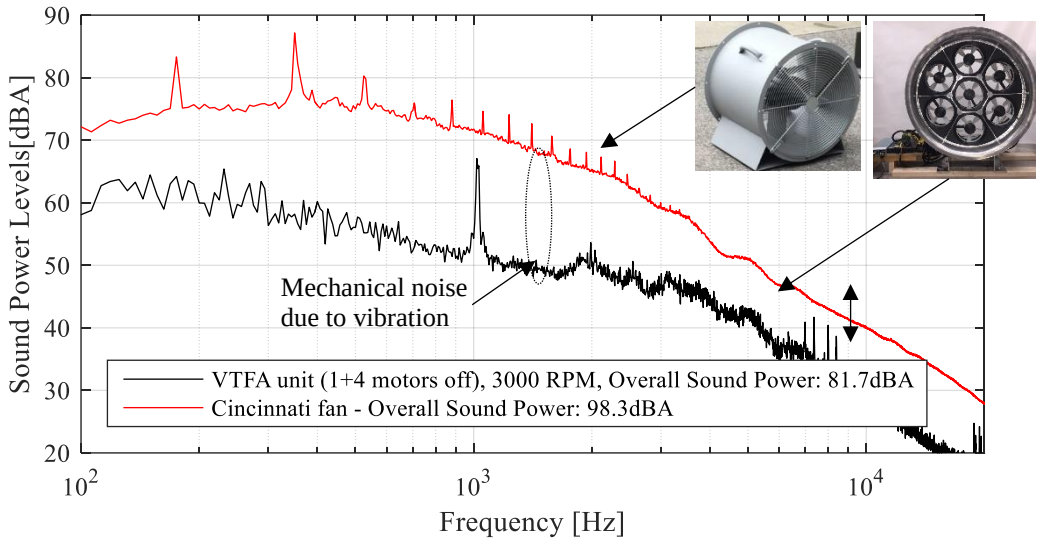

Figure 6.12: Narrowband power spectrum for **(a)** VTFA unit at 2800 rpm with all fans on and **(b)** VTFA unit at 3064 rpm with fans 1 and 4 off. In both cases Cincinnati fan operates at 1750 rpm.

6.3 Comparison to Commercial Fans

To summarize the noise results in a single plot, Figure 6.13 shows the overall sound power level for the VTFA unit as a function of fan rpm with all 7 motors operating (blue line). For reference, the case of 5 motors operating at 3064 rpm (motors 1 and 4 are off) in Figure 6.12(b) is also included as a solid black circle. The Cincinnati fan noise is indicated by the solid red circle at 98.3 dBA. The results for the single fan as a function of rpm measured in the anechoic chamber is also included (black line). The noise produced by 7 of these fans (incoherent addition) results in the single fan noise results to be shifted up by 8.5 dB (dashed black line). This line represents the quietest possible configuration with all 7 fans operating, e.g. unaffected by atmospheric turbulence and flow distortion from ground.

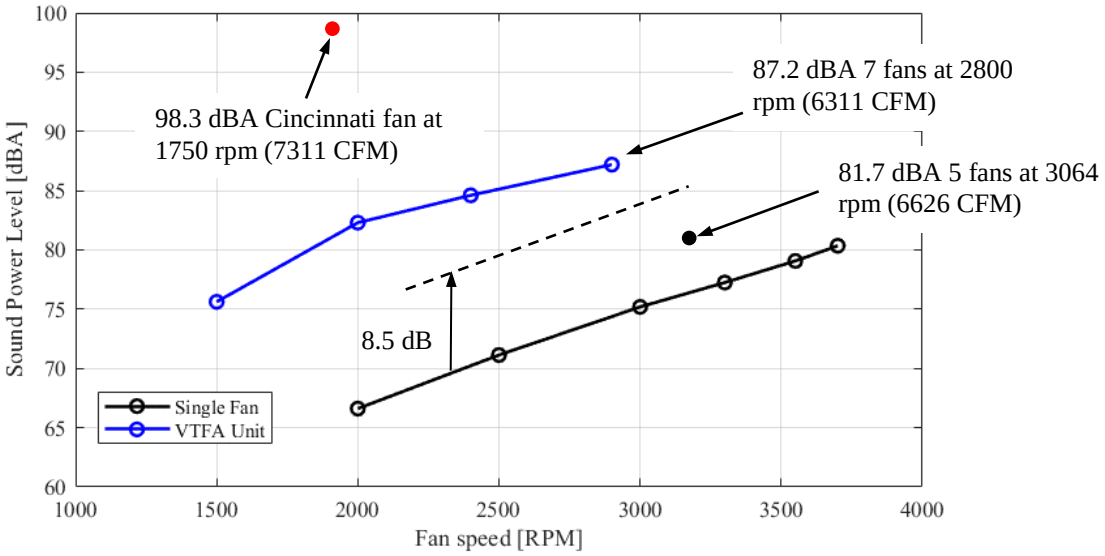

Figure 6.13: Overall sound power level as function of fan rpm.

The manufactured data collected for commercial fans in Chapter 2 is replotted in Figure 6.14 with the data collected for the Cincinnati baseline fan, CVT3 fan, and the VTFA unit. In this figure, the VTFA (green circle) generates a volumetric flow rate of 6626 CFM with 5 fans operating at 3000 rpm while generating 81.7 dBA overall sound power level. The VTFA unit outperforms all commercial fans of smaller sizes. Specifically compared to the baseline Cincinnati fan, the VTFA fan produces nearly the same flow rate (6626 vs 7311 CFM) at much lower noise levels (81.7 vs 98.3 dBA), e.g. a 16.6 dB reduction. Though several VTFA unit configurations were tested (number of operating fans and rpms), the one presented here (green circle) is the best in terms of both noise and flow rate. For completeness, the single CVT3 fan (shown as red circle) design used

in the VTFA system as tested in the anechoic chamber is also shown in this figure. It can be observed that this fan outperforms all other fan except for one. However, the diameter of this fan (0.32 m) is nearly twice the size of the CVT3 fan (0.18 m).

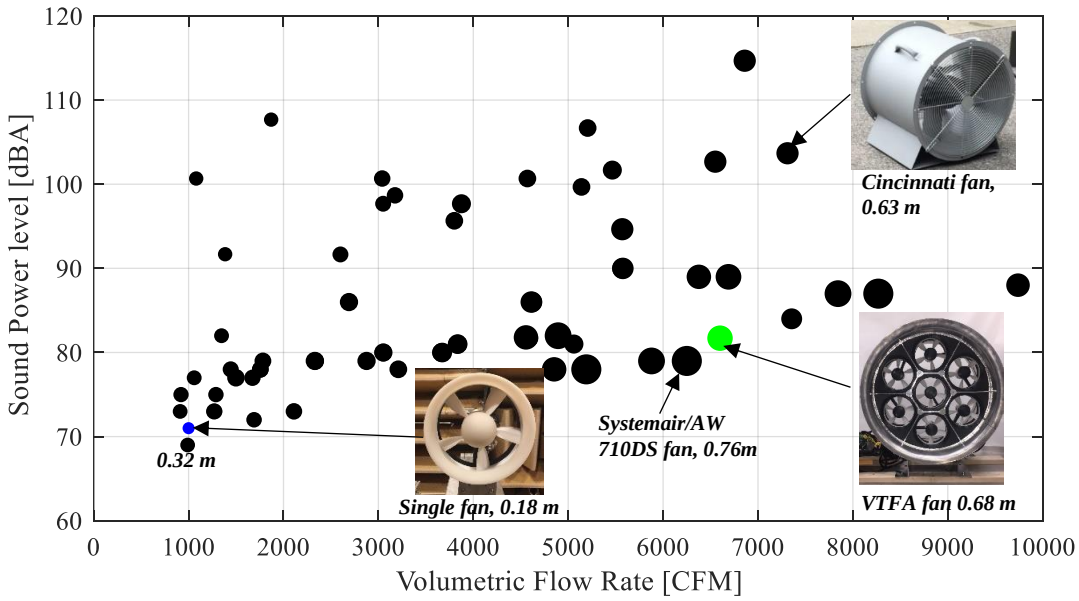

Figure 6.14: Performance of VTFA fan compared to commercial fans.

CHAPTER 7

7 Conclusion and recommendations for future work

7.1 Conclusions

A key contribution of this research work is the development of a new comprehensive design approach for rotor-only low-pressure axial ventilation fans considering both aerodynamic performance and noise. The stepwise approach implements a multi-objective genetic algorithm to determine the fan size (hub and tip radius), fan diameter, fan speed, and the span wise axial and swirl velocities to generate a user specified volumetric flow rate. The genetic algorithm defines the Pareto front, i.e. a family of optimal non-dominating solutions. The electric motor is then incorporated in the design process by selecting the solution that best matches the motor characteristics (e.g. motor operating at optimum efficiency). The blade geometry is then defined to produce the optimized velocity distribution at the specified fan speed. The resulting blade geometry generates the given volumetric flow rate at the minimum fan tip speed. The fan design is then complemented by the design of the optimum inlet duct geometry to maximize volumetric flow rate and minimize BL thickness for low noise generation. In the inlet duct design, size constrains can be incorporated into the design process. The comprehensive design approach has been implemented and experimentally validated for fans designed with single and multi-element airfoils. The good matching to the experimental results validated the design process.

Though multi-element airfoils are complex, a definitive trend towards implementing these geometries to axial compressors, wind turbines, and UAV propeller blades is ongoing. However, to the best of the author's knowledge, this was the first research effort to implement multi-element

airfoils into rotor-only axial ventilation fans. Unlike single element airfoils, there is no lift and drag polar data available in the open literature for multi-element airfoils at low Reynolds numbers. Consequently, the design of the multi-element airfoil configuration was carried out as part of this research using a dynamic programming approach. The design was carried out using the viscous/inviscid code MSES. Results showed that individual elements of the multi-element airfoil configuration will exhibit lower chord Reynolds numbers relative to the single element airfoil. The lower Reynolds numbers leads to the generation of separation bubbles. The separation bubble is eliminated by tripping the BL upstream of the separation bubble. The effect of tripping the BL on fan noise has been investigated experimentally. It has been shown that the tripped blades for the multi-element fans result in a significant decrease of noise. Therefore, the tripped multi-element airfoils exhibit lower drag and noise while maintaining the same lift. Additionally, it was shown that the blades of the fan implementing a multi-element airfoil operate at a significantly higher lift to drag ratio than the fan using the single element airfoil.

Experimental investigation of fans designed with single and multi-element airfoils have shown that fans designed with multi-element airfoils aerodynamically outperform single element fans. Therefore, the penalty caused by the increase in the drag is more than offset by the gain in the lift. This can be justified considering that an increase in the coefficient of lift results in a decrease in the required chord to generate a given lift force. A decrease in the chord results in a decrease in the overall drag for the fan. Good agreement between experimental and predicted aerodynamic and torque results suggests that the polars at low Reynolds numbers are predicted with great accuracy using MSES. Therefore, the lift and drag polars for multi-element airfoils computed using MSES can be readily implemented along traditional BEM design methods with excellent accuracy for the design of multi-element fans.

The fan noise results of the experimental work on the single element airfoil fan (CVS) have showed to agree well with the predicted sound power level spectrum from the combined rotor self-noise and turbulence rotor interaction noise models. Particular, it was shown that the measured noise spectrum for the CVS fan is dominated by turbulence rotor interaction noise. Consequently, turbulence rotor interaction noise resulting from the interaction of the blade tips with the duct wall boundary layer is underestimated in the open literature for small fans.

A direct comparison of fans designed with multi-element airfoils showed that the acoustic benefit is rather marginal in terms of overall sound levels. However, this research effort was limited by a lack of models to predict noise from multi-element airfoils at low Reynolds numbers. Consequently, future noise prediction models are needed to improve the design of multi-element airfoil fans. The data provided here provides a first step towards future acoustic prediction tool development that can be used for multi-element airfoil fans.

The innovations proposed here have been implemented into the design of a new advanced fan array system. The VTFA unit has been shown to outperform all commercial fans of smaller sizes. Specifically compared to the baseline Cincinnati fan, the VTFA fan produces nearly the same flow rate (6626 vs 7311 CFM) at much lower noise levels (81.7 vs 98.3 dBA), e.g. a 16.6 dB reduction.

7.2 Recommendations for future work

The Recommendations for future work are:

1. This research effort has demonstrated that turbulence rotor interaction noise is the dominant source of noise in small axial fans. Therefore, reducing the duct BL thickness will result in a significant reduction of fan noise. In this work, the inlet geometry was limited to an elliptical profile. It is recommended that new profiles and inlet configurations be investigated in order to reduce the BL thickness.

2. This research effort has demonstrated the need to develop noise prediction tools for fans designed with multi-element airfoils. As a first attempt, it is recommended that the noise prediction tools developed as part of this work are extended to fans designed with multi-element airfoils. An approach to accomplish this is by assuming that the noise from the individual airfoils is uncorrelated. It is possible to then compute the noise from each airfoil using the lift and drag polars of the each individual airfoils. These can be obtained experimentally or numerically using MSES. The process is then implemented as follows.

The drag contribution for airfoil 1 to the total drag for the fan blades can be computed by multiplying the total drag of the fan by the ratio of the individual drag of element 1 (computed by MSES) and the total drag of the multi-element airfoil (computed by MSES). This drag contribution of element 1 can be used to compute the noise of airfoil 1 using the noise prediction tools presented in this research effort. The same process can be repeated for element 2. The noise of element 1 and element 2 can be added incoherently to obtain the total noise spectrum. This assumption is a reasonable first approximation because it considers the contribution of two leading and trailing edges from two airfoils instead of just one airfoil.

References

Bammert, K., and Beelte, H. (1980). Investigations of an Axial Flow Compressor with Tandem Cascades. *Journal of Engineering for Power, 102*(4), 971-977. doi:10.1115/1.3230369

Betz, A. (1919). *Airscrews with minimum induced energy loss*. Retrieved from

Blair, G. P., and Cahoon, W. M. (2006). Special investigation: design of an intake bellmouth. *Race Engine Technology, 17*, 34-41.

Brooks, T. F., Marcolini, M. A., and Pope, D. S. (1989). *Airfoil self-noise and prediction.* Retrieved from http://vt.summon.serialssolutions.com/2.0.0/link/0/eLvHCXMwlV09C8IwED1UHNwUFT-h7lbaxmgdRRRdxcVJEnuFQkml0f_vXStS3FwCCUc-SfKOe3kBEMHCc3_OBHEnWK6W2kepyP9ZeyFKvaSNGCL5I8XXBJVH8N-36-aZ24VRVhUUy8_as5TgueD6MF4RrCRZJ5TPgdrriU5Wtq_cEYc2NEsw24Eami7MtkkeZ0nqWExj12SJRYe8dueRc2iEp6MH4rC_7I4uV3XjTtxYhfmubFLminKWYq70QvSp6czgABwlpcaAkYOiQVLqi3izjlah1tLzIjGE-T81j_4zH0OrJEIxp3QCjWf-winzBd8U2nSJ

Bruneau, P. R. P. (1994). *The design of a single rotor axial flow fan for a cooling tower application.* Stellenbosch: University of Stellenbosch.

Castegnaro, S. (2018). Aerodynamic Design of Low-Speed Axial-Flow Fans: A Historical Overview. *Designs, 2*(3), 20.

Castegnaro, S., Masi, M., and Lazzaretto, A. (2017). *Preliminary experimental assessment of the performance of rotor-only axial fans designed with different vortex criteria.* Paper presented at the 12th European Conference on Turbomachinery Fluid Dynamics and Thermodynamics, ETC 2017, April 3, 2017 - April 7, 2017, Stockholm, Sweden.

Chipperfield, A., and Fleming, P. (1995). The MATLAB genetic algorithm toolbox.

Cho, Y. T. (2018). Characterizing Sources of Small DC Motor Noise and Vibration. *Micromachines, 9*(2), 84. doi:10.3390/mi9020084

Cory, W. (2005). Fans and Ventilation - A Practical Guide: Elsevier.

Council, E. (2011). COMMISSION REGULATION (EU) No 327/2011 of 30 March 2011 implementing Directive 2009/125/EC of the European Parliament and of the Council with regard to ecodesign requirements for fans driven by motors with an electric input power between 125 W and 500 kW. *Official Journal of the European Union*.

cybernetics;, F. (Producer). (2019). Retrieved from http://www.feramat.com/en/reference-tunel-blanka.html

Dalton, W., Elliot, D., and Nickols, K. (1999). Design of a low speed fan stage for noise suppression.

Drela, M. (2014). *Flight vehicle aerodynamics*.

Drela, M. (2007a). MSES 3.05: A multielement airfoil design analysis system. *A Research Program by: MIT Computational Aerospace Sciences Laboratory*.

Drela, M. (1986). *Two-dimensional transonic aerodynamic design and analysis using the Euler equations*. Retrieved from

Drela, M. (2007b). A User's Guide to MSES 3.05.

Drela, M. (1989). XFOIL: An analysis and design system for low Reynolds number airfoils *Low Reynolds number aerodynamics* (pp. 1-12): Springer.

Drela, M., and Youngren, H. (2005). Ducted Fan Design Code (DFDC). Cambridge, MA. Retrieved from http://web.mit.edu/drela/Public/web/dfdc/

Drela, M., and Youngren, H. (2011). XROTOR. Cambridge, MA: Massachusetts Institute of Technology. Retrieved from http://web.mit.edu/drela/Public/web/xrotor/
Drela, M., and Youngren, H. (2003). XROTOR User Guide Cambridge, MA. Retrieved from http://web.mit.edu/drela/Public/web/xrotor/xrotor_doc.txt
Drzewiecki, S. (1892). Méthode pour la détermination des éléments mécaniques des propulseurs hélicoïdaux. *Association technique maritime*.
Dwyer (Producer). (2016). Specifications-Installation and Operating instructions. Retrieved from https://www.dwyer-inst.com/PDF_files/122d.pdf
Eck, B. (1973). Fans. *1st English ed., Pergamon Press, Oxford*, 139-153.
Envia, E., and Nallasamy, M. (1999). Design selection and analysis of a swept and leaned stator concept. *Journal of Sound and Vibration, 228*(4), 793-836.
Eugene Larrabee, E., and French, S. E. (1983). Minimum induced loss windmills and propellers. *Journal of Wind Engineering and Industrial Aerodynamics, 15*(1), 317-327. doi:http://dx.doi.org/10.1016/0167-6105(83)90201-5
Fukano, T., Takamatsu, Y., and Kodama, Y. (1986). The effects of tip clearance on the noise of low pressure axial and mixed flow fans. *Journal of Sound and Vibration, 105*(2), 291-308. doi:http://dx.doi.org/10.1016/0022-460X(86)90158-6
Glauert, H. (1926). *The Elements of Aerofoil and Airscrew Theory*. Cambridge, UK: Cambridge University Press.
Goldstein, S. (1929). On the vortex theory of screw propellers. *Proceedings of the Royal Society*(123).
Gopalarathnam, A., Broughton, B. A., McGranahan, B. D., and Selig, M. S. (2003). Design of low Reynolds number airfoils with trips. *Journal of Aircraft, 40*(4), 768-775.
Green, J. E., Weeks, D. J., and Brooman, J. W. F. (1973). Prediction of turbulent boundary layers and wakes in compressible flow by a lag-entrainment method. *ARC R&M 3791*.
HM Schulten, J. B. (1997). Vane sweep effects on rotor/stator interaction noise. *AIAA Journal, 35*(6), 945-951.
Hutcheson, F. V., Brooks, T. F., and Stead, D. J. (2012). Measurement of the noise resulting from the interaction of turbulence with a lifting surface. *International Journal of Aeroacoustics, 11*(5-6), 675-700.
Industries, A. C. (Producer). (2019). Retrieved from https://www.aircontrolindustries.com/construction/axial-fans-forced-ventilation/
Jang, C.-M., Furukawa, M., and Inoue, M. (2001). Noise Reduction by Controlling Tip Vortex in a Propeller Fan. *JSME International Journal Series B Fluids and Thermal Engineering, 44*(4), 748-755.
Jianu, O., Rosen, M. A., and Naterer, G. (2012). Noise Pollution Prevention in Wind Turbines: Status and Recent Advances. *Sustainability, 4*(6), 1104.
Jung, Y. K., Jeon, K.-S., Choi, C.-K., Maxim, T., Kim, S., and Lee, J.-W. (2015). Configuration Design and Optimization of Ducted Fan Using Parameter Based Design.
Keller, C. (1934). *Axialgebläse vom Standpunkt der Tragflügeltheorie.* (PhD thesis).
Keller, C., Weske, J. R., and Marks, L. S. (1937). *The theory and performance of axial-flow fans*. New York, London: McGraw-Hill Book Co.
Kurelek, J. W., Lambert, A. R., and Yarusevych, S. (2016). Coherent structures in the transition process of a laminar separation bubble. *AIAA Journal*, 2295-2309.
Laboratory, L. B. N. (1989). Improving Fan System Performance, a source for industry: The United States Department of Energy;

Air Movement and Control Association International, Inc.
Labriet, M., Joshi, S. R., Kanadia, A., Edwards, N. R., and Holden, P. B. (2013). *Impacts of climate change on heating and cooling: a worldwide estimate from energy and macro-economic perspectives* (ERMITAGE FP7/2007-2013). Retrieved from
Lakshmi, G., Balmuralidharan, P., and Sankar, G. (2018). High Lift Two-Element Airfoil Design for MALE UAV Using CFD.
Larrabee, E. E., and French, S. E. (1983). Minimum induced loss windmills and propellers. *Journal of Wind Engineering and Industrial Aerodynamics*`(15), 317-327.
Lin, X. H., Li, J., Cai, Y. P., and Ji, M. H. (2012). The Progress of the Study on Fan Noise Reduction Technology. *Advanced Materials Research, 591-593*, 2056-2059. doi:10.4028/www.scientific.net/AMR.591-593.2056
Longhouse, R. E. (1978). Control of tip-vortex noise of axial flow fans by rotating shrouds. *Journal of Sound and Vibration, 58*(2), 201-214. doi:http://dx.doi.org/10.1016/S0022-460X(78)80075-3
Longhouse, R. E. (1977). Vortex shedding noise of low tip speed, axial flow fans. *Journal of Sound and Vibration, 53*(1), 25-46. doi:http://dx.doi.org/10.1016/0022-460X(77)90092-X
Lyon, C., Selig, M., Broeren, A., Lyon, C., Selig, M., and Broeren, A. (1997). *Boundary layer trips on airfoils at low Reynolds numbers.* Paper presented at the 35th Aerospace Sciences Meeting and Exhibit.
Magne, S., Moreau, S., and Berry, A. (2015). Subharmonic tonal noise from backflow vortices radiated by a low-speed ring fan in uniform inlet flow. *The Journal of the Acoustical Society of America, 137*(1), 228-237.
Magne, S., Sanjosé, M., Moreau, S., and Berry, A. (2012). Aeroacoustic Prediction of the Tonal Noise Radiated by a Ring Fan in Uniform Inlet Flow.
Majumdar, S. J., and Peake, N. (1998). Noise generation by the interaction between ingested turbulence and a rotating fan. *Journal of Fluid Mechanics, 359*, 181-216.
Marte, J. E., and Kurtz, D. W. (1970). A Review of Aerodynamic Noise From Propellers, Rofors, and Lift Fans.
McGlumphy, J. (2008). *Numerical investigation of subsonic axial-flow tandem airfoils for a core compressor rotor.* Virginia Tech.
Moreau, A., and Guérin, S. Development and Application of a New Procedure for Fan Noise Prediction.
Moreau, S., Henner, M., Casalino, D., Gullbrand, J., Iaccarino, G., and Wang, M. (2006). Toward the prediction of low-speed fan noise. *Proceedings of the Summer Program 2006*, 519-531.
Mugridge, B. D., and Morfey, C. L. (1972). Sources of noise in axial flow fans. *Journal of the Acoustical Society of America, 51*(5), 1411-1427. doi:10.1121/1.1912992
Nakamura, Y., Isomura, K., and Kodama, H. (1986). *Rotor-strut interaction noise of a model fan.* Paper presented at the 10th Aeroacoustics Conference.
Neise, W., and Michel, U. (1994). Aerodynamic noise of turbomachines. *Deutsche Forschungsanstalt für Luft-und Raumfahrt, eV, DLR, Institut für Strömungsmechanik, Abt. Turbulenzforschung, Berlin, 5*.
NIEKERK, C. G. V. (1965). Noise generation in axial flow fans.
Osborne, W. C. (1966). Fans *International series of monographs in heating, ventilation and refrigeration*: Pergamon Press.

OSHA. (2013). *Ventilation in Shipyard Employment* (OSHA 3639-04 2013). Retrieved from https://www.osha.gov/Publications/OSHA3639.pdf

Padhy, S. K. (1994). *Noise generation in small axial flow fans: analysis and some design guidelines for noise reduction.* Paper presented at the 45th Annual International Appliance Technical Conference Designs on Technology, 9-11 May 1994, Madison, WI, USA.

Piellard, M., Coutty, B. B., Goff, V. L., Vidal, V., and Perot, F. Direct aeroacoustics simulation of automotive engine cooling fan system: effect of upstream geometry on broadband noise.

Pitot Static Tube: Properties and Characteristics. (2015). Retrieved from http://www.unitedsensorcorp.com/pitot-properties.html

Power-Star-Electrical. (2019). Retrieved from https://powerstarelectricals.co.uk/portable-ventilator-axial-blower-workshop-extractor-fan-220--240v-99-p.asp

Puterman, M. L. (2014). *Markov Decision Processes.: Discrete Stochastic Dynamic Programming*: John Wiley & Sons.

Roger, M., Moreau, S., and Guedel, A. (2006). Broadband Fan Noise Prediction Using Single-Airfoil Theory. *Noise Control Engineering Journal, 54*(1).

Roy, B., Mulmule, A., and Puranam, S. (2009). *Aerodynamic Design of a Part-Span Tandem Bladed Rotor for Low Speed Axial Compressor.* Paper presented at the 27th AIAA Applied Aerodynamics Conference.

Ruden, P. (1944). *Investigation of single stage axial fans*. Retrieved from

Saha, U. K., and Roy, B. (1997). Experimental investigations on tandem compressor cascade performance at low speeds. *Experimental Thermal and Fluid Science, 14*(3), 263-276. doi:https://doi.org/10.1016/S0894-1777(96)00125-2

Sargent, P. B., and Anemaat, W. A. (2018). *Benchmarking a Robust Panel Code for Ducted Fan VTOL Aircraft Design.* Paper presented at the 2018 Applied Aerodynamics Conference.

Schlichting, H., and Gersten, K. (2016). *Boundary-layer theory*: Springer.

Selig, M. S., Donovan, J., and Fraser, D. (1989a). Summary of Low Speed Airfoil Data, Vol. 1-4: Soar Tech Publications, Virginia Beach, VA.

Selig, M. S., Donovan, J. F., and Fraser, D. B. (1989b). Airfoils at low speeds.

Shimada, K., Kimura, K., and Watanabe, H. (2003). A study of radiator cooling fan with labyrinth seal. *JSAE Review, 24*(4), 431-439. doi:10.1016/S0389-4304(03)00076-6

Stahl, K. (1924). Air propeller.

Szafran, K., Shcherbonos, O., and Ejmocki, D. (2014). Effects of duct shape on ducted propeller thrust performance. *Prace Instytutu Lotnictwa*.

Terry, E. L. (2004). Extension of the aerodynamic design program MSES for the simulation of boundary layer suction.

Theodorsen, T. (1948). *Theory of Propellers*. New York: McGraw-Hill.

Tiwari, A., Patel, S., Lad, A., and Mistry, C. (2016). *DEVELOPMENT OF BELL MOUTH FOR LOW SPEED AXIAL FLOW COMPRESSOR TESTING FACILITY*.

Vad, J., and Horvath, C. (2008). *The impact of the vortex design method on the stall behavior of axial flow fan and compressor rotors.* Paper presented at the 2008 ASME Turbo Expo, June 9, 2008 - June 13, 2008, Berlin, Germany.

Wallis, R. A. (1983). *Axial flow fans and ducts*. New York: Wiley.

Williamson, G. A., McGranahan, B. D., Broughton, B. A., Deters, R. W., Brandt, J. B., and Selig, M. S. (2012). Summary of Low-Speed Airfoil Data, Vol. 5. *University of Illinois, Champaign, IL*, 204.

Winslow, J., Otsuka, H., Govindarajan, B., and Chopra, I. (2018). Basic Understanding of Airfoil Characteristics at Low Reynolds Numbers (104–105). *Journal of Aircraft, 55*(3), 1050-1061. doi:10.2514/1.c034415

Wright, S. E. (1976). The acoustic spectrum of axial flow machines. *Journal of Sound and Vibration, 45*(2), 165-223. doi:10.1016/0022-460X(76)90596-4

Xiang Hua, L., Ji, L., Yun Peng, C., and Ming Hui, J. (2012). The Progress of the Study on Fan Noise Reduction Technology. *Advanced Materials Research, 591-593*(3), 2056-2059. doi:10.4028/www.scientific.net/AMR.591-593.2056

Yilmaz, S., Erdem, D., and Kavsaoglu, M. (2013). *Effects of duct shape on a ducted propeller performance.* Paper presented at the 51st AIAA aerospace sciences meeting including the new horizons forum and aerospace exposition.

Yong-Han, K., Bo-Suk, Y., and Chang-Joon, K. (2006). Noise Source Identification of Small Fan-BLDC Motor System for Refrigerators. *International Journal of Rotating Machinery, 2006*. doi:10.1155/IJRM/2006/63214